Sudan University of Science & Technology

Faculty of Science

Department of Physics

The Effect of Exchanging the ZnO and CuO layers on the performance of solar cells

تأثير تبديل طبقات أكسيد الزنك وأكسيد النحاس على أداء الخلية الشمسية

Thesis Submitted In partial fulfillment of requirement for the degree of (PhD) in Physics

Prepared by:

Thowra Abd Elradi Daldowm

Supervised:

Mubarak Dirar A. Allah

February 2016


بسم الله الرحمن الرحيم

الآية

Quran Verse

قال تعالى:

﴿وَعَلَّمَ ءَادَمَ ٱلۡأَسۡمَآءَ كُلَّهَا ثُمَّ عَرَضَهُمۡ عَلَى ٱلۡمَلَٰٓئِكَةِ فَقَالَ أَنۢبِـُٔونِي بِأَسۡمَآءِ هَٰٓؤُلَآءِ إِن كُنتُمۡ صَٰدِقِينَ ٣١ قَالُواْ سُبۡحَٰنَكَ لَا عِلۡمَ لَنَآ إِلَّا مَا عَلَّمۡتَنَآۖ إِنَّكَ أَنتَ ٱلۡعَلِيمُ ٱلۡحَكِيمُ ٣٢﴾

صدق الله العظيم

سورة البقرة (31 – 32)

Deduction

We would like to dedicate

This simple work

To

My Father's Soul

To

My Mother's Soul

To

My Husband

To

My son Mohamed

To

My Brother's

To

My University (Dalanj University)

To

All Whom Love us

Acknowledgement

I would like to take this opportunity to thank some people who helped me to write and complete this research. First of all, I would like to thank my supervisor professor, **Mubarak Dirar A. Allah** for his time and support while pursuing my research.

Thanks to Professor Mohammed Osman Seed Ahmed for supporting me with essential information. My gratitude's to Dr. Abd Alsakhi and his group of chemistry at the laboratory of Alneelain University for helping in the preparation of the thin film photovoltaic.

Finally my gratitude's extend to my family and in particular my husband Gumaa Elwkeel Elieysir for his support and encouragement that helped me complete this research successfully.

المستخلص

في هذا البحث تم تصنيع نوعين من الخلايا الشمسية النوع الأول FTO/CuO/ZnO/AL والثاني هو FTO/ZnO/CuO/Al. حضرت ستة عينات من كل نوع. وحسبت كفاءة كل نوع. حيث أتضح أن كفاءة FTO/CuO/ZnO/AL في حدود 2×10^{-3} في حين أن كفاءة FTO/ZnO/CuO/Al في حدود 0.6×10^{-3}. وهذا الفرق قد يعزى لكون أن FTO و CuO يعملان كشبه موصل موجب في حين يعمل ZnO كشبه موصل سالب.

النوع الأول يعمل كـــ PnP خلية لذا تكون كفاءتها منخفضة والنوع الثاني يعمل كـــPPn خلية لذا تكون كفاءتها مرتفعة نسبياً. تم حساب فجوة الطاقة لـــ CuO و ZnO باستخدام طيف الامتصاص والنفاذ الضوئي أخذ الامتصاص الضوئي لـــ CuO و ZnO قيم مكافئة لفجوة طاقة في المدى $(1.3 - 2eV)$ و $(-2.2$ $3.6eV)$ بالترتيب، وهذه القيم تتسق مع القيم المشاهدة في دراسات النظري هذه القيم تحسب المستويات المتقبلة والمانحة لـــ CuO و ZnO. في حين بينت أطياف النفاذ فجواة طاقة في حدود $3.7eV$ و $3.6eV$ وهذه القيم توجد فجوة الطاقة بين نطاق التوصيل والتكافؤ بالترتيب.

Abstract

In this work two solar cells types were fabricated. The first type is (FTO/CuO/ZnO/Al) and the second type is FTO/ ZnO/ CuO/Al. Six samples were prepared from each type. The efficiency for each type was obtained. It was found that the efficiency of FTO/ZnO/CuO/Al is in the range ~0.6×10^{-3}, while the efficiency of FTO/CuO/ZnO/Al is in the range ~2×10^{-3} the difference may be attributed to the fact that FTO and CuO acts as P-type semiconductor, while ZnO act and n-type semiconductor.

Thus the first type acts as PnP component that has a low efficiency, while the second type acts as PPn component and has relatively high efficiency.

The energy gaps for CuO and ZnO are obtained by using optical absorption and transmittance spectra the optical absorption for CuO and ZnO shows a peak corresponding to the energy gaps in the ranges (1.3 – 2 eV) and (2.2-3.6eV) respectively. These values are compatible with the observed values in other studies, these values measure acceptor and donor levels For CuO and ZnO, however the transmittance spectrum for CuO and ZnO, shows band gaps about Eg~3.7eV and 3.6 E_geV. These values measure the energy gap between conduction and valence band for both, respectively.

Table of contents

Table of Appendix

List of Figures

List of Tables

List of Abbreviations

No	Subjects
PV	Photovoltaic
UV	Ultra violet
VIS	Visible light
IR	Infrared
λ	Wavelength
AM1.5	Is the reference spectrum measured at a solar zenith angle of 48.19^0?
CuO	Copper Oxide
ZnO	Zinc Oxide
XRD	X-ray diffractometer
Au	Gold
(J-V)	Current density voltage
IPCE	The incident photon to current conversion efficiency
ITO	Indium tin oxide
FTO	Fluorine-doped tin oxide
TZO	Tin –doped zinc oxide
Al	Aluminum
DSC_s	Dye – sensitized solar cells
R	Reflected
T	Transmitted

C-si	Crystalline Silicon Dye-sensitized solar cells
A – si	Amorphous Silicon
Mc-si	Multicrystalline silicon
Sc-si	Single crystal silicon
DSC_s	Dye- Sensitized Solar Cells
IC	Integrated Circuit
ECD	The Equivalent Circuit Diagram
AR	Antireflection
SEM	Scanning Electron Microscopy
EDS	Energy Dispersive Spectrometry
XRD	X-Ray Diffract

Chapter One

Introduction

1 Renewable energy

Solar cells are photovoltaic (PV) device that convert the electromagnetic radiation (i.e. light, including infrared, visible, and ultraviolet) from the sun in to utilizable electrical energy. The conversion process can be considered as a sequence of the four basic steps. The first step is the light absorption, which causes a transition from a ground state to an excited state in a material (the absorber of light). The second steps the conversion of the excited state in to at least one free electron, hole pair (photo generation). The third step is the presence of a force such that the produced free electrons travel in one direction and the produced free hole travel in the opposite direction. This causes charge separation. Then it is important the last step requires completion of an external circuit by the combination of returning electrons with hole to return the absorber to the ground state (non-equilibrium open system).

1.1 Solar Radiation

Solar radiation is an electromagnetic wave emitted by the sun's surface that originates in the bulk of the Sun where fusion reactions convert hydrogen atoms into helium. Every second $3.89.10^{-26}$ J of nuclear energy is released by the Sun's core [1]. This nuclear energy flux is rapidly converted into thermal energy and transported toward the surface of the star where it is released in the form of electromagnetic radiation.

The power density emitted by the Sun is of the order of 64 MW/m^2 of which ~ $1370W/m^2$ reaches the top of the atmosphere

with no significant absorption in the space. The latter quantity is called the solar constant.

The spectral range of the solar radiation is very large and encompasses anemometric wavelengths of gamma-and X- rays through metric wavelengths of radio waves. The energy flux is divided unevenly among the three large spectral categories.

Ultraviolet (UV) radiation ($\lambda < 400nm$) accounts for less than 9% of the total, visible light (VIS) (400nm$< \lambda < 700nm$) for 39%, and infrared (IR) for about 52%.

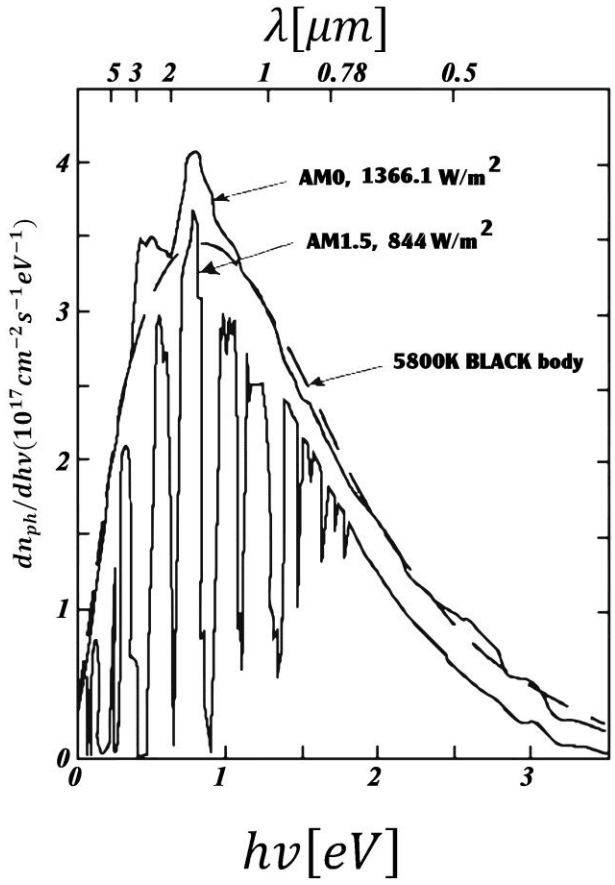

Fig (1.1).Extraterrestrial (AM_0) and ground-level (AM1.5) spectra of the solar radiation .The dashed line represents the emissionspectrum of a black body at 5800K.

As shown in fig, (1.1), the pattern of the solar spectrum resembles closely the radiation of a perfect black body at 500K. In the figure, AM_0 indicates the Air Mass Zero reference spectrum measured –and partially modeled –outside the terrestrial atmosphere [1].

Radiation reaching the Earth's surface is altered by a number of factors, namely the inclination of the Earth's axis and the atmosphere that causes both absorption and reflection (albedo) of part of the incoming radiation.

The influence of all these elements on solar radiation is visible in the ground-level spectrum, labeled $AMI^1.5$ in fig.1, where the light absorption by the molecular elements of the atmosphere is particularly evident. Accounting for absorption by the atmosphere, reflection from cloud tops, oceans, and terrestrial surfaces, and rotation of the Earth (day/night cycles), the annual mean of the solar radiation reaching the surface is $170W/m^2$ for the oceans and $180W/m^2$ for the continents [2]. Of this, about 75% is direct light, the balance of which is scattered by air molecules, water, vapor, aerosols, and clouds.

Fig (1.2) solar radiation energy flow diagram units in TW [3]. Shaded surfaces represent natural energy destruction; arrows represent human use for energy services.

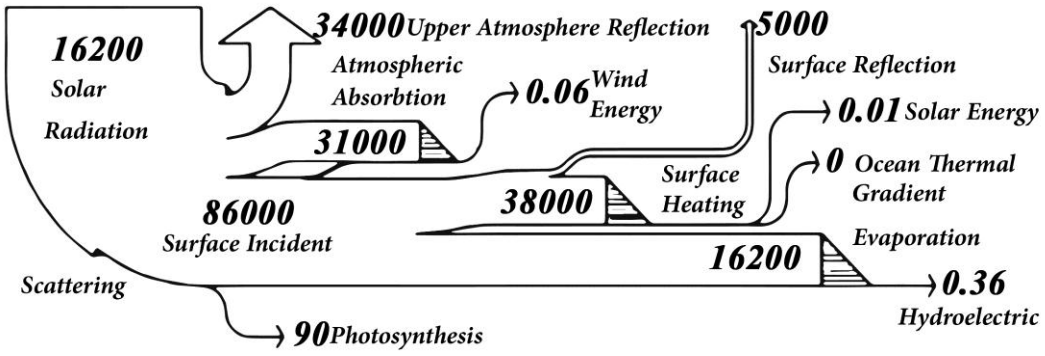

Fig (1.2) solar radiation energy flow diagram (units in TW). Shaded surfaces represent natural energy destruction; arrows represent human use for energy services.

The diagram in fig (1.2) illustrates the flow of the work potential, or energy, of the solar energy into the atmosphere and the terrestrial ecosystem. This quantity represents the upper limit to the work obtainable from solar radiation conversion, a limit that is imposed by the 2nd law of thermodynamics and is indepent of any conceptual device.

Of the 162PW of solar radiation Earth, 86PW hit its surface in the form of direct (75%) and diffused light (25%). The energy quality of diffused radiation is lower (75.2% of energy content instead of 93.2%for direct light [3], with consequences on the amount of work that can be extracted from it. 38 PW hit the continentals and a total energy of 0.01TW is estimated to be destroyed during the collection and use of solar radiation for energy services. This estimation includes the use of photovoltaic and solar thermal plants for the production of electricity and hot water. Similar estimates are shown for wind energy (0.06TW), ocean thermal gradient (not yet exploited for energy production), and hydroelectric energy (0.36TW) [3].

1.2 Renewable Energy Sources

Fortunately, we have renewable energy sources which neither run out nor have any significant harmful effects on our environment. Naturally, power plants that use wind, the potential, wave or tidal energy of water, the heat from the Earth's crust or direct solar radiation rely on the local supply of their primary energy source. Thus, the amount of power they can supply over a longer period often depends on geographical and weather conditions.

It is important to recognize that the installation of these power systems should always be preferred as long as they supply more energy throughout their lifetime than they have consumed during their fabrication, installation and maintenance. Although this criterion is fulfilled for all of them their prices are not yet low enough. Unless we can soon develop low cost technologies for renewable energy sources we have to hope that the world's governments start to consider the "costs" of environmental hazards of the majority of existing power sources in the planning of future power plants [4].

1.3 Inorganic Solar Cells

At present, solar cells comprising an inorganic semiconductor such as mono- and multi-crystalline silicon have found markets for small scale devices such as solar panels on roofs, pocket calculators and water pumps .These conventional solar cells can harvest up to as much as 24% of the incoming solar energy which is already close to the theoretically predicted upper limit of 30%. This illustrates that technologies which allow low fabrication costs - rather than somewhat higher conversion efficiencies - are now

desired. One approach here would be to reduce the amount of silicon by using thinner films on (cheap) glass substrates. Today, the production of these solar cells still requires many energy intensive processes at high temperatures (400-1400^{o}C) and high vacuum conditions with numerous lithographic steps leading to relatively high manufacturing costs [4].

1.4 Organic Solar Cells

Considerably less effort and production energy is necessary if organic semiconductors are used because of simpler processing at much lower temperatures ($20 - 200^{0} C$) than the above mentioned inorganic cells.

For example, electro-chemical solar cells using titanium dioxide in conjunction with an organic dye and liquid electrolyte already exceeded 6% power conversion efficiencies and are about to enter the commercial market thanks to their relatively low production costs. Another interesting alternative to inorganic cells is given by the semiconducting polymers, which combine the optoelectronic properties of conventional semiconductors with the excellent mechanical and processing properties of polymeric i.e. ”plastic” materials. These can be processed from solution at room-temperature onto e.g. flexible substrates using simple and therefore cheaper deposition methods like spin or blade coating. Since the discovery of electro-luminescence in conjugated polymers, this class of materials has been used to build efficient light emitting diodes field, effect transistors, optically-pumped lasers and photovoltaic diodes.

The advantage of polymeric photovoltaic cells when compared to electro-chemical cells is predominantly the absence of

a liquid electrolyte, which generates problems with sealing against air, but also the prospect of even cheaper production using large area devices and the use of flexible substrates. Possible applications may range from small disposable solar cells to power smart plastic (credit, debit, phone or other) cards which can display for example, the remaining amount, to photo detectors in large area scanners or medical imaging and solar power applications on uneven surfaces [4].

1.5 The Objective of the Study

The objective of this research is to develop low cost, chemically stable easy manufactured solar cells.

Remedy the defects of conventional traditional solar cells, like (SiO) solar cell which are very expensive, and not available, in contrary to CuO and ZnO available not costly material.

- Contribution in the reduction of the consumption of fossil fuel, and reeducation of pollution.
- The development of the solar cells, and their technologies, by improving efficiency.

1.6 The Significance of the Study

Remote area in Sudan needs electricity. It is possible to exploit the direct solar energy , in the generation of electricity. In addition, the solar energy is free, clean and not –pollutant

1.7 The Problem of Study

- The solution of the problem of electricity, at root in all the rural and urban areas, of the Sudan, which suffer from the non-provision of electricity services.

- The increase of the demand of the solar cells, and their low cost, makes it easy to reach all the individuals.
- The lesser levels of pollution, provides it with great prospects, in future.
- The advancement of the remote areas, in which there is no electricity, by the connection of educational and learning aids.

1.8 Methodology

Literature review had made through consultation of relevant references, journals and internet in the field of the solar cells "How to fabricate FTO/ZnO/CuO/Al and FTO/CuO/ZnO/Al, in the laboratory of Alnilaan university faculty of science.

Type of Study:	Field study
Sources of Data:	directly preparation of thin films CuO, ZnO thin film in laboratory, Reference, web sites.
Equipment:	CuO and ZnO thin films and FTO substrata and Al substrate.

1.9 Thesis Scope

The thesis consists of four chapters. Chapter One is the introduction, Chapter two is devoted for the theoretical background, while chapter three is concerned with the literature review. Results, Discussion and Conclusion are exhibited in chapter four.

Chapter 2

Theoretical background

2 Introduction

For photovoltaic (PV) technology to be a serious contender as an alternative energy source the electricity generated must be reasonable cost – effective compared with current fossil fuel sources [10, 11]. This requires that the efficiency of the PV cells be increased and their manufacturing costs be reduced.

While photovoltaic cells based on bulk semiconductors can provide very high efficiency (e.g. a conversion efficiency of >25% for single junction GaAs solar cells), their high manufacturing cost currently limits their use to primarily space – based application [12].

Solution – process able solar cell technologies can enable the realization of low - cost and high – through put photovoltaic production [13]. While much work has previously focused on organic semiconductors [14], organic solar cells can be manufactured at room temperature. Also have many advantages such as a low cost, easy fabrication of thin film, and possible manufactured to a large size. Because it can be made to be flexible, a research and development on solar cells are actively in progress for the next generation [15, 16], colloidal inorganic semiconductor anon crystals (NCs) are starting to attract attention for photovoltaic application [13]. NCs have the advantages of being solution-processable capable of a absorbing a large fraction of the solar spectrum, and tunable band – gab due to quantum – confinement effects [13].

One of the most promising alternatives has been dye – sensitized solar cells (DSCs) [17]. DSC_s use dye molecules an adsorbed on a wide band gab semiconducting material for light

harvesting. The photo excited dye emits an electron to the conducting substrate, connected to an external load, through the semiconducting material [17].

2.1 Semiconductor

A semiconductor is a solid material that has electrical conductivity in between that of a conductor and that of an insulator; it can very over that wide range either permanently or dynamically. Semiconductors are tremendously important in technology. Semiconductor devices, electronic components made of semiconductor materials, are essential in modern electrical devices. Examples range from computers to cellular phones to digital audio players.

Silicon is used to create most semiconductors commercially, but dozens of other materials are used as well. Semiconductors are very similar to insulators. The two categories of solids differ primarily in that insulators have large band gaps- energies that electrons must acquire to be free to move from atom to atom. In semiconductors at room temperature, just as in insulators, very few electrons gain enough thermal energy to leap the band gap from the valence band to the conduction band, which is necessary for electrons to be available for electric current conduction. For this reason, pure semiconductors and insulators in the absence of applied electric fields, have roughly similar resistance. The smaller band gaps of semiconductors, however, allow for other means besides temperature to control their electrical properties.

Semiconductors' intrinsic electrical properties are often permanently modified by introducing impurities by a process known as doping. Usually, it sufficient to approximate that each impurity atom adds one electron or one "hole" that may flow freely. Upon the addition of a sufficiently large proportion of impurity dopants, semiconductors will conduct electricity nearly as

well as metals. Depending on the kind of impurity, a doped region of semiconductor can have more electrons or holes, and is named n-type or p-type semiconductor material, respectively. Junctions between regions of N- and P-type semiconductors create electric fields, which cause electrons and holes to be available to move away from them, and this effect is critical to semiconductor device operation. Also, a density difference in the amount of impurities produces a small electric field in the region which is used to accelerate non-equilibrium electrons or holes. In addition to permanent modification through doping, the resistance of semiconductors is normally modified dynamically by applying electric fields. The ability to control resistance/conductivity in regions of semiconductor material dynamically through the application of electric fields is the feature that makes semiconductors useful. It has led to the development of a broad range of semiconductor device, like transistors and diodes. Semiconductor devices that have dynamically controllable conductivity, such as transistors, are the building blocks of integrated circuits devices like the microprocessor. These "active" semiconductor devices (transistors) are combined with passive components implemented from semiconductor material such as capacitors and resistors, to produce complete electronic circuits.

In most semiconductors, when electrons lose enough energy to fall from the conduction band to the valence band (the energy levels above and below the band gap), they often emit light, a quantum of energy in the visible electromagnetic spectrum. This photoemission process underlies the light- emitting diode (LED)and the semiconductor laser, both of which are very important commercially. Conversely, semiconductor absorption of light in photodetectors excites electrons to move from the valence band to the higher energy conduction band, thus facilitating detection of light and vary with its intensity. This is useful for fiber

optic communications, and providing the basis for energy from solar cells. Semiconductors may be elemental materials such as silicon and germanium, or compound semiconductors such as gallium arsenide and indium phosphide, or alloys such as silicon germanium or aluminum gallium arsenide [46].

Electronic Band Structure

In solid state physics, the electronic band structure (or simply band structure) of solid describes the range of energies that an electron within the solid may have (called energy bands, allowed bands, or simply bands) and ranges of energy that it may not have (called band gaps or forbidden bands).

Band Theory

Devices these band and band gabs by examine the allowed quantum mechanical wave's functions for an electron in a large, periodic of atoms or molecules. Band theory has been successfully used to explain many physical properties of solid, such as electrical resistivity and optical absorption, and forms the foundation of the understanding of all solid-state devices (transistors, solar cells, etc).

Band Gaps

Are essentially leftover ranges of energy not covered by any band, a result of the finite widths of the energy bands? The bands have different widths, with the widths depending upon the degree of overlap in the atomic orbital's from which they arise. Two a adjacent bands may simply not be wide enough to fully cover the range of energy. For example, the bands associated with core orbital's (such as 1_s electrons) are extremely narrow due to the small overlap. As a result, there tend to be large band gaps between the core bands. Higher bands involve larger and larger orbital with

more overlap, becoming progressively wider and wider at high energy so that there are no band gaps at high energy [47].

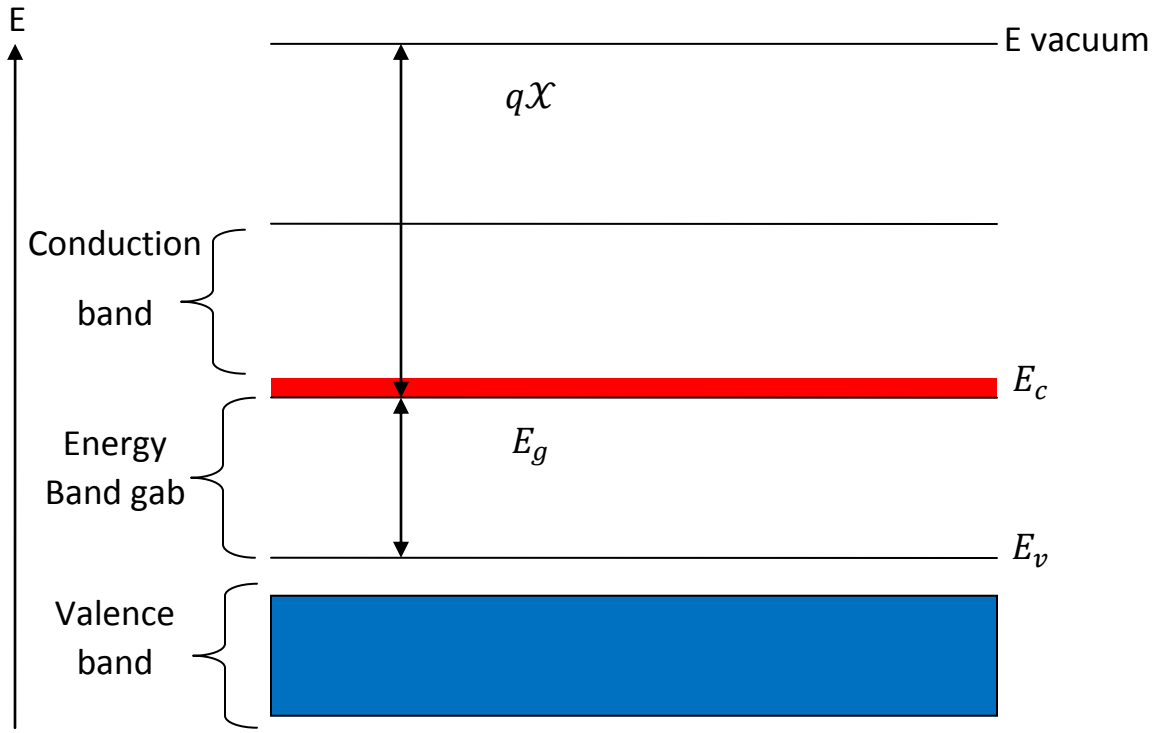

Figure (2-1) A simplified energy band diagram

Used to describe semi-conductors. Shown are the valence and conduction band as indicated by the valence band edge, E_v, and the conduction band edge, E_c, the vacuum level, E_{vacuum}, and the electron affinity, $\mathcal{X}$, and also indicated on the figure [48].

Doping

Doping means the introduction of impurities into a semiconductor crystal to the defined modification of conductivity tow of the most important materials silicon can be doped with, are boron (3 valence electrons = 3 – valent) and phosphorus (5 valence electrons = 5 – valent). Other materials are aluminum, indium (3 – valet) and arsenic, antimony (5 – valent).

The dopant is integrated into the lattice structure of the semiconductor crystal, the number of outer electrons define the type of doping – elements with 3 valence electrons are used for p-type doping, 5 – valued elements for n – doping. The conductivity of a deliberately contaminated silicon crystal can be increased by a factor of 10^6 [49-50].

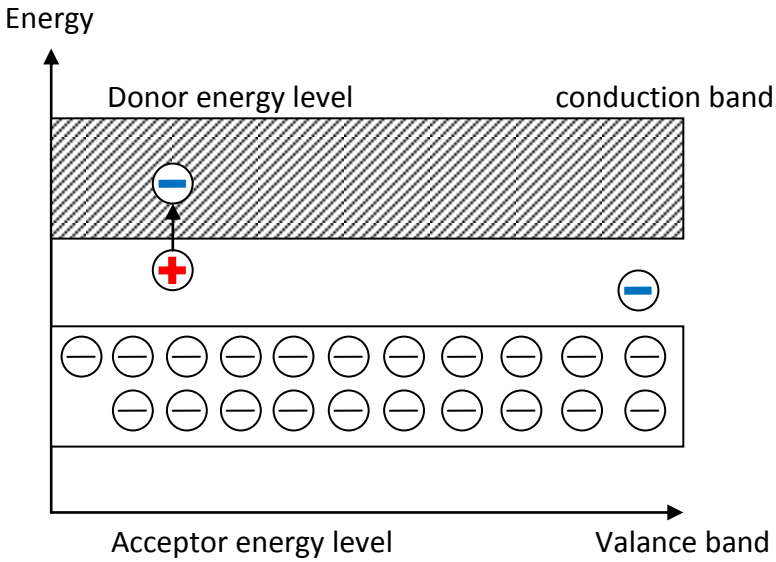

⊕ Positively charged donor Atom.

⊖ Negatively charged acceptor atom.

Figure (2.2) Doping in band structure

2.2 The different materials in a solar cell

2.2.1 Light absorber

The PV conversion process requires a number of materials having suitable electrical, electronic and optical properties that are fundamental to solar cell operation. The key material is the light absorber that is capable of excited stated produced by photon absorption with energies in the photon – rich range of the solar spectrum.

These excited states must be capable of being converted to free electrons and holes that can be collected externally. Commercial solar cells typically employ absorber materials that and inorganic semiconductor.

The ability of an absorber to absorb light of different wave lengths is defined of wavelengths is defined by its absorption coefficient α that is a function of wavelengthsλ . Beer – Lambert's law is applies to calculate the a absorbance A relative to the incident flux intensity I (photons impinging per cm^2 per second), some of which is reflected (R) off the material surface on which it is incident (always referred to as the "front" end) and some transmitted (T) so that light emerges from the opposite side (always reflected to as "back" end) of the material. [18]

Based on this low, the absorbance A as a function of λ is given by equation: [2-1].

$$A(\lambda) = [1 - R].[1 - \exp(-\alpha(\lambda)d] \qquad (2-1)$$

Where d is the thickness of material traversed by the light radiation.

It is seen from Eq-(2-1) that the absorption increases exponentially with α of material thickness d. It is there for desirable to use thick material layers and /or semiconductors that have high absorption coefficients so that the value A can be maximized. The absorption length L_{abs} is a quantity used to denote absorption characteristics, and is defined as the thickness required absorbing 63% of the potential J_{sc} available [18]. This value corresponds to the α.d prodnct equaling I in the exponent maybe defined as the reciprocal of absorption length, and vice versa.

2.2.2 Schottky barrier

In addition to the absorber there are a number of other material components in a solar cell structure. They may include material layers that Plock on type of charge carrier while supporting transport of the other to help promote motion of one type of charge carriers in a different direction to the other. Such layers when used in conjunction with the absorber create a build – in electric field or chemical potential (on effective field) that breaks symmetry and forces electrons in one direction and holes in the other. This region is typically called a junction and forms the building block or a PV device system. [18].

2.2.3 Ohmic contacts

Conducting materials are typically used at either ends of the PV cell and provide the contacts of the cell electrodes and the grids needed for carrying the current to the external load. These materials must produce minimal electrical (voltage) and optical loss, and my metals or transparent conductive oxides (TCOs).

Metal are excellent ohmic contacts because of their low resistivity.

It is a general rule that one must use a large work function metal as contact to P-type semiconductor materials (such as light absorbers) [18].

2.3 Contact Materials

2.3.1 Metal Contacts

Metals are excellent for contact due to their low resistivity. As a general “rule of thumb”, one wants to use a large work function metal as the contact to p-type semiconductor materials, whether inorganic or organic. If a metal with a work function less than that of a given p-type material were used to contact the p-type

semiconductor, $\emptyset wm \geq \emptyset wp$ where $\emptyset wm$ is the metal work function and $\emptyset mp$ is the p-type semiconductor work function.

This situation produces a dipole- oriented negative in the metal and positive in the semiconductor, this large- work function case produces an ohmic contact for holes in p-type materials. The obvious corollary to this work function "rule of thumb" is that one wants to use a low –work function metal as the contact to n-type semiconductor materials, whether inorganic or organic [19].

2.3.2 transparent contacts

These materials are utilized to maximize light entry in to the cell structure while still providing properly positioned electrodes [18] they must have high transparencies, high conductivities and suitable work function.

Since a absorption in these materials is achieved through doping (alloying), there is a trade – off between conductivity and light transmission.

Some commonly employed materials of such roles include tin oxide, indium tin oxide (ITO) and fluorine – doped tin oxide (FTO).

2.4 P-n Junction

It is important to realize that the entire semiconductor is a single – crystal material in which one region is doped with acceptor impurity atoms to form the p– region and the adjacent region is depend with donor atoms to from the n- region. The interface separating the n and p regions is referred to as the metallurgical junction [20].

The impurity doping concentrations in the p and n regions figure (2-1a) shows the p-n junction and (2-1b) shows the impurity doping concentration in the p and n regions.

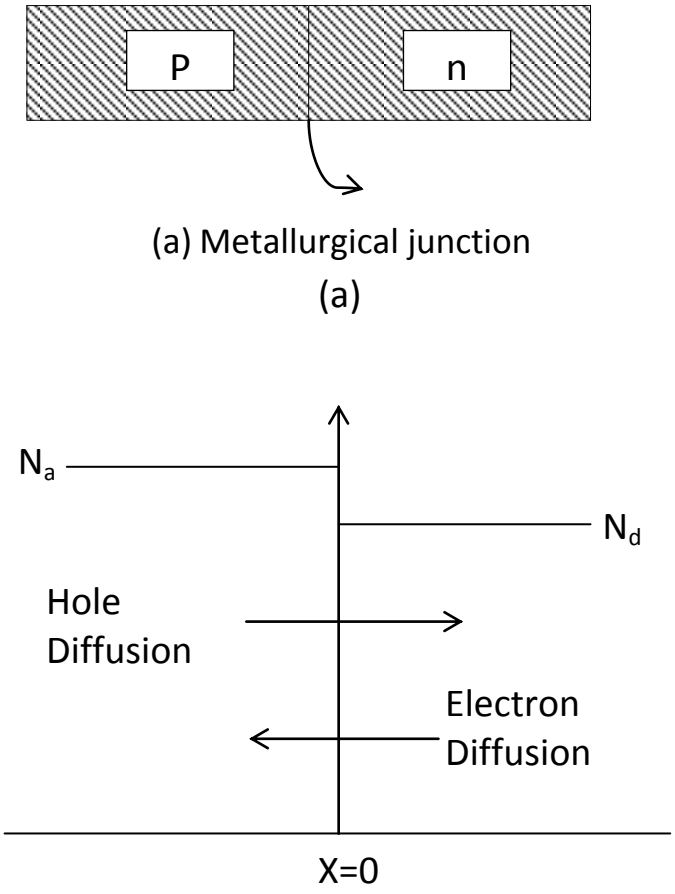

Figure (2-3) (a) simplified geometry of a p n junction (b) doping profile of an ideal uniformly doped p n junction

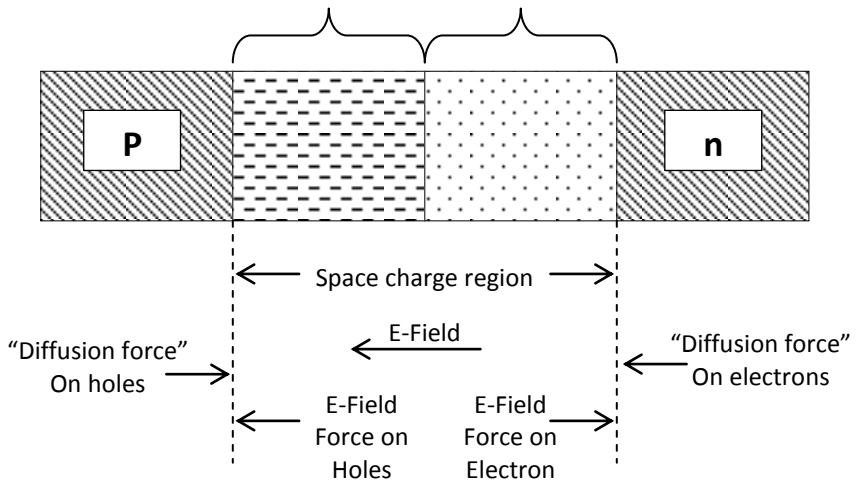

Figure (2-4) the space charge region, the electric field, and forces acting on the charged carriers

For simplicity, we will consider a step junction in which the doping concentration is uniform in each region and there is an abrupt change in doping at the junction. Initially, at the metallurgical junction, there is a very large density gradient in both the electron and hole concentrations. Majority carrier electrons in the n- region will begin diffusing into the p- region and majority carrier holes in the p-region will begin diffusing into the n – region. If we assume there are no external connections to the semiconductor, then this diffusion process cannot continue indefinitely.

As electrons diffuse from the n-region, positively charged donor atoms are left behind. Similarly, as holes diffuse from the p-region, they uncover negatively charged acceptor atoms. [20].

The net positive and negative charges in the n and p regions induce and electric field in the region nears the metallurgical junction, in the direction from the positive to the negative charge, or from the n to the region.

The net positively and negatively charged regions are shown in figure (2-2) these two regions are referred to as the space charge region.

Essentially all electrons and holes are swept out of the space charge region by the electric field. Since the space charge region is depleted of any mobile charge, this region is also referred to as the depletion region; these two terms will be used interchangeably.

Density gradients still exist in the majority carrier concentration at each edge of the space charge region. We can think of a density gradient as producing a “diffusion force” that acts on the majority carriers. These diffusion forces, acting on the electrons and holes at the edges of the space charge region. The electric field in the space charge region produces another force on

the electrons and holes which is in the opposite direction to the diffusion force for each type of particle. In thermal equilibrium, the diffusion force and the E- field force exactly balance each other [20].

2.5 Silicon Solar Cells

(Crystalline and amorphous (C- Si and a – Si))

The Si – based p-n homojunction PV cells have been long employed globally for producing electricity from solar energy. It is the most well – Understood semiconductor technology in the world, benefitting from decades of development by the integrated circuit (IC) industry.

The advantages of Si – based PV include the availability [21], of well – established the techniques for controlling and manipulating the electronic and physical properties of doped homojunctions and the crystal abundance of the element on the earth's surface [22].

Mutt crystalline silicon (Mc – Si) remains the global leader of PV products with a 45% market share that has reduced in the past few years with the rapid growth of the industry based on commercialization of the monocrystalline variety and the CdTe thin films [22].

The single crystal Si device (Sc – Si) have become increasingly popular because of their higher cell (and module) efficiencies (25 and 21% respectevtively) compared to mc-Si (20 – 5% and 17% respectively), attend that can be attributed to a combination of superior properties such as low internal resistance from defects and impurities and improvements in wire cutting technology that has enable reductions in wafer thickness's to about 180μm at present [22]. It must be noted that ideal C-Si calls would require only about 20 μm of absorber material to absorb 95% of

the incident radiation, based on their (α) values that are typically 10^3 Cm^{-1} [3].

2.6 The Efficiency of a solar cell

Figure (3.3) shows a plot of the possible J-V operating points, called the "light" J-V characteristic of the PV cell. The points labeled J_{sc} and V_{oc} represent, respectively the extreme cases of no voltage produced between the opposite ends of the device (i-e. the illuminated the cell is at short – circuit condition) and of no current flowing between the two ends (i-e- illuminated cell is open – circuit condition).

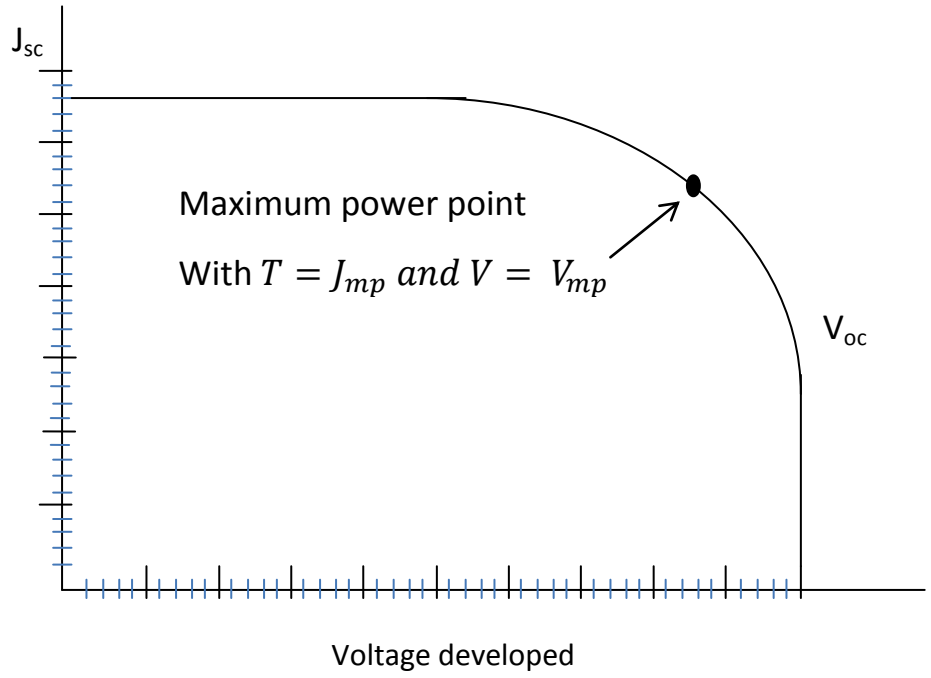

Figure (2.5) typical (I-V characteristic of photovoltaic structure under illumination)

It must be noted that the power output (defined) as J.V product at any point) has its highest value at the maximum power point corresponding to the values of J_{mp} and V_{mp} in figure (2.3).

The definition of these quantities helps define the thermodynamic efficiency η (eta) of the PV conversion process in terms of the input power P_{input} as:

$$\eta = J_{mp}.V_{mp}/P \qquad (2-2)$$

It can be seen from figure (3.3) that's an ideal shaped J-V curve would be rectangular and would deliver a constant current density I_{sc} up to the open – circuit voltage V_{oc}.

A term called the fill factor FF is hence used to measure how close a given characteristic is to conforming to this ideal rectangular J-V shape the fill factor, by definition, is ≤ 1.

The efficiency of a PV device can now be defined in terms of the fill factor as:

$$\eta = FF.J_{sc}\,.V_{oc}/pinput \qquad (2-3)$$

It is evident that the two major parameters governing efficiencies in solar cells are short – circuit current density J_{sc} and open – circuit V_{oc}. Consequently, improvements to PV conversion efficiencies involve increasing J_{sc} of V_{oc} values or both [22].

2.7 Photovoltaic characterizations

2.7.1Real Solar Cells

For a real solar cell, the effect of parallel resistance R_{sh} (shunt resistance due to leakage current, e.g. by local shorts of the solar cell) and serial resistance R_s (due to ohmic loss) must be considered.

$$In\left(\frac{I+I_L}{I_s}-\frac{V-IR_s}{I_sR_{sh}}+1\right)=\frac{e}{kT}(V-IR_s) \qquad (2-4)$$

The serial resistance affects the filling factor more strongly than the shunt resistance (Fig (2-4).

$$I = I_s \left[\exp\left(\frac{e(V - IR_s}{kT}\right) - 1\right] - I_L. \qquad (2-5)$$

In the example of Fig 2.4, a serial resistance of 5Ω reduces the filling factor by a factor of about four [34].

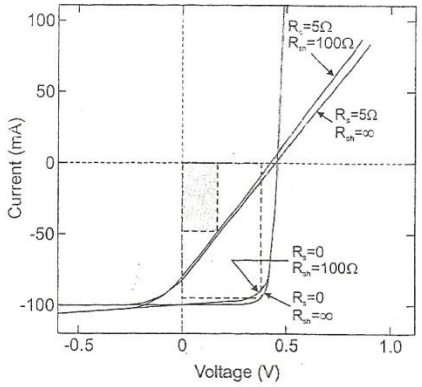

Fig (2.6) I-V characteristics of a solar cell considering shunt and series resistances R and R_h, respectively. The efficiency of the real cell (shaded power rectangle) is less than 30% of that of the ideal cell.

2.7.2 ideal conversion Efficiency

The conventional solar cells, typically a p-n Junction, have a single band gap E_g. When the cell is exposed to the solar spectrum, a photon with energy greater than E_g makes no contribution to the cell output (neglecting phonon assisted absorption). A photon with energy with energy greater than E_g contributes an electric charge to

the cell output, and the excess energy over E_g is wasted as heat. To derive the ideal conversion efficiency.

We shall consider the energy band of the semiconductor used. The solar cell is assumed to have ideal diode I-V characteristics. The equivalent circuit is shown in fig (2.5)

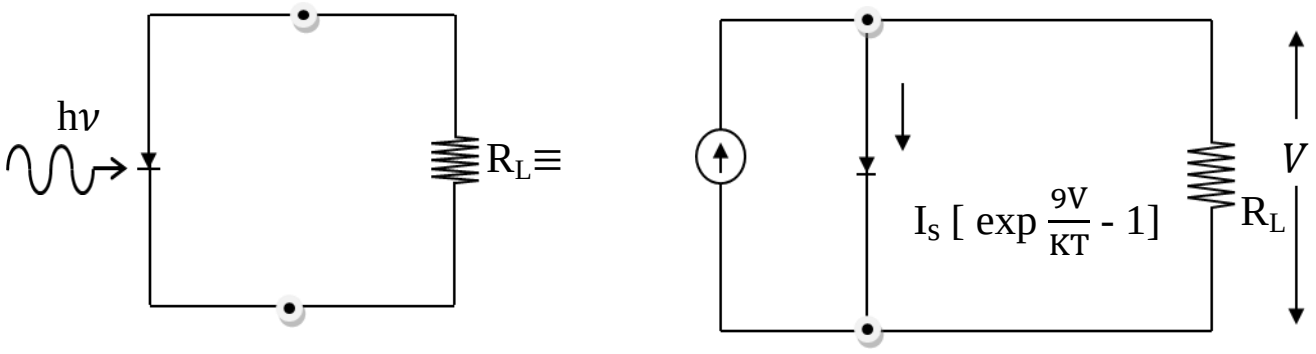

Fig. (2.7) Idealized equivalent circuit of solar cell under illumination.

Where a constant – current source of photo current is in parallel with the Junction. The source I_L results from the excitation of excess carriers by solar radiation, I_s is the diode saturation current and R_s is the load resistance. To obtain the photocurrent I_L, need to integrate the total area under the graph shown fig (2-8)

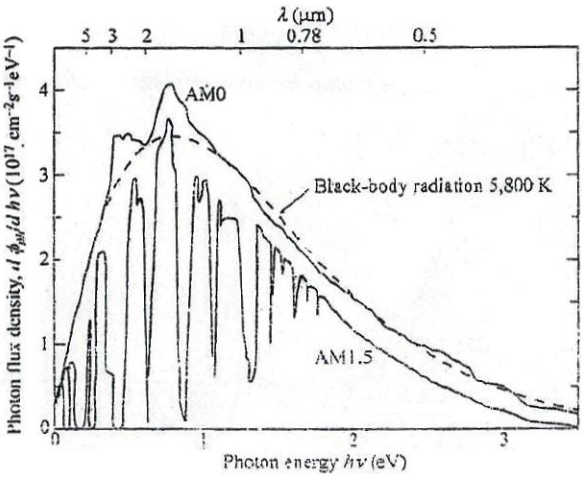

Fig (2.8) Solar spectrum in photon flux density per photon energy for AM0 and AMI-5 radiation.

$$That\ is\ , I_L\ (E_a)\ =\ Aq \int_{h\upsilon=Eg}^{\infty} \frac{d\,\phi\,ph}{dh\upsilon} d(h\upsilon) \qquad (2-6)$$

The result is show in fig (2.9) as a function of the band gap of the semiconductor. For the photo current consideration, the smaller band gap the better because more photons are collected.

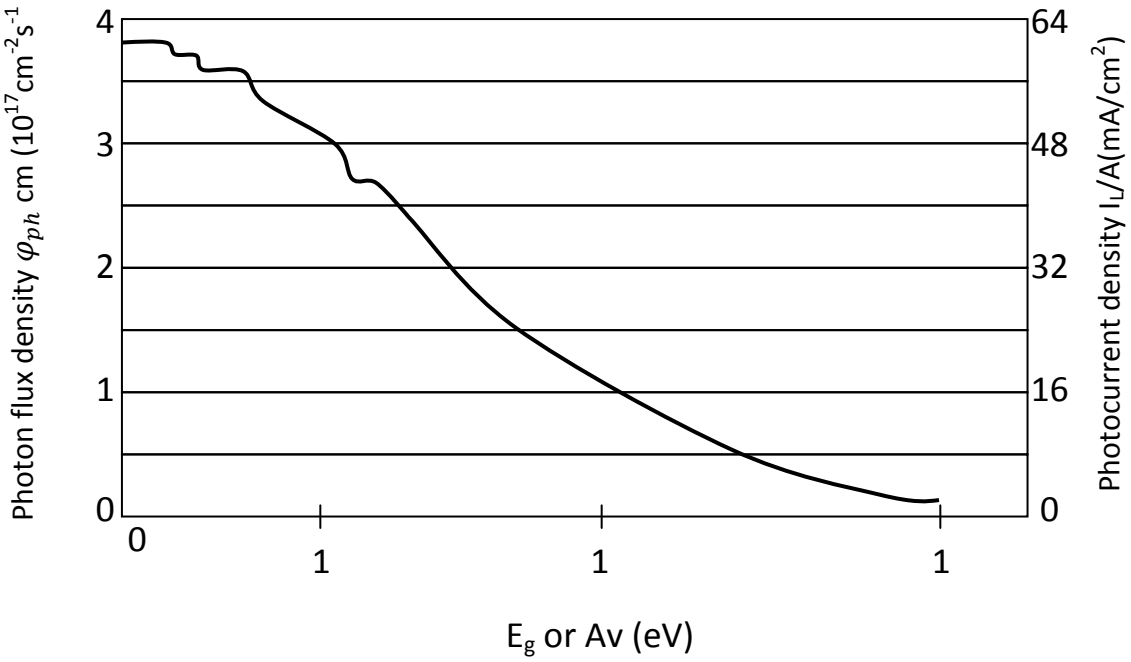

Fig (2.9) Total number of photons in the solar spectrum (of AMI-5) above an energy value. Contributing to the maximum photo current for a solar cell made with specific E_g.

The total I-V characteristics of such a device under illumination is simply a summation of the dark current and the photocurrent, given as

$$I = I_s \left[\exp\left(\frac{qV}{KT}\right) - 1\right] - I_L \qquad (2-7)$$

From equation (2-7) We obtain the open – circuit voltage by setting I= 0:

$$V_{oc} = \frac{KT}{q} Ln \left(\frac{I_L}{I_s} + 1\right) \approx \frac{KT}{q} \ln\left(\frac{I_L}{I_s}\right) \qquad (2-8)$$

Hence for a given I_L, the open-circuit voltage increases logarithmically with decreasing saturation current I_s. For a regular p-n Junction, the ideal saturation current is given by:

$$I_s = Aq\, N_c\, N_v \left[\frac{1}{N_A}\sqrt{\frac{D_n}{\zeta_n}} + \frac{1}{N_D}\sqrt{\frac{D_p}{\zeta_p}}\right] \exp\left[\frac{-Eg}{KT}\right] \qquad (2-9)$$

As seen, I_S decreases exponentially with Eg. So the obtain a large V_{oc}' a large Eg. Is required.

Qualitatively, we know the maximum V_{oc} is the built – in potential of the Junction, and the maximum built- in potential is close to the energy gap. A plot of equation (2-7) is given in fig (2-12).

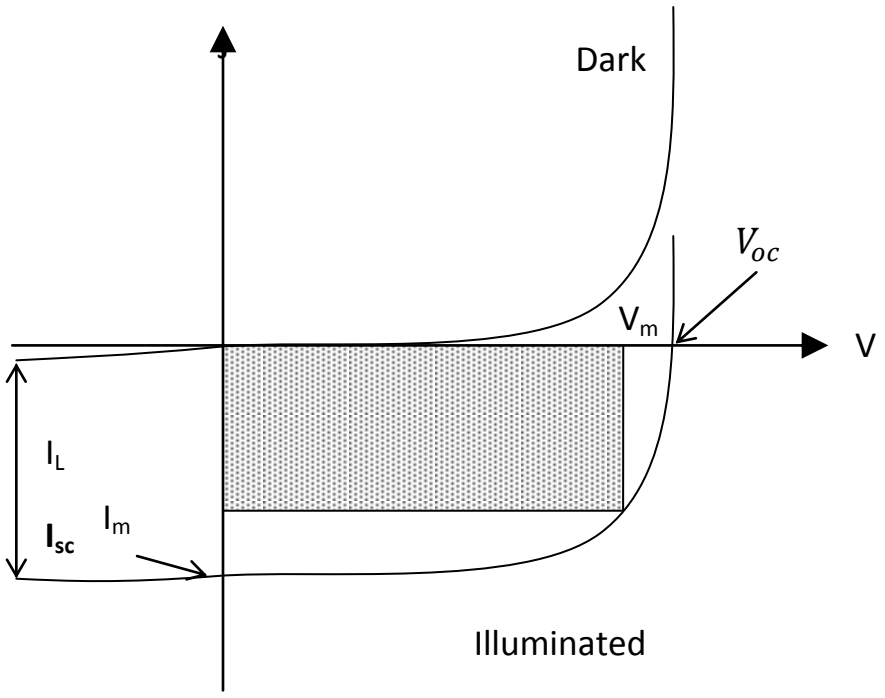

Fig (2-10) I-V Characteristics of solar cell under illumination. Determination of illuminated power output is indicated

The curve passes through the fourth guardant and, therefore, power can be extracted from the device to a load. By properly choosing a load, close to 80% of the product I_{sc} V_{oc} can be extracted.

Here I_{sc} is the short- circuit current which is equal to the photocurrent derived. The shaded area is the maximum power output. We also define in Fig (2.10) the quantities I_m and V_m that correspond to the current and voltage. For the maximum power output P_m (= I_m V_m).

To derive the maximum-power operating point, the output power is given by:

$$P = IV = I_S V[\exp\left(\frac{qV}{KT}\right) - 1] - I_L V \qquad (2-10)$$

The condition for maximum power can be obtained when

$$dp/dv = 0, \text{ or}$$

$$I_m = I_s \beta V_m \exp(\beta V_m) \approx I_L(1 - \frac{1}{\beta V_m}) \qquad (2-11)$$

$$V_m = \frac{1}{\beta}\ln\left[\frac{I_L/I_S + 1}{1 + \beta V_m}\right] \approx V_{oc} - \frac{1}{\beta}\ln(1 + \beta V_m) \qquad (2-12)$$

Where $\beta = q/kT$ .the maximum power output P_m is then

$$P_m = I_m V_m = FF I_{sc} V_{oc} \approx I_L[V_{oo} - \frac{1}{\beta}\ln(1 + \beta V_m) \qquad (2-13)$$

Where the full factor FF measures the sharpness of the curve and is defined as:

$$FF \equiv \frac{I_m V_m}{I_{sc} V_{oc}} \qquad (2.-14)$$

In practice a good fill factor as around 0.8.

The ideal conversion efficiency is the ratio of the maximum power output to the incident power P_{in}

$$\eta = \frac{P_m}{P_{in}} = \frac{I_m V_m}{P_{in}} = \frac{V_m^2 I_s \left(\frac{q}{KT}\right) exp(qV_m/KT)}{Pin} \quad (2-15)$$

Theoretically, the ideal efficiency can be calculated. We have shown that the photocurrent increases with smaller E_g. On the other hand, the voltage increases with E_g. By having a small saturation current.

So to maximize the power, there exists an optimum value for the band gap E_g. Furthermore, by using the ideal saturation current of E.g. (2.8) in relation to E_g, the theoretical maximum conversion efficiency can be calculated [35].

2.7.3 Nonideal Effects

For a practical solar cell, the ideal equivalent circuit, fig (2.5) be modified to include the series resistance Rs from ohmic loss in the front surface and the shunt resistance R_{sh} from leakage currents.

The equivalent circuit should include Rs added in series with the load $R_{L'}$ and R_{sh} added in parallel with the diode. The diode I-V characteristics are found to be modified from Equation (2-7) to:

$$\ln\left(\frac{I+I_L}{I_s}-\frac{V-IR_s}{I_sR_{sh}}+1\right)=\frac{q}{KT}(V-IR_s) \qquad (2-16)$$

In practice, the shunt resistance has much less affected them the series resistance. The effect of R_s can be simply obtained by replacing V with (V- IR_s), and the main impact is on the fill factor.

For practical solar cells, the forward current can be dominated by the recombination current in the depletion region. The efficiency is recued with that of an ideal diode. The recombination current is in the form.

$$I_{re}=I_s\left[\exp\left(\frac{qv}{2kT}\right)-1\right] \qquad (2-17)$$

The energy conversion equation can again be put into closed form yielding equations similar to E.q (2-7) through (2-13), with the exception that I_s is replaced by $\acute{I}_s$ and the exponential factor is divided by 2.

The efficiency for the case of recombination current is found to be much less than the ideal – current case due to degradation of both V_{oc} and the fill factor. For solar cells having mixtures of diffusion current and recombination current, or current due to other defects, the forward current shows an exponential dependency on the forward voltage as ($e^{\frac{qv}{nkT}}$), where n is celled the ideality factor and

is generally between 1-2. The efficiency decreases with increasing values of n.

As the device temperature increases, the diffusion lengths will increase because the diffusion constant stays the same or increases with temperature, and the minority carrier lifetime increases with temperature.

The increases in mining- carrier diffusion length will increases the photocurrent I_L. However, V_{oc} will rapidly decrease because of the exponential dependence of the saturation current on temperature.

The degradation in the softness in the knee of the I-V curve as temperature increases will also decrees the fill factor. Therefore, the overall effect causes a reduction of efficiency as the temperature increases. This presents a challenge for operation under optical concentrators [2].

2.7.4 The Equivalent circuit diagram (ECD)

ECDs are frequently used to describe the electric behavior of more complex semiconductor devices with a network of ideal electrical components such as diodes, current of voltage sources and resistors.

Fig (2.11) show as the ECD that the typically used for inorganic solar cells.

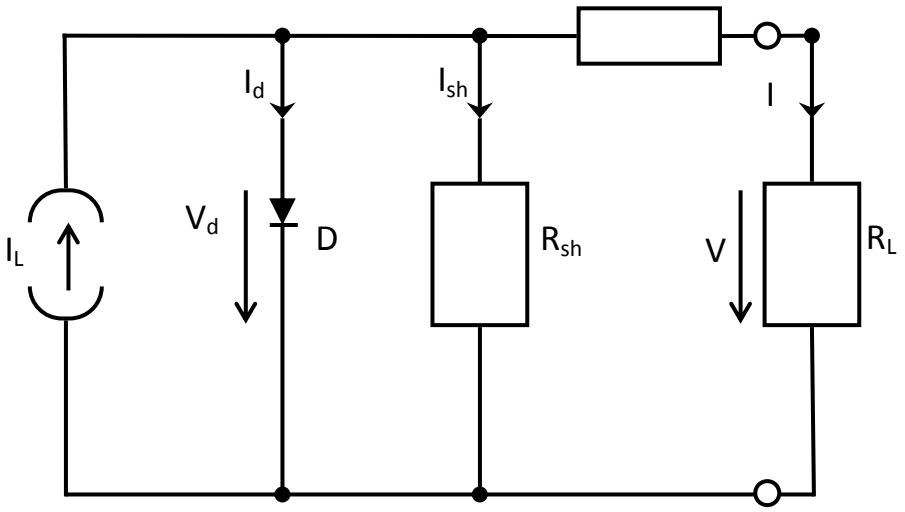

Fig (2.11): ECD of a solar cell.

The circuit consists of the following ideal components:

A current source I_L that considers the light-generated current, a diode that accounts for the nonlinear voltage dependence and a shunt as well as a series resistor.

Also shown are a load resistor R and its voltage drop and current. The current arrows point into the direction the holes flow- according to the standard in electronics. The current I is negative if $V > V_{oc}$ and it flows "into" the device- otherwise it is positive.

Although the specific physical processes in organic semiconductors may by different and therefore lead to other parameters, the principal loss mechanisms are the same and we

may therefore apply the same circuit. suggest to associate the following (more general) processes with the single components in the ECD:

- The current source generates current I_L upon illumination. I_L = number of dissociated exactions/ S = number of free electron / hole pairs immediately after generation-before any recombination can take place.
- The shunt resistor R_{sh} is due to recombination of charge carriers near the dissociation sate (e.g D/A interface). Provided the series resistor R_s is at least one order of magnitude lower than R_{sh}, it may also include recombination further away from the dissociation site e.g. near the electrode. Otherwise an extra shunt resistor R_{sh_2} has to be considered Fig. (2.12)

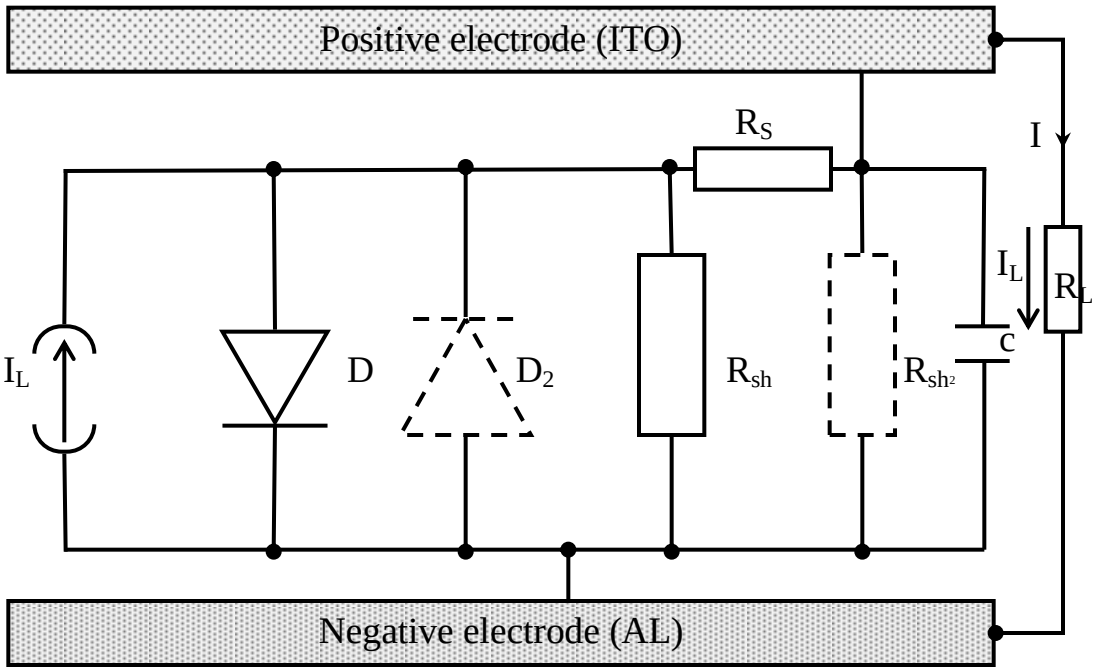

Fig. (2.12) Extended ECD of a solar cell.

The formation of a counter diode D_2 may sometimes need to be considered as well as another shunt R_{sh} that connects the tow electrodes dividedly.

The capacitor accounts for accumulation i.e storage effects of charges and may be of particular interest for AC measurements i.e photocurrent measurements with chopped light.

R_{sh} can be derived by taking the inverse slope around 0V:

$$R_{sh} \approx \left(\frac{1}{V}\right) - 1 \qquad (2-18)$$

This is because at very small voltages the diode D is not conducting and the current driven by the external voltage (positive of negative) is only determined by R_{sh} + R_s with R_{sh} (typically) being much larger.

- The series resistor Rs considers conductively i.e. mobility of the specific charge carrier in the respective transport medium. For example mobility of holes in a p- type conductor or electron donor material. The mobility can be affected by space charges and traps or other barriers (hopping). R_s is also increased with a longer traveling distance of the charges in e.g thicker transport layers. R_{sh} can be estimated from the (inverse) slope as appositive voltage $>$ V_{oc} where the IV curves becomes liner :

$$R_s \approx \left(\frac{1}{V}\right)^{-1} \qquad (2-19)$$

  This is because at high positive external voltages V the diode D becomes much more conducting than R_{sh} so that R_s can dominate the shape of the IV curve.

- Ideal diode D = voltage dependent resistor that takes into account the asymmetry of conductivity due to the built in field in D/A cell (difference between the acceptor LUMO and the donor it (HOMO) or the nature of the semiconductor

electrode interface (blocking contact) in single layer cells. This diode is responsible for the nonlinear shape of the IV curves.

The diode characteristic is not necessarily Shockley type. Not that the IV characteristic of ideal diode D is only equal to the IV characteristic of the entire cell (circuit) if:

$$R_s = 0\ \Omega \quad \text{and} \quad R_{sh} = \infty\ \Omega$$

0Solar cell voltage V. the cell can great a voltage between 0 and V_{oc} depending on the size of the load resistor. In other to obtain IV curve data in other voltage ranges (V< O and V_{oc} < V) in IV curve an external voltage source is required. We note that also the voltage drop across a load resistor. The range between 0 and V_{oc} can be simulated by the same voltage source so that the entire range can be scanned by applying an external voltage.

Not that the current for V > V_{oc} and the extra current for V < 0V is delivered from the external voltage source. The external voltage source can then act as a current amplifier to boost the photo sensitivity but the actual photon to current conversion efficiency (EQE) of the solar cell or photo diode cannot really be increased.

These are the components of an ECD with which we can associate the most important effects in solar cells of all types. However, a

more comprehensive ECD for organic devices – see Fig (2.12) may comprise the following extra components:

- Another diode D_2. The formation of an extra blocking contact (e.g for holes at the ITO electrode) can affect the IV curve in the third quadrant or even lead to FF values < 0.25.
- Note that the normal blocking contact for electrons at ITO and holes at AL allows charge injection into the electrodes if sufficiently high negative voltage is applied.
- The capacitor C. the capacitor that takes into account charging / discharging and other time dependent effects that can be significant since the contact area A can be large and the distance between the electrical is very small:

$$C = \epsilon \frac{A}{d}$$

- An extra shunt resistor R_{sh_2}. it considers shorts due to p in holes or significant conductivity of the bulk material. It may also account for recombination losses near the electrodes. The effect of R_{sh_2} if R_s is considerably smaller than any of the tow shunts.

We note that current and resistor values depend on the illuminated area and need to be related to it, if comparisons between cells with different illumination areas are desired.

Note that the dark current depends on the actual device area – regardless of the size of the light spot. Using the simple ECD in fig. (2.11) and Kirchhoff's laws for current knotes and voltage loops, we can formulate the following relation:

$$\overbrace{(I_L - I_d - I)}^{I_{sh}} R_{sh} = V + IR_s \qquad (2-20)$$

Which can be transformed in to?

$$I\left(\frac{Rs}{R_{sh}} + 1\right) = I_L - I_d - \frac{V}{R_{sh}} \qquad (2-21)$$

If we now assume that the Shockley diode equation describes the voltage dependence of the current I_d through the ideal diode D

$$I_d = I_o\left(e^{\frac{V-IR_S}{\frac{nKT}{q}}} - 1\right) \qquad (2-22)$$

And replace I_d in Eg. (2.21) we obtain

$$I = \left(I_L - \frac{V}{R_{sh}}\right)\frac{R_{sh}}{R_{sh}+R_s} - I_0\frac{R_{sh}}{R_{sh}+R_s}\left(e^{\frac{V-IRs}{\frac{nKT}{q}}} - 1\right) \qquad (2-23)$$

If we now use

$$R_{sh} + \frac{R_s}{R_{sh}} = 1 + \frac{R_s}{R_{sh}} \qquad (2-24)$$

We can write Eg. (2-19) as

$$I = \frac{I_L - \frac{v}{R_{sh}}}{I + \frac{R_s}{R_{sh}}} - \frac{I_0}{L + \frac{R_s}{R_{sh}}}\left(e^{\frac{v - IR_s}{\frac{nkT}{q}} - 1} \right) \qquad (2-25)$$

This equation will be used from the specific shapes of IV characteristics.

Inorganic solar cells have R_s values between 0.3 Ω and a few ohms and R_{sh} larger than 1000 Ω so that the ration $\frac{R_s}{R_{sh}}$ is very small and the term $1+\frac{R_s}{R_{sh}}$ is virtually 1 and can therefore be neglected in Eg. (2-21). However, even in silicon solar cells the voltage drop across R_s represents an important loss factor and has to be considered as well as the loss current through the shunt. Note that both R_s and R_{sh} still appear in E_g. (2-21) even though $1 + R_s/R_{sh}$ can be neglected.

However the situation can be very different for organic cells.

Organic cells very often suffer from high series resistors and – in addition – relatively small R_{sh} values. As a consequence not only the losses due to both resistors are higher than in silicon cells but also the term $1 + R_s/R_{sh}$ can become significantly different from 1 and has to be considered in Eg. (2.23)

As a result, the shape of the IV curves and the absolute currents are more affected by these resistor values in organic than in inorganic cells [4].

2.8 Interpretation of IV Characteristics

2.8.1 Inorganic Solar Cell

The higher charge carrier mobility in inorganic semiconductors leads to sufficiently long diffusion lengths which allow most charge carriers to reach the electrodes before they undergo intense recombination- even though the devices are about 1000 times thicker. In addition R_{sh} is typically more than 3 orders of magnitude larger than R_s. This not only leads to a negligible term $I + \frac{R_s}{R_{sh}}$ in Eqn (2.23), but also makes it much easier to distinguish the effects of the tow resistors in the IV characteristics.

In addition the reverse saturation current I_0 is typically larger than in organic devices.

However, clearly smaller R_{sh} values have enormous bad effects on the I-V curve. However, the short circuit current is not affected since the current through the shunt can be neglected if $R_s << R_{sh}$ [4].

2.8.2 Design Refinements

In order to collect electrons most efficiently, a back surface field is used (Fig. (2.11). A higher- doped region at the back contact creates a potential barrier and reflects electrons back to the front contact.

An important point for optimization is the management of the reflection at the solar cell surface. First, dielectric antireflection (AR) multilayer's can used. These layers should have a broad AR spectrum. Additionally, a textured surface, as schematically shown in Fig (2.12a), e.g. created by anisotropic etching of Si (001) (Fig. 2.12c), reduces reflection (Fig. 2.12b). The reflectivity of bare Si, 35%, can be reduced to 2%. An AM0 efficiency of 15% was reached using textured cells.

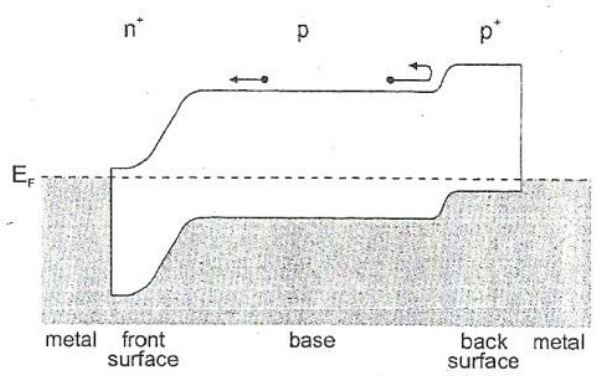

Fig. (2.13). Increase of the carrier collection efficiency by a back surface field.

During its course over the sky during the day, the sun changes its angle towards a fixed solar cell. A tracking mechanism can optimize the angle of incidence during the day and increase the overall efficiency of the solar cell (Fig.2.15) [34].

2.8.3 Solar-Cell Types

Silicon is the most frequently used material for solar cells. Cells based on single-crystalline silicon (wafers) have the highest efficiency hut are the most expensive (Fig. 2.16a). Polycrystalline silicon (Fig. 2.16b) is cheaper but offers less performance material design is oriented towards increasing the grain size. These solar cells are also called ‘first-generation’ photovoltaic.

Thin sheets of crystalline silicon drawn from a melt between two seed crystals in a modified CZ growth (sheet silicon or ribbon silicon) allow cheaper

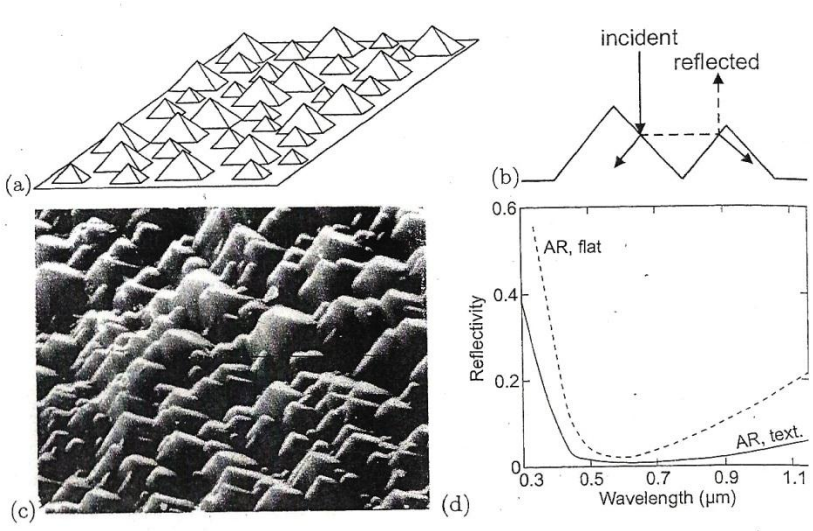

Fig.(2.14 (a) Schematic surface topology of a textured solar cell. (b) Exemplary light path. (c) SEM image of a textured surface (pyramid base: 5pm). (d) Reflectivity of antireflection-coated flat (dashed line) and textured (solid line) surface).

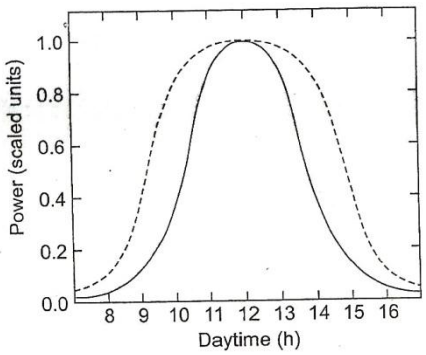

Fig. (2.15). Power generation of a solar cell vs. time (in daytime hours) for a stationary setup facing the sun at constant angle (solid line) and mounting with tracking (dashed line) to optimize the angle towards the sun.

Production compared to cells based on ‘traditional’ polished wafers cut from a large silicon rod.

Even cheaper are solar cells from amorphous silicon (Fig. (2.16c). since silicon is an indirect semiconductor, a fairly thick layer is needed for light absorption. If direct semiconductors are used, a thin layer (d ~ 1 μm) is sufficient for complete light absorption. Such cells are called thin-film solar cells. A typical material class used in this type of cell are chalcopyrite's, such as CuInSe2 (CIS). The band gap is around 1 eV, which is not optimal. An improvement can be achieved by adding Ga and/or S that increases the band gap, Cu (In,Ga)(Se,S)$_2$ (CIGS), to 1.2—1.6 eV. Using CIGS, an efficiency of 15% has been reported. Thin-film solar cells can be fabricated on glass substrate or on flexible polymer substrate such as Kapton (Fig. 2.17a,b).

Also here, optimization of the grain size is important (Fig. 2.17b). As the front contact, a transparent conductive oxide (TCO), such as ITO ($InSnO_2$) or ZnO:Al, is used. Thin-film and amorphous silicon solar cells are also termed ‘second-generation’ photovoltaic.

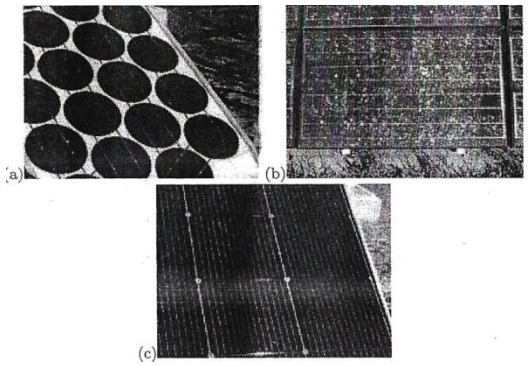

Fig.(2.16). Various types of solar cells: (a) monocrystalline silicon solar cell, (b) polycrystalline solar cell, (e) amorphous silicon solar cell.

In order to cover a large area and supply certain values of output voltage and current, several solar cells are connected into modules. Arrays are built up from several modules (Fig. 2.18) if solar cells are connected in parallel, the total current increases; if they are connected in series, the output voltage increases.

'Third-generation' photovoltaic attempt to go beyond the 30% limit and comprise of multifunction solar cells. concentration of sunlight use of hot carrier excess energy as discussed above and possibly other concepts including photon conversion.

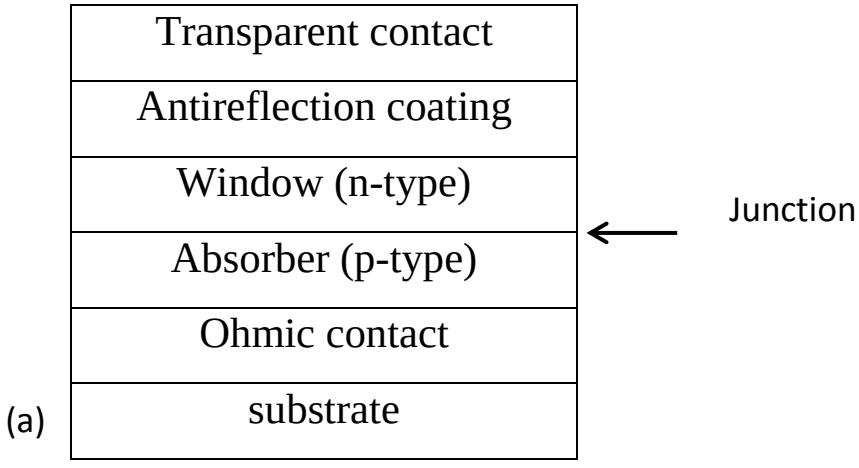

(a)

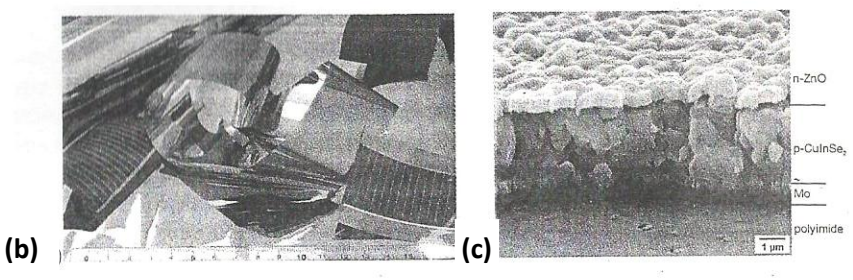

Fig.(2.17). (a) Schematic cross section of a polycrystalline thin-film solar cell. (b) Rolled sheets of CIS thin film solar cell on flexible Capton foil. (c) SEM cross section of CIS thin-film solar cell [34].

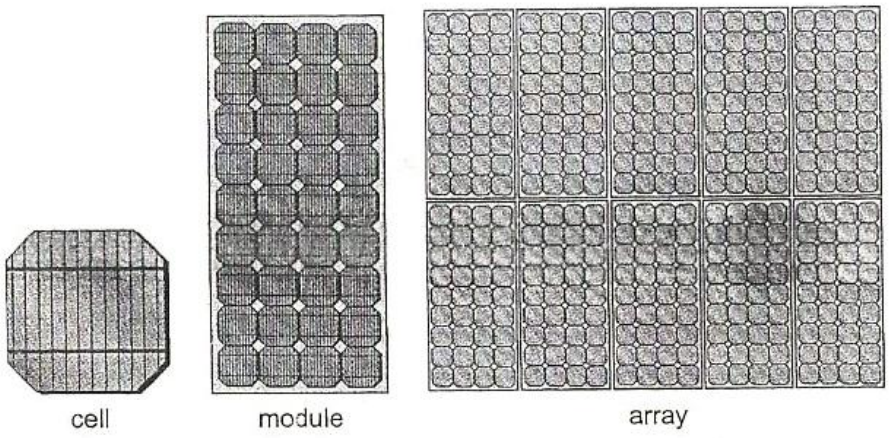

Fig.2.18. Schematic drawing of a solar cell (with contact grid), a module (36 cells) and an array of ten modules

2.9 Solar cell efficiency tables (version 37)

Since January 1993, 'Progress in Photovoltaic' has published sis monthly listings of the highest confirmed efficiencies for a range of photovoltaic cell and module technologies By providing guidelines for the inclusion of results into these tables, this not only provides an authoritative summary of the current state of the art but also encourages researchers to seek independent confirmation of results and to report results on a standardized basis. In a recent version of these tables (Version 33).

Results were updated to the new internationally accepted reference spectrum (IEC 60904—3, Ed. 2.2008), where this was possible.

The most important criterion for inclusion of results into the tables is that they must have been measured by a recognized test centre listed elsewhere. A distinction is made between three different eligible areas: total area; aperture area and designated illumination area. 'Active area' efficiencies are not included. There are also certain minimum values of the area sought for the different device types (above 0.05 cm^2 for a concentrator cell, .1 cm^2 for a one—sun cell and 8011cm^2 for a module).

Results are reported for cells and modules made from different semiconductors and for subcategories within each semiconductor grouping (e.g. crystalline. polycrystalline and thin film). From Version 36 onwards, spectral response information has been included when available in the Thon of a plot of the external quantum efficiency (EQE) versus wavelength, normalized to the peak measured value.

2.9.1 New Results

Highest confirmed "one-sun" cell and module results are reported in Tables I and II. Any changes in the tables from those previously published are set in bold type. In most cases, a literature reference is provided that describes either the result reported or a similar result. Table I summarizes the best measurements for cells and sub modules, while Table II shows the best results for modules.

Table III contains what might be described as 'notable exceptions'. While not conforming to the requirements to be recognized as a class record, the cells and modules in this Table have notable characteristics that will be of interest to sections of the photovoltaic community with entries based on their

significance and timeliness, to ensure discrimination, Table III is limited to nominally l0 entries with the present authors having.

Table(2.1).confirmed terrestrial cell and submodule efficiencies measured under the global AM1.5 spectrum (1000W/m^2) at 25°C (IEC 60904-3: 2008, ASTM G-173 – 03 global).

Classification	**Effic.[b] (%)**	**Area[c] (cm^2)**	**V_{oc} (cm^2)**	**J_{sc} (mA/cm^2)**	**FF° (%)**	**Test centre (land Data)**	**Description**
Silicon							
Si (crystalline)	25.0±0.5	4.00(da)	0.706	42.7[f]	82.8	Sandia (3/99)[g]	UNSW PERL
Si (multicrystalline)	20.4±0.5	1.002(ap)	0.664	38.0	80.9	NREL (5/04)[g]	FhG-ISE
Si (thin film transfer)	16.7±0.4	4.017(ap)	0.645	33.0	78.2	FhG-ISE(7/01)[g]	U. Stuttgart (45μm thick)
Si (thin film submodule)	10.5±0.3	94.0(ap)	0.492[h]	29.7[h]	72.1	FhG-ISE (8/07)[g]	CSG Solar(1-2 μm on glass; 20 cells)
III-V cells							

GaAs (thin film)	**27.6±0.8**	**0.9989(ap)**	**1.107**	**29.6**	**84.1**	**NREL(11/10)**	**Alta Devices**
GaAs (multicrystalline)	18.4±0.5	4.011(t)	0.994	23.2	79.7	NREL (11/95)[g]	RTI, Ge substrate
InP (crystalline)	22.1±0.7	4.02(t)	0.878	29.5	85.4	NREL(4/90)[g]	Spire, epitaxial
Thin Film Chalcogenide							
CIGS (cell)	**19.6±0.6**	**0.996(ap)**	**0.713**	**34.8**	**79.2**	**NREL(4/09)**	**NREL, CIGS on glass**
CIGS (submodule)	16.7±0.4	16.0(ap)	0.661[h]	33.6[h]	75.1	FhG-ISE(3/00)[g]	U.Uppsala, 4 serial cells
CdTe (cell)	16.7±0.5[h]	1.032(ap)	0.845	26.1	75.5	NREL(9/01)[g]	NREL, mesa on glass
CdTe (submodule)	**12.5±0.4**	**35.03(ap)**	**0.838**	**21.2[j]**	**70.5**	**NREL(9/10)**	**ASP Hangzhou, 8 serial cells**

Amorphous/nanocrystalline Si							
Si (amorphous)	10.1±0.3[k]	1.036(ap)	0.886	16.75[f]	67	NREL(7/09)	Oerlikon solar Lab, Neuchatel
Si (nanocrystalline)	10.1±0.2[I]	1.199(ap)	0.539	24.4	76.6	JQA(12/97)	Kaneka (2μm on glass)
Photochemical							
Dye sensitized	10.4±0.3[m]	1.004(ap)	0.729	22	65.2	AIST (8/05)[g]	Sharp
Dye sensitized (submodule)	**9.9±0.4[m]**	**17.11(ap)**	**0.719[h]**	**19.4[h,j]**	**71.4**	**AIST(8/10)**	**Sony, 8 parallel cells**
Organic							
Organic polymer	**8.3±0.3[m]**	**1.031(ap)**	**0.816**	**14.46**	**70.2**	**NREL(11/10)**	**Konarka**
Organic (submodule)	3.5±0.3[m]	208.4(ap)	8.62	0.847	48.3	NREL (7/09)	Solarmer

Multijunction devices							
GaInP/GaAs/Ge	32.0±1.5[I]	3.989(t)	2.622	14.37	85	NREL (1/03)	Spectrolab (monolithic)
GaAs/CIS (thin film)	25.8±1.3[I]	4.00(t)	-	-	-	NREL (11/89)	Kopin/Boeing (4 terminal) [30]
a-Si/μc-Si (thin film cell)	**11.9±0.8[n]**	**1.227**	**1.346**	**12.92[I]**	**68.5**	**NREL (8/10)**	**Oerlikon Solar Lab, Neuchatel [8]**
a-Si/μc-Si (thin film submodule)[j,I]	11.7±0.4[I,O]	14.23(ap)	5.462	2.99	71.3	AIST (9/04)	Kaneka (thin film)[31]
Organic (2-cell tandem)	**8.3±0.3[m]**	**1.087(ap)**	**1.733**	**8.03[I]**	**59.5**	**FhG-ISE (10/10)**	**Heliatek [9]**

[a] CICS= CnlnGaSe2; a-Si=amorphous silicon/hydrogen alloy.

[b] Effic.= efficiency

[c] (ap)= aperture area; (t)= total area; (da)=designated illumination area.

[d] FF= fill factor.

[e] FhG-ISE= Fraunhofer Institute fur Solar Energies system; JQA=Japan Quality Assurance; AIST=Japanese National Institute of Advanced Industrial Science and Technology.

[f] Spectral response reported in Version 36 of these tables.

[g] Recalibrated from original measurement.

[h] Recalibrated from original measurement.

[i] Not measured at an external laboratory.

[j] Spectral response reported in present version of these tables.

[k] Light soaked at Oerlikon prior to resting at NREL (1000h, 1 sun, 50°C).

[l] Measured under IEC 60904-3 Ed. 1:1989 reference spectrum.

[m] Stability not investigated.

[n] Stabilized by 1000h, 1 sun illumination at a sample temperature of 50°C.

[o] Stabilized by 174h, 1 sun illumination after 20h, 5 sun illumination at a sample temperature of 50°C.

Table (2.2). Confirmed terrestrial module efficiencies measured under the global AM1.5 spectrum (1000W/m2) at a cell temperature of 25°C (IEC 60904-3: 2008, ASTM G-173-03 global).

Classification	**Effic.[b] (%)**	**Area[c] (cm^2)**	**V_{oc} (cm^2)**	**J_{sc} (mA/cm^2)**	**FF[d] (%)**	**Test centre (and Data)**	**Description**
Si(crystalline)	22.9±0.6	778(da)	5.6	3.97	80.3	Sandia (9/96)[e]	UNSW/Gochermann
Si (Large crystalline)	21.4±0.6	15780(ap)	68.6	6.293	78.4	NREL (10/09)	Sun Power
Si (multicrystalline)	**17.55±0.5**	**14701(ap)**	**38.31**	**8.94[f]**	**75.3**	**ESTI (8/10)**	**Schott Solar (60 serial cells)**
Si(tin-film polycrystalline)	8.2±0.2	661(ap)	25	0.32	68	Sandia (7/02)[e]	Pacific Solar (1-2μm on glass)[36]
CIGS	**15.7±0.5**	**9703(ap)**	**28.24**	**7.254[f]**	**72.5**	**NREL (11/10)**	**Miasole**
CIGSS (Cd free)	13.5±0.7	3459(ap)	31.2	2.18	68.9	NREL (8/02)[e]	Showa Shell
CdTe	10.9±0.5	4874(ap)	26.21	3.24	62.3	NREL	BP Solarex

						(4/00)[e]	
a-Si/a-SiGe/a-SiGe (randem	10.4±0.5[g.h]	905(ap)	4.353	3.285	66	NREL (10/98)[e]	USSC

[a] CICS= CnlnGaSSe; a-Si=amorphous silicon/hydrogen alloy; a-SiGe= amorphous silicon/germanium/hydrogen alloy.

[b] Effic.= efficiency

[c] (ap)= aperture area; (da)=designated illumination area.

[d] FF= fill factor.

[e] Recalibrated from original measurement.

[f] Spectral response reported in present version of these tables.

[g] Lightsoaked at NREL for 1000h at 50°C, nominally 1-sun illumination.

[h] Measured under IEC 60904-3 Ed. 1: 1989 reference spectrum.

Table (2.3). Notable Exceptions: Top ten confirmed cell and module results, not class records measured under the global AM1.5 spectrum (1000 Wm^{-2}) at 25°C (IEC 60904-3: 2008, ASTM G-173-03 global).

Classification	Effic.[b] (%)	Area[c] (cm^2)	V_{oc} (cm^2)	J_{sc} (mA/cm^2)	FF[d] (%)	Test centre (and Data)	Description
Cells (Silicon)							
Si (MCZ crystalline)	24.7±0.5	4.0(da)	0.704	42	83.5	Sandia (7/99)[d]	UNSW PERL, SHE MCZ substrate
Si (large crystalline)	**24.2±0.7**	**155.1(t)**	**0.721**	**40.5[e]**	**82.9**	**NREL (5/10)**	**Sun power n-type CZ substrate**
Si (large crystalline)	23.0±0.6	100.4(t)	0.729	39.6	80	AIST (2/09)	Sanyo HIT, n-type substrate
Si (large multicrystalline)	19.3±0.5	217.7(t)	0.651	38.8[f]	76.4	AIST (7/09)	Mitsubishi Electric honeycomb
Cells (Other)							
GalnP/GaAs/GalnAs (tandem)	35.8±1.5	0.880(ap)	3.012	13.9	85.3	AIST (9/09)	Sharp, monolithic
CIGS (thin film)	**20.3±0.6**	**0.5015(ap)**	**0.740**	**35.4[e]**	**77.5**	**FhG-ISE (6/10)**	**ZSW Stuttgart CIGS on glass [**

a-Si/nc-Si/nc-Si (tandem)	12.5±0.7[g]	0.27(da)	2.01	9.11	68.4	NREL (3/09)	United Solar stabilized
Dye-sensitized	11.2±0.3[h]	0.219(ap)	0.736	21	72.2	AIST (3/06)[d]	Sharp
Luminescent submodule	**7.1±0.2[h]**	**25(ap)**	**1.008**	**8.84**	**79.5**	**ESTI (9/08)**	**ECN Petten, GaAs cells**

[a] CICS= CnlnGaSSe$_2$;

[b] Effic.= efficiency

[c] (ap)= aperture area; (da)=designated illumination area.

[d] Recalibrated from original measurement.

[e] Spectral response reported in present version of these tables.

[f] Spectral response reported in version 36 of these tables.

[g] Light soaked under 100mW/cm^2 white light at 50°C for 1000h.

[h] Stability not investigated.

Table (2.4).Terrestrial concentrator cell and module efficiencies measured under the ASTM G-173-03 direct beam AM1.5 spectrum at a cell temperature of 25°C

Classification	Effic.[a] (%)	Area[b] (cm^2)	Intensty[c] (suns)	Test centre (and Data)	Description
Single cells					
GaAs	29.1±1.3[d,e]	0.0505 (da)	117	FhG-ISE(1/10)	Fraunhhofer ISE
Si	27.6±1.0[f]	1.00(da)	92	FhG-ISE(11/04)	Amonix Back-contact
Multifunction cells					
InGaP/GaAs/InGaAs (2-terminal)	**42.3±2.5[i]**	**0.9756(ap)**	**406**	**NREL(9/10)**	**Spire, bi-facial epigrowth**
GalnP/GalnAs/Ge (2-terminal)	41.6±2.5[e]	0.3174(da)	364	NREL(8/09)	Spectrolab, lattice-matched
Submodules					
GalnP/GaAs; GalnAsP/GalnAs	**38.5±1.9[i]**	**0.202(ap)**	**20**	**NREL(8/08)**	**DuPone et al., split spectrum [16]**
GalnP/GaAs/Ge	27.0±1.5[g]	34(ap)	10	NREL(5/00)	ENTECH [48]
Modules					

Si	20.5±0.8[d]	1875(ap)	79	Sandia (4/89)[h]	Sandia/UNSW/ ENTECH (12 cells) [49]
Notable exceptions					
GalnP/GaAs (2-terminal)	32.6±2.0[e]	0.010(da)	1026	FhG-ISE(9/08)	U. Polytecnica de Madrid [50]
Si (large area)	21.7±0.7	20.0(da)	11	Sandia(9/90)[h]	UNSW laser grooved [51]

[a] Effic.=efficiency.

[b] (ap)= aperture area; (da)=designated illumination area.

[c] One sun corresponds to direct irradiance of 1000W/m.

[d] Not measured at an external laboratory.

[e] Spectral response reported in version 36 of these tables.

[f] Measured under a low aerosol optical depth spectrum similar to ASTM G-173-03 direct.

[g] Measured under old ASTM E891-87 reference spectrum.

[h] Recalibrated from original measurement.

[i] Spectral response reported in the present version of these tables.

Voted for their preferences for inclusion. Readers who have suggestions of results for inclusion into this table are welcome to contact any of the authors with full details.

Suggestions conforming to the guidelines will be included on the voting list for a future issue.

Table (2.4) shows the best results for concentrator cells and concentrator modules (a smaller number of “notable exceptions” for concentrator cells and modules additionally is included in table 2.4).

Fourteen new results are reported in the present version of these Tables.

The first new result in Table I an outright record for solar conversion by any single-junction photovoltaic device. An efficiency of 27.6% has been measured at the National Renewable Energy Laboratory (NREL) for s 1 cm^2 thin-film GaAs device fabricated, by Alta Devices, Inc. Alto Devices is a Santa Clara based ‘start-up” seeking to develop low-cost, 30% efficient solar modules.

The second new result in Table I is an efficiency improvement to 19.6% for a I cm2 single-junction copper—indium—gallium—selenide (CIGS) cell fabricated by and measured at NREL. Although CIGS efficiency of 20% and (higher has been reported previously by two groups (see Table III), this has been for cells appreciably less than t cm^2 in area, the minimum considered reasonable for efficiency comparisons in these Tables and for milestones in most of the international programs.

A third new result in Table (2.1) is 12.5% efficiency for an eight cell 35cm^2 CdTe submodule fabricated by Advanced Solar Power (ASP) Hangzhou, also measured by NREL.

A fourth new result in Table (2.1) is for a dye sensitized submodule with efficiency of 9.9%.Reported for a 17 cm^2 submodule fabricated by Sony and measured by the Japanese National Institute of Advanced Industrial Science and Technology (AIST). This is quite close to the record of 10.4% efficiency for the best individual dye sensitized cell yet confirmed (of more than 1 cm^2 area).

Another outstanding new result is the measurement of 8.3% efficiency at NREL for a 1cm2 organic cell fabricated by Konarka, representing a massive improvement over the company's previous 5.15% record entry. An inter mediate result of 6.5% was measured in July 2010. Another new result in Table (2.1) is for a double-junction Amorphous /microcrystal line silicon cell with stabilized efficiency of 11.9% reported for a 1.2 cm^2 cell fabricated by Oerlikon and Corning N and again measured by NREL. After stabilization.

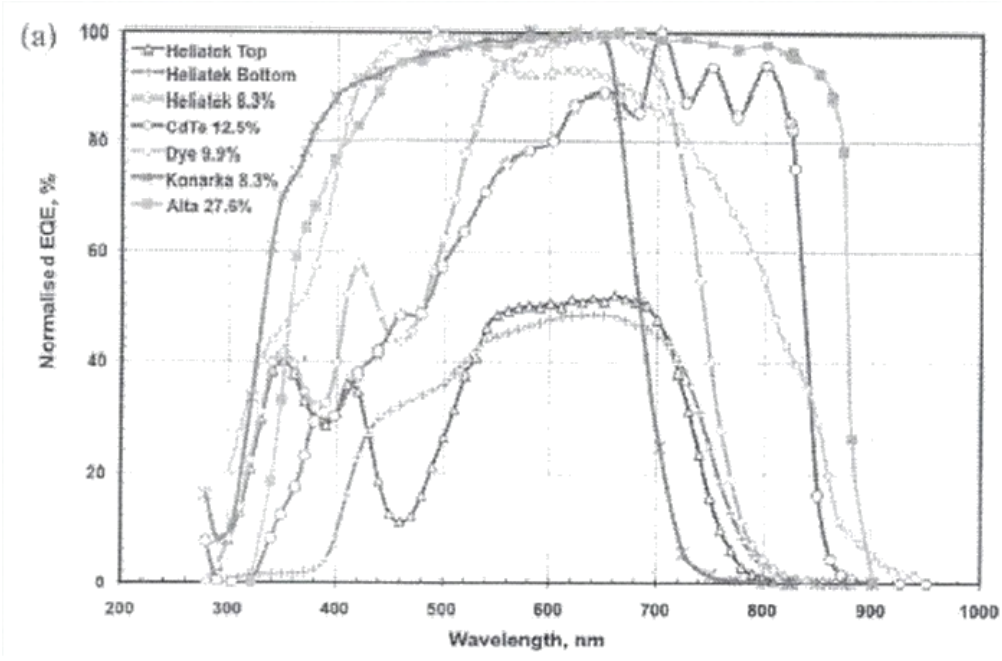

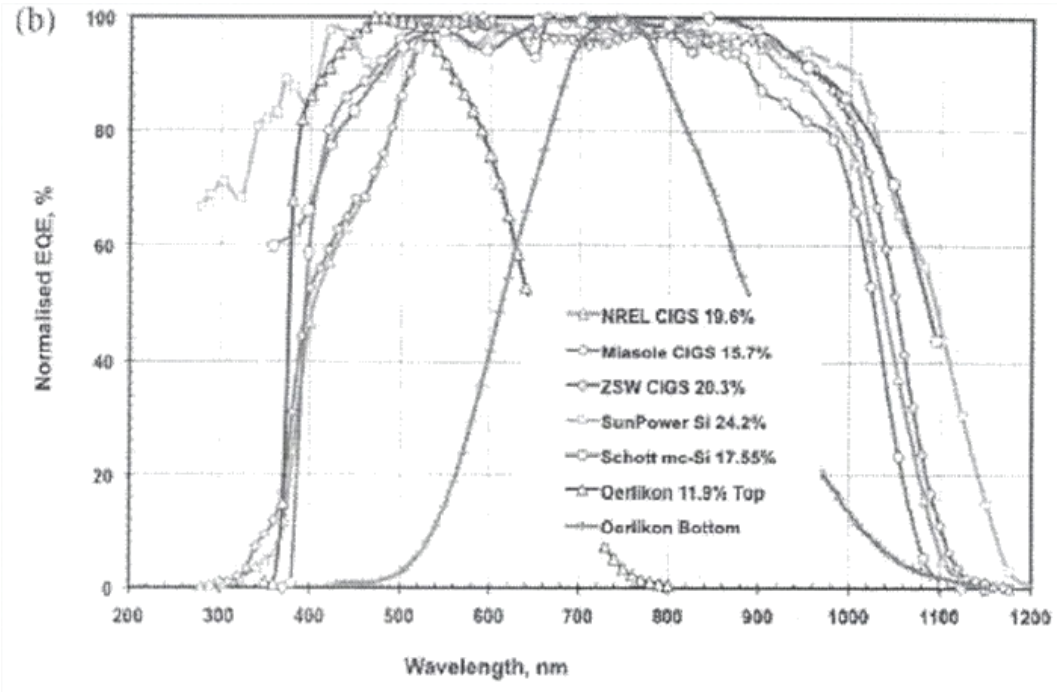

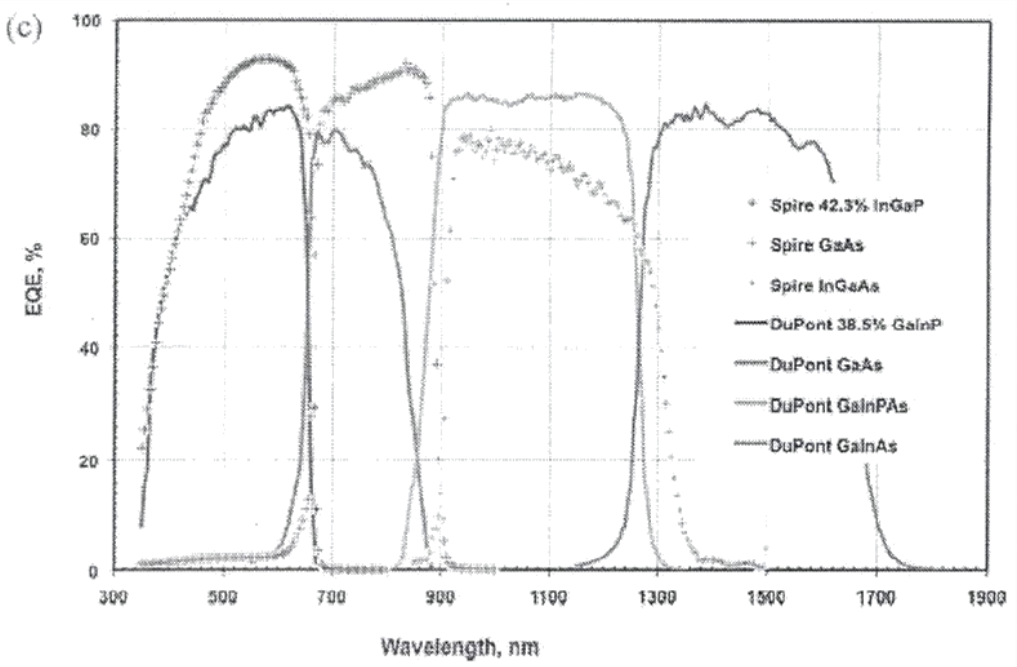

Figure(2.19). (a) Normalized external quantum efficiency (EQE) for the new organic and GaAs cell results in this issue and for the new CdTe and dye-sensitized submodule results; (b) Normalized EQE for the three new CIGS cell and module entries in this issue plus for the three new silicon cell and module results; (c) EQE of the composite cells for the new concentrator cell and submodule entries in the present issue.

The final new result in Table (2.1) is for a double-junction organic solar cell with 8.3% efficiency measured for a I .1 cm^2 cell fabricated by Heliatek and measured by the Fraunhofer Institute for Solar Energy Systems (FhG-ISE). This represents rapid progress from the 6.1% result from Heliatek measured in June last year and reported in the previous version of these Tables. An intermediate result of 7.7% was measured in March 2010.

Following e similarly vigorous burst of activity in the multicrystalline silicon module area reported in the two previous versions of these Tables, where four groups exceeded the previous record for module efficiency over the two reporting periods, a fifth group has done even helter. In Table (2.2), a new efficiency record of 17.55% is reported for a large (1.5 m^2 aperture area) module fabricated by Schott Solar and measured by the European Solar ‘Pest Installation, Ispra (ESTI)). Also reported in Table (2.2) is a record result for a thin-film module, with a large improvement to 15.7% reported for a I m^2 CIGS module fabricated by Miasole and measured by NREL.

The first new result in Table (2.3) relates to an efficiency increase to 24.2% for a large 155 m^2 silicon cell fabricated on an n-type Czochralski grown wafer, with the cell fabricated by Sun Power and also measured by NREL.

Another new result in Table (2.3) is the further improvement of a small area (0.5 cm^2) CIGS cell fabricated by Zentrum fur Sonnenenergie- und Wasserstoff- For schung (ZSW), Stuttgart to 20.3% efficiency as measured by FhG-ISE. This cell is smaller than the 1 m^2 size required for classification as an outright record, as previously discussed.

The final new result in Table (2.3) is for a luminescent concentrating submodule using high performance GaAs cells placed along the edge of a luminescent plate to convert the collected luminescent radiation. An efficiency of 7.1% was confirmed for a 25cm^2 test device fabricated by ECN, Netherlands and measured by ESTI.

Two more new results are reported in Table (2.4) for more conventional concentrator cells and systems. The tirst is a new efficiency record for any photovoltaic cell with 42.3% efficiency measured by NREL at 406 suns concentration (irradiance) fur an I cm^2 cell fabricated by the Spire Corporation. A new approach was used whereby a low band gap In GaAs cell was grown on one side of a GaAs wafer, with the wafer then flipped over and an intermediate band gap GaAs followed by a high band gap In GaP cell grown on the other side.

The final new result represents a new record for the conversion of sunlight to electricity by any means. An efficiency vi' 38.5% was measured by NREL for a very small area (0.2 cnt2) spectral-splitting submodule at about 20 suns concentration as the result of a multi-institutional effort headed by DuPont. This complete lens/cell assembly uses a dichroic reflector to steer light to two different two-cell stacks, one on a GaAs substrate and one on an lnP substrate.

The external quantum efficiencies (EQE) normalized to the peak EQF values for the new organic cell results of Table Tare shown in Figure (1a) as well as the response for the GaAs cell and CdTe and dye-sensitized submodules of Table (2.1). Also shown is the decomposition into the top and bottom cell response for the 8.3% 1-leliatek tandem cell of Table (2.1). Interestingly, both cells in the stack have largely overlapping spectral response range, although complement in some aspects.

Figure (2.19b) shows the normalized EQE of the new ClGS
and silicon results in the present issue of these tables, Quite striking is the almost identical responses of the NREL and ZSW CIGS cells with the higher current from the ZSW cell attributed to a slightly lower band gap edge. The normal ized responses of both cells in the Oerliken/Corning micro morph tandem cell are also shown.

Figure 2.19(c) shows the absolute EQE for the different cells
contributing to the new concentrator cell and submodule

results of Table IV. The much narrower response bandwidth of the bottom InGaAs cell in the 42.3% Spire monolithic stack compared to the response of the bottom Ge in the 41.6% Spectrolab device [3] reflects a higher band gap.

This gives a higher voltage output that contributes to the improved performance. The EQE for the 38.5% submodule differs slightly from results reported elsewhere due to incorporation of the effect of the dichroic reflector used in this system. Each of the four cells in this system is contacted separately, removing the need for current matching [36].

Multifunction III-V concentrator cells have the highest energy conversion deficiency of any solar cell technology, with several different types of cell architecture reaching over 40% efficiency since 2006. Such cells represent the only third – generation photovoltaic technology to enter commercial power generation markets far, and continue to demonstrate what is possible for other emerging solar cell technologies that divided the sun's spectrum into discrete slices for higher efficiency, such as flat – plate multifunction polycrystalline semiconductor cells, tandem organic solar cells, and spectral splitting optical systems[51].

Chapter Three

Literature Review

3. Introduction

In this chapter some attempts to fabricate ZnO and CuO solar cells and their performance are investigated. The purpose of the present works to fabricate Cu_2O/ZnO and ZnO/Cu_2O thin film solar cells by electrodepositing, and to investigate the effect of Cu_2O and ZnO layers on their electronic properties. Structural, morphological and absorption measurement of CuO/ZnO heterojunction were studied by using x-ray diffraction, transmission electron microscopy, atomic force microscopy and also the determination the energy levels. In the other hand CuO and ZnO films were deposited using a galvanostatic method, hetrojunction were studied by using also (XRD), and light current- voltage characteristics.

The n-type ZnO/ p-type CuO heterojunction have been fabricated by sol-gel dip-coating technique which is simple and inexpensive.

3.1 Fabrication and characterization of copper oxide –zinc oxide solar cells prepared by electrodeposition

In this paper the Cu_2O and CuO layers were prepared on pre-cleaned indium tin oxide (ITO) glass plate by electro deposition using platinum counter electrode, Copper (11) sulfate ($CuSO_4$, 0.4 mol L^{-1} ,Wako 97.5%) and L-lactic acid (3 mol L^{-1} ,Wako) were dissolved into distilled water. Electrolyte pH was adjusted to 12.5 by adding NaOH. The electrolyte temperature was kept at 65 ^{0}C during electrodepositing. Preparation of Cu_2O layers were carried out at current density at 1.5 mA cm^{-2} and quantity of electric charge of 4.0 C cm^{-2}. ZnO layers were also

galvanostatically pared at current density at 5 and 10 $mAcm^{-2}$ from 8mM aqueous solution of Zn $(NO_3)_2$ on Cu_2O layers. Electric charge was adjusted 1.5 C cm^{-2} .Gold (Au) metal contacts were vacuum deposited as top electrodes. Structures were denoted as ITO or FTO/ZnO/Cu_2O or Cu_2O/Au. Current density-voltage (J-V) characteristics (Hokuto Denko, HSV-110)

Of the solar cells were measured both in the dark and under illumination at 100mW cm^{-2} by using an AM1.5 solar simulator (San-ei Electric, XES-301S). The solar cells were illuminated through the side of the ITO substrates, and the illuminated area was 0.16 cm^2.Optical absorption of the solar cells was investigated by means of UV visible spectroscopy (Jasco, V-670). The incident photon to current conversion efficiency (IPCE) of solar cells of investigated (Peccell technologies, PEC-S20). The microstructures of the copper oxide were investigated by X-ray diffract meter (XRD, Philips, X□ Pert-MPD System) with CuKα radiation operating at40KVand 40 mA, and scanning electron microscope (SEM) operating at 15KV (Jeol, JEM-6380).

3.1.1 Results and Discussion

J-V characteristics of ZnO/Cu_2O structure under illumination at 100mW cm^{-2} by using an AM 1.5 solar simulator. The photocurrent was observed under illumination and the CuO/ZnO structure shoed characteristic curves with short-circuits current and open-circuit voltage. A solar cell with FTO/ZnO/Cu_2O structure provided power conversion efficiency (η) of 0.25%, fill factor (FF) of 0.33, and short-circuit current density (J_{sc}) of 2.7 mA cm^{-2} and open-circuit voltage (V_{oc}) of 0.28V. Solar cells with ITO/ZnO (mA cm^{-2}) /Cu_2O structure provided power conversion efficiency (η) 7.3×10^{-3}%, fill factor (FF) 0.26, and short-circuit current density (J_{sc}) of 0.45$mAcm^{-2}$and open-circuit voltage (0.063) V. Solar cell with

ITO/ZnO(5mAcm^{-2}) /Cu_2O also provided power conversion efficiency (η) 6.9×10^{-2} %, fill factor (FF) 0.26, and (J_{sc}) 1.38mAcm^{-2}, and (V_{oc}) 0.20V. Solar cell with ITO/ZnO (5mAcm^{-2}) also provided power conversion efficiency (η) 1.0×10^{-5}%,fill factor (FF) of 0.25, and (J_{sc}) of 2.4×10^{-3} mAcm^{-2}, and open-circuit voltage (V_{oc}) 0.017 [5].

3.1.2 Fabrication and Evaluation of CuO/ZnO Heterostructures for Photoelectric Conversion

Solar cell with cuprous oxide (CuO) and zinc oxide (ZnO) heterojuntion fabricated on indium tin oxide –glass were studied. CuO and ZnO films were deposited using a galvanostatic method. Structural, morphological and optoelectronic properties of the CuO/ZnO heterojuntion were studied by using X-ray diffraction, atomic force microscopy and light current-voltage characteristics.

Silicon is used as the semiconductor material for conventional solar cells, but silicon is expensive and cost reduction of the solar cells is one of the most important issues. Oxide semiconductors are one of the alternatives to silicon solar cells, and copper oxide such as CuO and Cu_2O are one of the candidate materials. The features of copper oxide semiconductors are relatively higher optical absorption, low cost of raw materials and non-toxic. CuO and Cu_2O are p-type semiconductors with band gap energies of 1.5 eV and 2.0 eV, respectively, which are close to the ideal energy gap of 1.4 eV for solar cells and allows for good solar spectral absorption. Zinc oxide (ZnO) is an n-type semiconductor with a wide band gap of ~3.37 eV, which can be applied to solar cells .The highest efficiency of ~2% for Cu_2O solar cells has been obtained by using the high temperature annealing method.

3.1.3 Experimental Procedures

The purpose of the present work is to fabricate and characterize solar cells with CuO/ZnO structures. CuO layer were prepared on pre-cleaned indium tin oxide (ITO) glass plate by electro deposition using platinum as counter electrode. Copper (11) sulfate ($CuSO_4$, 0.4 mol/L, Wako97.5%) and l-lactic acid (3 mol/L, wako) were dissolved into distilled water. PH of the electrolyte solution was adjusted to 12.5 by adding NaHO. The temperature of electrolyte solution was kept at 65^0C during electro deposition. Preparation of CuO layers were carried out at voltage of +0.70Vand quantity of electric charge of 2.2C cm^{-2}. After the deposition, the sample was rinsed with water and transferred in to the ZnO electro deposition bath. ZnO layers were galvanostatically electro-deposited from 0.025 M aqueous solution of Zn (NO_3) on the ITO/CuO substrate. The sample thickness ranged between 1and 2µm depending on the deposition time and current. Finally, the substrates were rinsed with water, dried with air and quickly transferred into a thermal evaporator for the vacuum deposition of the aluminum (Al) back contact, Structure of heterojunction solar cells were denoted as ITO/CuO/ZnO/Al,

Current density- voltage (J-V) characteristics (Hokuto Denko Corp., HSV-100) of the solar cells were measured using potentiostat (Hokuto Denko,HSV-100) in the dark and under illumination at 100 mW/cm^2 by using an AM 1.5 solar simulator(San-ei Electric, XES-301S). The solar cells were illuminated through the side of the ITO substrate, and the illuminated area was 0.16 cm^2. Optical absorption of the solar cells was investigated by means of UV visible spectroscopy (Hitachi, Ltd., U-4100). Microstructures of the copper oxide were investigated by X-ray diffractometer (XRD, PHILIPS X Pert-MPD System) with CuKα radiation operating at 40 KV and

40mA. Transmission electron microscopy (TEM, Hitachi H-8100, 200 kV operating voltage) was also carried out for nanostructure analysis.

3.1.4 Results and Discussion

Thicknesses of CuO were ~1μm and ~2μm for 5 min and 10min, respectively. A solar cell with a CuO/ZnO structure provided power conversion efficiency (η) of 1.1×10^{-4} %, fill factor (FF) of 0.25, and short-circuit current density (J_{sc}) of 1.9mAcm^{-2} and open-circuit voltage (V_{oc}) of 2.8×10^{-4}. Thicknesses of CuO ~2μ m for 10min, solar cell structure provided power conversion efficiency (η) $1.1x10^{-7}$, fill factor (FF) 0.25, and short-circuit current (J_{sc}) 0.017 mA/cm^{-2} and open – circuit voltage (V_{oc}) of 1.8×10^{-4} V. The ZnO/CuO (5 min) structure provided power conversion efficiency 9.9×10^{-5} , fill factor (FF) of 0.28, and short-circuit current density (J_{sc}) 0.43, and open-circuit voltage (V_{oc}) 8.2×10^{-4}V. The photocurrent was observed under illumination and CuO/ZnO structure showed characteristic curves with short-circuits current and open-circuit voltage. The CuO and ZnO thin films show high optical absorption in the range of 400nm and 700nm.

Transmittance spectrum of 100nm thick CuO film, deposited on ITO, the optical absorption coefficients (α) of this film was determined from the spectral transmittance using the next equation $\alpha = \frac{1}{d} .\ln(\frac{1}{T})$. Where d is the film thickness and T is the transmittance. For determination of the optical band gap energy (E_g), the method based on the relation of $\alpha h\upsilon = A\ (h\upsilon - E_g)^{n/2}$ was used, where n is a number that depends on the nature of the transition. In this case, its value was found to be 1, which corresponds to direct band to band transition.

In this research we use a tauc plot, which shows $(\alpha h\upsilon)^2$ versus hυ for the CuO film. The intersection of the straight line with hυ-exis determines the optical band gap energy E_g. It was found to be ~ 2.1eV which is lower than the ideal band gap of the CuO crystal. Because of the small band gap energy, the open-circuit voltage would be low [6].

3.2 Current-Voltage Characteristics of P-CuO/n-ZnO：Sn Solar Cell

In this study p-CuO/n-ZnO:Sn heterojunction solar cell has been fabricated on glass substrate in steps using Edwards AUTO 306vacuum coater system. Copper oxide has energy band gap of the range 1.21-2.1eV while tin doped zinc oxide (TZO) has good transmittance properties. A solar cell with thickness of 250nm of p-type copper oxide and thickness of 140nm of n-type TZO with 2% tin doping has been made. Current-Voltage (I-V) measurement has been done on the solar cell using Keithley 2400sourcemeter interfaced with the computer running labview program. Diode properties determined from I-V measurements are open circuit voltage (V_{oc}), short circuit current (I_{sc}), fill factor (FF), maximum current output (I_m), and maximum voltage output (V_m), and conversion efficiency (η). The solar cell had V_{oc} of 480 mV, I_{sc} of 326.8mA, FF=0.63 and η=0.232%.

3.2.1 Experimental Procedure

The process of fabrication the solar cell was done in stages using Edwards AUTO 306 vacuum coater system. Silver paste acting as the back contact electrode was applies on a clean glass substrate measuring 70mm×27mm. The glass slide was wrapped with strips of aluminum foil 20mm from both ends so as to mask the edges and parts of silver layer film deposition. The glass slide was mounted on revolving substrate holder of the vacuum coater.

Then 250nm thick CuO was deposited on the glass slide at room temperature by reactive dc magnetron sputtering method at oxygen flow of 5sccm. Argon was used as the sputtering gas and oxygen as the reacting gas. CuO film was deposited at chamber pressure of 9×10^{-3} mbars, argon flow of 20sccm and power of 200W.

Then a 140 nm thick TZO was deposited on CuO layer by reactive evaporation technique at temperature of 750^{0}C, oxygen flow of 20sccm and base pressure of 3×10^{-5}mbars. Current supplied to the molybdenum boat was 3.5A.The film deposited was doped at 2% tin concentration. Temperature was monitored using digital thermometer attached to the backside of molybdenum boat. A P-N junction of CuO-ZnO:Sn was denoted as Glass Substrate/Ag back contact/CuO/ZnO:Sn Solar Cell.

3.2.2 The Result and Discussion

The Diode characteristics investigated for the fabricated solar cell are open –circuit voltage (V_{oc}), short-circuit current (I_{sc}), fill factor (FF), maximum-current output (I_m), maximum-voltage output (V_m), and conversion (η). Fill factor and conversion efficiency are obtained using the diode parameters as shown in equations 1and 2 below.

$$FF = \frac{I_m V_m}{I_{sc} V_{oc}} \qquad (3-1)$$

$$\eta = \frac{I_m V_m}{P_{in}} \times 100 \qquad (3-2)$$

Where V_{oc} is open-circuit voltage, I_{sc} short circuit-current, FF is fill factor, I_m maximum current output, V_m maximum voltage output, η conversion efficiency and P_{in} is power of photons incident on solar cell.

Diode properties of the solar cells were determined from measurements of current and voltage generated across the solar cell using four point probe system by use of Keithley 2400sourcemeter interfaced with a computer running labview program. The measurement was done with 100W bulb radiating light at power of 640W/m^2 and temperature of 25^0C. The power of light from the bulb was measured by a pyranometer. The bulb-solar cell separation distance was 15cm.The lab view program was such that a voltage of 0.8Vwas sourced from Keithley source meter to the solar cell and then current across it measured. The appropriate formulas were fitted into the program enabling it to automatically plot current versus voltage graph and determine V_{oc} ,I_{sc} ,I_m ,V_m and η for the solar cell.

3.2.3 Conclusion

A solar cell with silver back contact, n-type TZO window layer and p-type CuO absorber layer was fabricated in stages using Edwards AUTO306 vacuum coater system. I-V characteristics were measured using Keithley 2400sourcemeter interfaced with computer running lab view program. The solar cell had V_{oc} of 480mV, I_{sc} of 0.182mA, FF of 0.63 and efficiency of 0.232%.

The values of V_{oc} and fill factor obtained are higher than those of other solar cells like $CuSe_2$, CIGS and SIGS/ZnO whose values of V_{oc} and fill factor are 450mV and 0.62 respectively but with higher efficiency of 11%. The low efficiency may be attributed to surface reflections of incident photons leaving less radiation for conversion to electricity. Heating also decreases efficiency because at higher temperatures, conductivity decreases. More so series resistance of the cell due to non-ohmic contacts inhibits the flow of electrons. This decreases V_{oc} and makes current of the I-V curve fall slowly. Even though the efficiency of

the solar cell fabricated was low, the availability and low cost of the materials makes it relatively affordable as compared to other cell devices like CIGS based cells whose materials are very expensive and not easily available [7].

3.3 Fabrication and Characterization of CuO/ZnO Solar Cells

In this study cuprous oxide (CuO) and zinc oxide (ZnO) heterojunction solar cells fabricated on indium tin oxide –coated glass were studied. CuO and ZnO films were deposited using a galvanostatic method. The purpose of the present work is to fabricate and characterize solar cells with CuO/ZnO structures. The band gab energy of CuO is ~1.5eV, which is closer to the ideal band gap of 1.4eV. Zinc oxide (ZnO) is an n-type semiconductor with a wide band gap of ~3.37eV, which can be applied to solar cells. Structural, morphological and optoelectronic properties of the CuO/ZnO heterojunction were studied by using X-ray diffraction, atomic force microscopy and light current-voltage characteristics.

3. 3.1Experimental Procedures

CuO layers were prepared on per-cleaned indium tin oxide (ITO) glass plate by electro deposition using platinum as counter electrode. Copper (II) sulfate ($CuSO_4$, 0.4 mol /L, Wako 97.5%) and 1-lactic acid (3mol/, Wako) were dissolved into distilled water. pH of the electrolyte solution was adjusted to 12.5 by adding NaOH. The temperature of electrolyte solution was kept at 65^0C during electro deposition. Preparation of CuO layers were carried out at voltages of +0.70V and quantity of electric charge of 2.2C cm^{-2}. After the deposition, the sample was rinsed with water and transferred into the ZnO electro deposition bath. ZnO layers were galvanostatically electro-deposited from 0.025 M aqueous solution of Zn (NO_3) on the ITO/CuO substrate. The

sample thickness ranged between 1and 2 µm depending on the deposition time and current. Finally, the substrates were rinsed with water, dried with air and quickly transferred into a thermal evaporator for the vacuum deposition of the aluminum (Al) back contact. Structure of heterojunction solar cells were denoted as ITO/CuO/ZnO/Al,

Current density- voltage (J-V) characteristics (Hokuto Denko Corp, HSV-100) of the solar cells were measured both in the dark and under illumination at 100 mW/cm^2 by using an AM 1.5 solar simulator (San-ei Electric, XES-301S). The solar cells were illuminated through the side of the ITO substrate, and illuminated area was $0.16cm^2$. Optical absorption of the solar cells was investigated by means of U V visible spectroscopy (Hitachi, Ltd; U-4100). Microstructures of the copper oxides were investigated by X-Ray diffractometer (XRD, PHILIPS X' P X' Pert-MPD System) with CuKα radiation operating at 40KV and 40mA.

3.3.2 Results and Discussion

Thicknesses of CuO were ~1µm and~2µm for 5min and10 min, respectively. A solar cell with a CuO/ZnO structure provided power conversion efficiency (η) of 1.1×10^{-4}%, fill factor (FF) of 0.25, short-circuit current density (J_{sc}) of 1.6 $mAcm^{-2}$ and open-circuit voltage (V_{oc}) of 2.8×10^{-4}V. The photocurrent was observed under illumination, and the CuO/ZnO structures showed characteristic curves with short-circuit current and open-circuit voltage. The CuO and ZnO thin films show high optical absorption in the range of 400nm and 800nm. Also Thicknesses of ~2µm for 10 min (η) 1.1×10^{-7}%, fill factor (FF) 0.25, short-circuit current density (J_{sc}) $0.017mAcm^2$, and open-circuit voltage (V_{oc}) of 0.18mV.Transmittance spectrum of 100nm of thick CuO film, deposited on ITO, is presented from this spectrum, the

optical absorption coefficients (α) of this film was determined from the spectral transmittance using the next equation α=1/d.ln (1/T). Where d is the film thickness and T is transmittance. For determination of the optical band gap energy (E_g), the method based on the relation of $\alpha h\upsilon=A\ (h\nu = E_g)^{n/2}$ was used, where n is a number that depends on the nature of the transition. In this case, its value was found to be 1, which corresponds to direct band to band transition.

Use a Tauc plot, which shows $(\alpha h\nu)^2$ versus hνfor the CuO film. The intersection of the straight line with the $h\nu$-axis determines the optical band gap energy E_g. It was found to be ~2.1eV which is lower than the ideal band gap of the CuO crystal. Because of the small band gap energy, the open-circuit voltage would be low. Diffraction peaks corresponding to CuO and ZnO are observed in thin film, which consisted of cupric phase with monoclinic system (space group of C2/c and lattice parameter of a=0.4653 nm, b=0.3410 nm, c=0.5018 nm, $\beta=99.481^0$). The particle size was estimated using Scherer's equation; $D=0.9\lambda/B\cos\theta$, where λ, B, and θ represent the

Wavelength of the X-ray source, the full width at half maximum (FWHM), and the Bragg angle, respectively. The crystallite size of CuO and ZnO were determined to be 49.0nm and 82.0nm, respectively. Lattice constant of CuO and ZnO were obtains and comparing with reported value. From the lattice constant, the crystal structures of CuO and ZnO have some crystal distortions. To increase the efficiency of the CuO/ZnO solar cells, small grain size of ZnO and higher crystalline of CuO would be necessary [8].

Energy level diagram of the CuO/ZnO solar cell was showed. Previously reported values were used for the energy

levels. It has been reported that V_{oc} is nearly proportional to the band gap of the semiconductors, and control of the energy level is important to increase efficiency. Compared to silicon with an indirect transition band structure, CuO with a direct transition band structure is more suitable for the optical absorption property. In addition, the ultrathin film of the CuO layers could provide efficient charge injection because of the optical absorption. In the present work, microstructures of CuO and ZnO thin film were found to have some crystal distortion, which would result in the reduction of electrical transport. If the crystal qualities of the CuO and ZnO thin films are increased, V_{oc} would be improved.

3.3.3 Conclusion

ITO/CuO/ZnO/Al solar cells were produced and characterized which provided ηof 1.1×10^{-4}%, FF of 0.25, J_{sc} of 1.6 $mAcm^{-2}$ and V_{oc} of 2.8×10^{-4} V. The CuO/ZnO structure showed high optical absorption in the range of 400 nm and 800 nm, and the E_g of CuO was found to be ~1.2 eV from the Tauc plot which is smaller than that of the ideal band gap of the CuO crystal and the open-circuit voltage would be decreased. A crystallite size of CuO was determined to be 49.0 nm, and higher crystalline of CuO would increase the efficiency of the CuO/ZnO solar cells. The energy level of the present solar cell was proposed, and separated holes could transfer from the valence band of the CuO to the ITO, and separated electrons could transfer from the conduction band of the CuO to the Al electrode, respectively. Formation of the CuO/ZnO active layer with homogeneous distributed CuO nanoparticles would improve the efficiencies of the solar cells.

3.4 Current Transport Mechanisms of n-ZnO/p-CuO Heterojunctions

In this study n – ZnO/p –CuO heterojunction have been fabricated by sol – gel dip – coating technique which is simple and inexpensive. The structure of the p-CuO/n –ZnO was analyzed by x-ray diffraction spectroscopy and UV-VIS spectroscopy. The electrical junction properties were characterized by temperature dependent current-voltage (I-V) characteristics and at high frequency capacitance – voltage (C-V) characteristic at room temperature. The structure showed non – ideal behavior of I-V characteristics with an ideality factor of 3.5 at room temperature. Temperature dependent forward current-voltage measurements suggest that trap-assisted multi-step tunneling is the dominant current mechanism in this structure.

3.4.1 Experiments

In order to prepare ZnO solution, firstly, zinc acetate 2-hydrate [Zn $(CH_3COO)_2$ $2H_2O$] was dissolved in ethanol (CH_3COCH_3 , 99.9%, Merck) and then lactic acid was added as hydrolysis catalyst in drops. Afterwards solution was thoroughly mixed by a magnetic stirs for 2 hours, and homogeneous transparent solution was obtained which had a concentration of 0.4M. Each coating on the ATO (Antimony Tin Oxide) substrate was first dried at 250^0 C for 5min. This process of coating was repeated for 10 times and then the final film was annealed at 250^0 C for 15 min.

CuO layer was deposited on ZnO. The CuO sol was prepared by adding copper 11 acetate ($(CH_3\ COO)_2$ Cu, H_2O) to ethanol and mixing the both components. While sol was mixing, the triethylamine was added in the sol. After the sol prepared, the CuO film was deposited on the ZnO film dried at 250^0 C for 5

min. This process of coating was repeated for 10 times and then the p – n junction was annealed at 250^0 C for 30 min.

After 10 coating for the ZnO film, thickness of the film was calculated $\sim 70nm$ and after 10 coating for the CuO film, it was calculated$\sim 212nm$.

After ZnO/CuO heterojunction was prepared, the contact was composed between the coated film and Cu wire. To insure good contact between the film and Cu wire. Ag paste was used. The crystal structure of the n- ZnO/p- CuO heterojunction was determined by XRD using Rikagu D-max 2200 X-Ray diffract meter system with CuKα radiation ($\lambda = 1.5405$)A^0 and by the UV – VIS spectroscopy (350 – 1100nm) using Perkin Elmer UV – VIS Spectrometer Lambda 2S. The current – voltage characteristics of the heterojunctions were measured with a system which consists of a DC voltage –current source Keithley 2420, a specially designed sample holder computer. Thin films samples were mounted in the sample holder. To control the temperature of the samples. Lake Shore 330 auto tuning temperature controller is used.

3.4.2 Results and discussion

The lattice constants of ZnO calculated from the present data are a=3.300 A^0 and c=5.131 A^0 which are agreement with a=3.253 A^0 and c=5.209 A^0 of ZnO known from the literature (JCPDS Card No. 80-00075) and the lattice constants of CuO calculated from the present data are a= 4.774 A^0, b= 3.434 A^0 and c=5.131 A^0 which are in agreement with the values a= 4.68 A^0, b=3.42 A^0 and c=5.129 A^0 of CuO obtained by kimura et al.

The band gab of ZnO and CuO were determined from measured transmittance spectra. We shows plot of the square of the absorption coefficient (α^2) of ZnO and CuO films fabricated

onto glass substrate as a function of the energy of incident radiation. For this, the fundamental absorption coefficient α was evaluated using $\alpha = lnT^{-1}$/d where d is the film thickness and T is the transmittance. The optical band gap, E_g of the film was calculated using the Tauc relation, which is given as $\alpha = \alpha_0 (h\nu - E_g)^n$ where hν is the photon energy. α_0 is a constant and n=0.5, 1.5, 2 or 3for allowed direct, forbidden direct, allowed indirect and forbidden indirect electronic transitions, respectively. In the present case the band -gap energy gap (E_g) has been estimated by assuming an allowed direct transition (n=1/2). The factor (α^2) varies linearly with hν in the high- energy region. In the low – energy region, the absorption spectrum deviates from the straight line. The band gap was obtained by extrapolating the linear portion of the plot of $(\alpha)^2$ against hν to $(\alpha)^2$ =0. The intercept on energy axis gives the value of the band gap energy (E_g) for the film. The band gap energy (E_g) values of ZnO and CuO are 3.3 and 1.8 eV respectively, which are in agreement with what have been reported previously.

XRD and UV- VIS measurements showed that ZnO films consisted of hexagonal wurtzite crystal grains with energy band gap of 3.3eV. At ambient conditions. The thermodynamically stable phase is hexagonal wurtzite, the cubic zinc blended ZnO structure can be stabilized only by layer growth on cubic substrates, and the cubic rock salt structure may be obtained at relatively high pressures. In our heterojunctions, the ZnO films were deposited onto the ATO substrates. The ATO films are a tetragonal system because tin oxide is a tetragonal system and the lattice parameters are not affected much the incorporation of the dopants in the films, is hexagonal wurtzite system. The CuO layer is monoclinic system. Since all layers at our heterojunction are different crystal systems, the lattice mismatch occur. To confirm

the presence of the interface state. We calculate the lattice mismatch given by the relation:

$$\frac{\Delta a}{a} = \frac{a_2 - a_1}{a_2} \qquad (3-3)$$

Where a_1 and a_2 are the lattice constant of the ZnO and CuO respectively. The lattice mismatch between CuO and ZnO calculated to be 32%, which is higher than the Cu_2O/ZnO heterojunction with mismatch of 7.1%, and Cu_2O/ZnO/ITO p-i-n heterojunction with the mismatch 27.1%. So the lattice mismatch leads to an interface defect states. In order to determine the dominant current transport mechanism through n-ZnO/p-CuO heterojunctions, we measured the I-V characteristics at various temperatures. The forward and reverse bias I-V graphics of ZnO/CuO heterojunction samples at different temperature in the range of 300-360 K. The sample was kept in the dark condition during the measurement. It is obvious that the heterojunction are rectifying in the nature with a turn on voltage of ~0.5Vand under reverse voltage. The breakdown voltage for the sample is ~0.6 V which is same as that of ZnO/Cu_2O heterojunction prepared by RF-magnetron sputtering and Cu_2O/ZnO/ITO p-i-n heterojunction prepared by electrochemical deposition method. The current at real diode were given at equation (3-5):

$$I = I_0\, exp\left(\frac{qV}{nKT}\right)\left[1 - exp\left(-\frac{qV}{KT}\right)\right] \qquad (3-4)$$

Where q is electronic charge, I_0 is the reverse saturation current, V is the applied voltage, n is ideality, k is Boltzmann constant and T is temperature. For $V > 3KT/q$ .Eq. (2-5) can also be shown as

$$I = I_0\, exp\left(\frac{qV}{nKT}\right) \qquad (3-5)$$

The ideality factor (n) is obtained from the slope of the plot In I versus V. The forward bias ln (I)-V characteristics of the samples at different temperature in the range of 300-360 K. The forward current can be classified into two regions. In the region 11, the forward currents behave linearly due to the serial resistance effect on the system. In region 1, the forward current can be expressed:

$$I = I_0 exp(AV) \qquad (3-6)$$

There are three models for explaining the current through heterojunctions: A is independent of the measuring temperature T for a tunneling model, (2) A is temperature, n=1, A=q/KT for the diffusion model, (3) A is temperature dependent, n=2, A=q/2KT for the recombination model. The ideality factor (n), the reverse saturation current I_0 which is a function of temperature, depending on the nature of dominant carrier transport mechanisms in the heterojunction and the slope of ln (I)-V graphics A(is independent of the voltage) of the samples are calculated from the graphics. In table 1, the slope A of the ln (I)-V graphicstemperature insensitive. Therefore, the data are consistent with Eq. (2.7). The ideality factor n is larger than 2.

Table (3.1).The I_0, A and n values for the sample of the n-ZnO/p-CuO heterojunction

T (K)	I_0 (A)	A (V^{-1})	N
300	1.36×10^{-9}	11.0	3.5
310	2.80×10^{-9}	10.1	3.7
320	2.80×10^{-9}	10.6	3.4
330	1.75×10^{-9}	9.7	3.6
340	1.26×10^{-9}	10.1	3.4
350	1.37×10^{-9}	10.0	3.3
360	1.84×10^{-9}	10.1	3.2

the temperature dependence of saturation current $I_0$is expressed as:

$$I_0 = I_{00} exp\left(-\frac{\Delta E_a}{KT}\right) \qquad (3-7)$$

Where ΔE_a is the thermal activation energy of carrier conduction. Form the slope of ln (I_0) versus T^{-1} graphics, the activation energy was calculated to be 0.412eV. The data fits almost on straight lines, which agrees with multi-step tunneling model. The capacitance per unit area given by Anderson

$$C = \left\{\frac{q\varepsilon_n\varepsilon_p N_a N_d}{2\left(\varepsilon_n N_d + \varepsilon_p\varepsilon_d\right)}\right\}(V_{bi} - V)^{-\frac{1}{2}} \qquad (3-8)$$

Where ε_n , ε_p are the dielectric constant and N_d, N_a are ionized impurity density of ZnO and CuO respectively, V_{bi} is the built in potential and V is the applied voltage. The capacitance-

voltage characteristics of n-ZnO/p-CuO heterojunction at MHz frequency in dark and at room temperature.

3.4.3 Conclusion

n-ZnO/p-CuO heterojunction has been successfully fabricated onto ATO substrates using sol-gel dip coating method. The thickness of ZnO film prepared by 10-times coating is ∼70nm while that of CuO film coated 10-times is ∼212 nm. At room temperature, the diode turn –on voltage is of ∼0.5V. The temperature dependent I-V characteristics of the n-ZnO/p-CuO heterojuncion showed that the forward current transport can be explained with a multi-step tunneling model between 300-360K. While the activation energy of the saturation current is about 0.412, the built-in potential is about 1.5eV [31].

3.5 Characterization of Cu_2O thin films prepared by evaporation of CuO powder

Introduction

Among the potential photovoltaic devices based on semiconductor oxides as active layer is cuprous oxide (Cu_2O). This oxide semiconductor shows many attractive characterizes useful for solar cells production such as low cost, nontoxicity, high mobility and diffusion length of minority carriers, high absorption coefficient and direct energy gap. In this work we report out results of optical and structural investigations of Cu_2O thin films fabricated by thermal vacuum evaporation of CuO powder. The effects of the deposition velocity on structural and optical properties of Cu_2O films were investigated. The X-ray investigations have shown that at low deposition velocity the films consist only of Cu_2O phase without any interstitial phase and have a nano-grain structure. The grains have an average dimensions about (25-30) nm and all these grains showed (200) preferential crystallographic orientation. Optical investigations

have shown that the absorption edge of prepared films is due to a direct allowed transition. The value of determined optical band gap is 2.05 eV which corresponds to band gap of bulk Cu_2O.

3.5.1 Experiments

Thin films of Cu_2O were fabricated by continuous thermal evaporation of CuO small particles. Schematic view of vacuum evaporation setup presented in figure (3.1). CuO particles have different size from 100 to 500 micrometers. These particles were prepped by crush of pallet which was obtained by pressing commercially available CuO powder (99.9% purity) and sintering at 700°C in air 1 h. The vacuum chamber before evaporation was pumped to a base pressure of 1.5×10^{-5} mm Hg. The thermal evaporation was carried out by dosed supply of CuO particles to the molybdenum boat heated to the temperature 1300°C. Process of CuO particles evaporation occurred as follows. After contact to boat the particles of CuO in process of their heating at first convert to Cu_2O by the reaction:

$$4CuO \rightarrow 2Cu_2O + O_2 \qquad (3\text{-}1)$$

And then convert to Cu by the reaction:

$$2Cu_2O \rightarrow 4Cu + O_2 \qquad (3\text{-}2)$$

Since the temperature of boat was above the temperature of Cu evaporation (1260°C) after thermal decomposition of Cu_2O to Cu and O_2 a full evaporation of Cu was occurred. This method of evaporation provides in average the same flows of copper and oxygen atoms due to different temperature of evaporating particles.

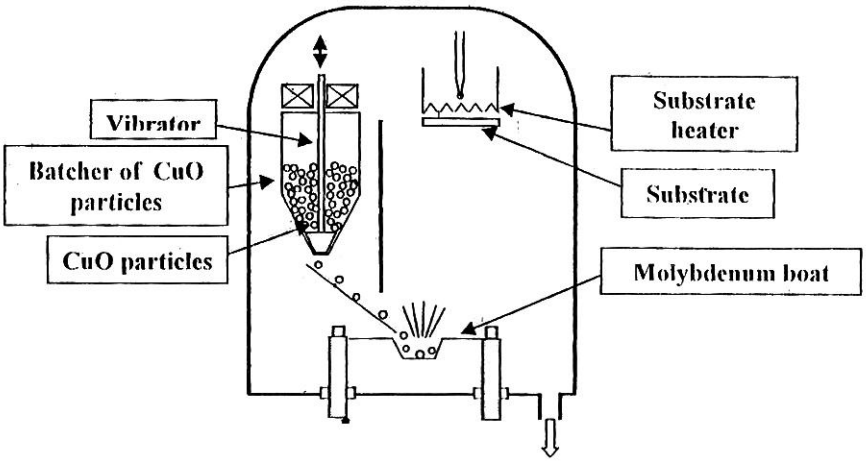

Figure (3-1): schematic representation of the experimental setup

The films were deposited on sapphire substrate. The temperature of substrates was 700°C. During the evaporation process the base pressure in vacuum chamber was changed from base pressure 1.5×10^{-5} mm Hg to the partial pressure of oxygen 1.10^{-4} mm Hg. After the film deposition the substrate was cooled to the room temperature during 1 hour with the chamber pressure 6.10^{-6} mm Hg. The film thickness and duration of deposition were typically 1-3 micrometer and 3 hours.

The structural properties of samples were studied by X-ray diffract meter URD-6 in the 0-20 mode using Cu-Kα radiation as well as by optical Olympus microscope with magnitude 500. Transmittance and reflectance, over the wavelength from 300 to 1000 nm was measured using double beam Spectra M-50 Spectrophotometer.

3.5.2 Results and discussion

Phase formation

We have investigated the characteristics of films depend on the deposition velocity at the temperature of substrate 700°C. Figure (3-2) shows the photo of surface morphology of two films series A and B which differ from each other by the velocity of deposition. For low deposition velocity less than 5 nm/min the

films of series A consist of smaller size grains than the films of series B (figures (3-2) a and b).

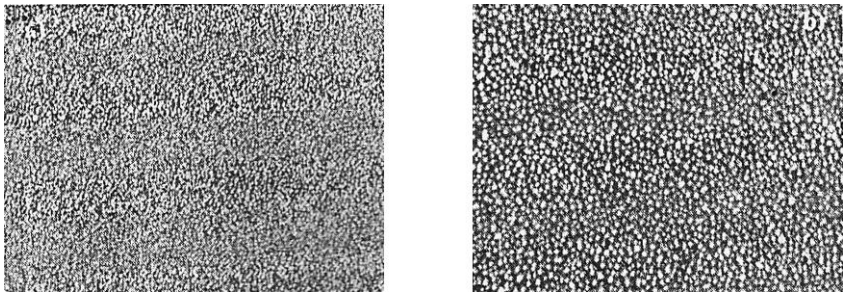

Figure (3-2): the photo of surface morphology of (a) films series A, and (b) films series B (500)

Structural analysis (XRD)

Angler XRD patterns of films series A and B are shown figure (3-3) For films series A, there is one strong XRD peak at 20=42.4° corresponding to the (200) crystal plane of Cu_2O (figure (3-3a). This XRD pattern indicates that films series A is single phase Cu_2O film with crystalline structure. These films consist of nano-size grains and all these grains have identical orientation. Full width of half maximum (FWHM) of the XRD peak was used to estimate the grain size of the films series A. The values of the grain size calculated using Scherer's formula:

$$D = \frac{0.9\lambda}{d.\cos\theta} \qquad (3-3)$$

Where λ is the x-ray wavelength, θ is the Bragg diffraction angle, and d is full- width at the half maximum (FWHM) of the peak corresponding toθ.

For the peak corresponding to the (200) plane of Cu_2O, the resultant grain size is 25 nm. The XRD pattern for films series B presented in figure 3b contains one Cu_2O – related diffraction (111) peak (20-36.38°) and tow Cu- related diffraction peak (111) (2 θ =42.9°) and (200) (2 θ = 49.8°).

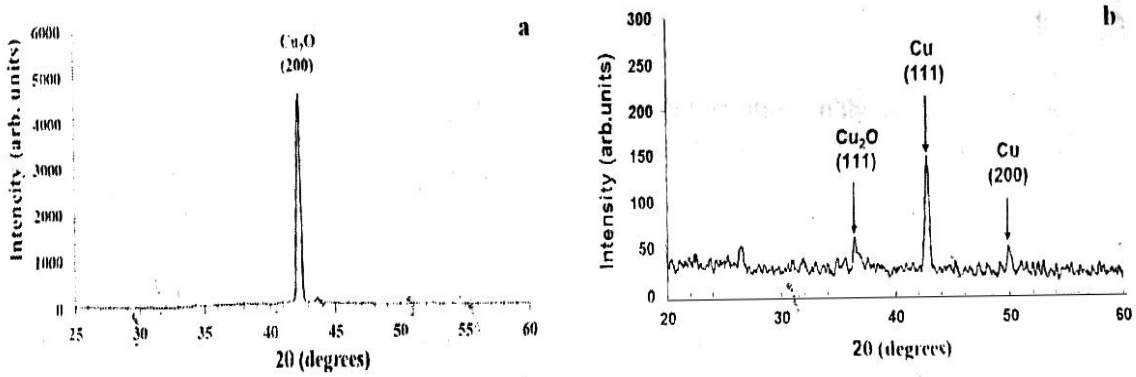

Figure (3-3): XRD patterns of (a) films series A, and (b) films series B

The composition of deposited layer formed due to reaction between cupper and oxygen. Figure (3-4) shows the equilibrium phase diagram of the Cu-O system. The partial pressure and temperature of substrate corresponding to the films deposition conditions are shown in figure (3-4) (point A). At low velocity of deposition Cu atoms have enough time in order to completely react to oxygen. This time determined by the time of kinetic reaction for formation Cu_2O phase. In this case the composition of deposited film determined by the equilibrium Cu-O phase diagram. It is confirmed by XRD pattern of films series A where observe only Cu_2O- related diffraction peaks. We believe that at high velocity of deposition Cu atoms have not enough time to completely convert in Cu_2O phase (figure (3-3b).

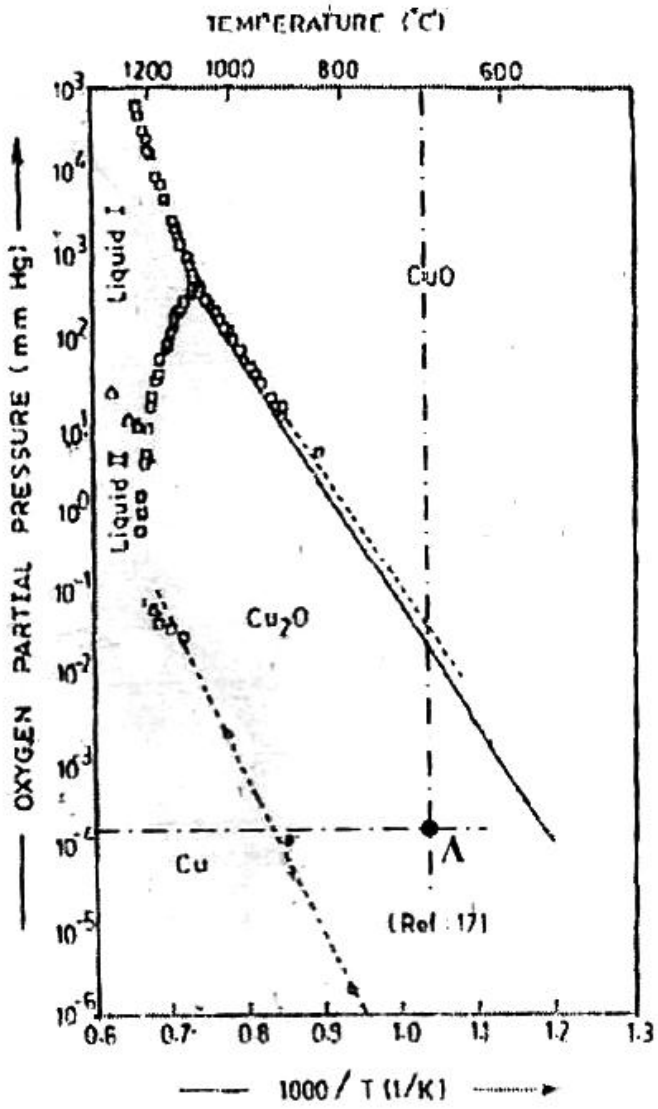

Figure (3- 4): The cooper – oxygen equilibrium phase diagram

Optical properties

The transmission and absorbance spectra were taken to obtain information on the optical properties of the copper oxide thin film. In the fundamental absorption region, the optical absorption coefficient (α) can be calculated from the transmittance and reflectance data by the equation.

$$\alpha = \frac{1}{d} In \frac{(1-R)}{T} \qquad (3-4)$$

Where d is the thickness of the film.

Above the fundamental absorption edge the dependence of the absorption coefficient on the incident photon energy is given by Taue's model:

$$\alpha . hv = B\left(hv - E_g\right)^n \qquad (3-5)$$

Where hv is the photon energy, E_g is the optical band gap and B is a constant and n is an exponent that depends on the type of optical transitions. As shown in figure (3-5) the best linear relationship is obtained by plotting $(\alpha . hv)^2$ against photon energy (hv), indicating that the absorption edge in this film is due to a direct allowed transition. The linear portion of the curve is fitted using linear regression analysis. The value of optical band gap was determined from the value of intercept of the straight line at $\alpha = 0$ the value of determined optical band gap is 2.05 eV which corresponds to the band gap of bulk Cu_2O.

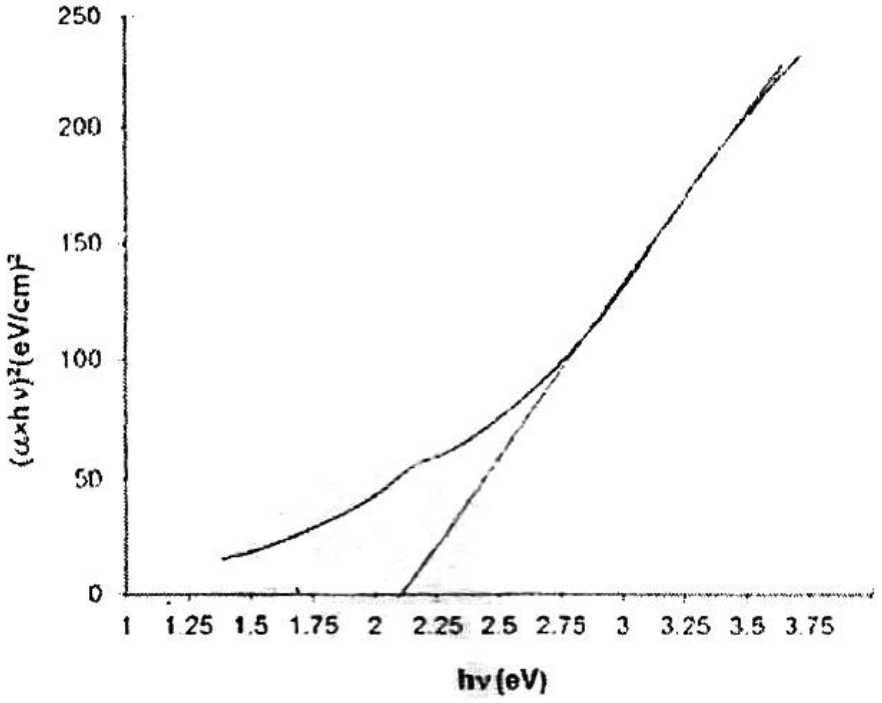

Figure (3-5): Variation of $(\alpha hv)^2$ as a function of photon energy

3.5.3 Conclusion

The films of copper oxide were deposited on sapphire substrate by the continuous thermal evaporation of CuO small particles. The effects of deposition velocity on the structural and optical properties of Cu_2O films were investigated. It was shown that at deposition velocity less than ∼5 nm/min the films deposited on the 700°C substrate consist only of Cu_2O phase. These films have n nano-grain structure and all these nana-grains have (200) preferential crystallographic orientation with average dimensions about (25-30) nm.

It was found that the optical band gap of fabricated Cu_2O films is 2.05 eV which corresponds to the hand gap of bulk Cu_2O[32].

3.6 Characterization of Dye-Sensitized solar cell with ZnO Nanorod multilayer electrode

3.6.1 Introduction

In this study, zinc oxide (ZnO) nonrods were synthesized on indium-tin-oxide (ITO) glass substrates by a hydrothermal process. The growth process was carried out one to five times to obtain ZnO nanorods of different generations (1^{st} to 5^{th} generation). Scanning electron microscopy (SEM), energy dispersive spectrometry (EDS).

And x-ray diffraction (XRD) was used to obtain the surface morphology, chemical composition, and crystallographic structure of the synthesized ZnO nanorods. These ZnO nanorods were submerged in the dye solution and ware used as the working electrode (anode) of dye-sensitized solar cell (DSSC). I-V and optoelectronic characteristics of the DSSCs using ZnO nanorods of different generations as the electrodes were measured to obtain their fill factors and conversion efficiency. Experimental results reveal that the ZnO film of the 4^{th} generation exhibits a uniform distribution of dense nanorods whose shape and microstructure

are beneficial to dye adsorption and carrier transport. Therefore, the DSSC fabricated with the ZnO nanorods of the 4th generation has an improved short-circuit current, fill factor, and conversion efficiency.

3.6.2 Experiments Details

In this work, ZnO nanorods prepared by a simple hydrothermal process were used to fabricate the working electrodes for DSSC applications. First, indium-tin-oxide (ITO) glass substrate was cut into 2 cm × 2 cm pieces, and then rinsed with acetone, methanol and deionizer water. After cleaning, the ITO glass substrates were blown with nitrogen to dry. Transparent tapes were adhered along the peripheral of ITO glass substrate. Only the central area of 1 cm x 1 cm was reserved for the growth for ZnO nanorods. In addition to ITO substrates, ZnO nanorods were also synthesized on silicon substrates since they are more suitable for SEM and EDS measurements. Second, deionized water was added to zinc nitrate hexahydrate (Zn $(NO_3)_2$ $6H_2O$) and methenamine ($C_6H_{12}N_4$, HMT) to obtain the reagents used for the growth of ZnO nanorods. These two solutions were mixed at the ratio of 1:1 to obtain a mixture of 0.1 M molar concentration. The mixed solution was vigorously stirred for 20 min at room temperature to ensure full and uniform mixing. The mixture was heated indirectly through water at 85°C. After the temperature of mixture was stabilized, ITO glass substrates were submerged in the mixture with ITO facing upwards. After 1 hr of high temperature process, samples were removed from the beaker and were rinsed with deionized water for 20 min to halt the growth process of ZnO nanorods. Finally, the synthesized ZnO samples were placed into a box for 5 hours so that they can dry by themselves.

This completed the growth process of ZnO, and the ZnO nanorods of the 1st generation were achieved. The 2nd, 3rd 4th and 5th growth processes were then carried out sequentially to obtain the ZnO nanorods of 2nd, 3rd, 4th, and 5th generations. The ZnO

nanorods synthesized in the previous growth process were used as the starting point of the next growth process and were covered by the ZnO nanorods synthesized in the next growth process. The processing parameters (e.g. molar concentration of mixture, growth temperature, and growth time) in all subsequent growth processes of ZnO were the same as those used in the 1st growth process.

After the working electrodes using ZnO nanorods of different generations were fabricated, they were submerged in the dye solution for 8 hours so that the dye can be fully adsorbed by ZnO nanorods. Subsequently, the working electrodes were assembled with the counter electrode of Pt film/ITO glass and electrolyte was injected to from DSSC.

The purpose of this work is to study the surface morphology, chemical composition, and microstructure of the ZnO nanorods of different generations. Scanning electron microscopy (SEM), energy dispersive spectrometry (EDS) and (XRD) were used to obtain the surface morphology, chemical composition, and crystallographic structure of ZnO nanorods. Afterwards, I-V characteristics of the $DSSC_s$ using ZnO nanorods of different generations were measured, and open-circuit voltage, short-circuit current, fill factor, and conversion efficiency were determined.

3.6.3. Results and Discussions:

In this study, zinc nitrate hexahydrate (Zn $(NO_3)_2$, $6H_2O$) and hexamethylene tetramine ($C_6H_{12}N_4$, HMT) were mixed at the ratio of 1:1 in water. The molar concentration ratio of Zn $(NO_3)_2.6H_2O$ and C6H12N4 was 1 : 1 which was the optimum value determined from our previous experimental results. HMT is non-toxic and its water-soluble polymer ring dissolves in acidic solution into functional groups to form NH3. $Zn(NO_3)_2$ can react with HMT in water to synthesize ZnO nanorods. The chemical reactions involved in the growth of ZnO nanorods are:

$$C_6H_{12}N_4+6H_2O\rightarrow 6HCHO+4NH_3 \quad (3\text{-}6)$$

$$NH_3+H_2O\rightarrow NH_4+OH^- \quad (3\text{-}7)$$

$$2OH^-+Zn^{2+}\rightarrow ZuO+H_2O \quad (3\text{-}8)$$

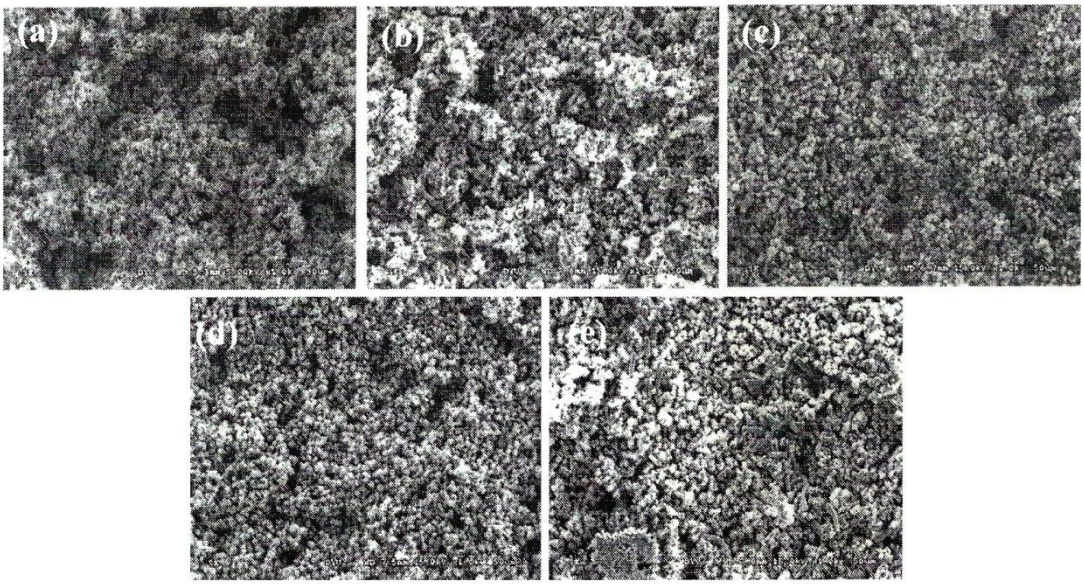

Figure (3-6). The top-view SEM images of ZnO nanorods of the: (a) 1st , (b) 2nd , (c) 3rd (d) 4th , and (e) 5th generations. The magnification factor is 1×10^3.

First, $C_6H_{12}N_4$ is disintegrated into formaldehyde (HCHO) and ammonia (NH_3) as shown in equation (3-6). Ammonia tends to disintegrate water to produce OH^- anions (equation 3-7). Finally, OH anions react with Zn^{+2} cations to form ZnO (equation 3-8). In the growth process of ZnO nanorods, the concentration of OH^- anions is the dominant factor. Therefore, $C_6H_{12}N_4$ that supplies OH^- anions play a key role in the growth of ZnO nanorods.

The hydrolysis rate of $C_6H_{12}N_4$ is low and thus can provide OH^- anions at a steady rate rendering a solution with a constant concentration of 0H anions. At low concentrations of $C_6H_{12}N_4$ + $Zn(NO_3)_26H_2O$, the reaction rate of OH^- anions is low: on the other hand, the reaction rate and the growth rate of ZnO nanorods is high at high concentrations of $C_6H_{12}N_4$ + $Zn(NO_3)_26H_2O$. In

this study, the molar concentration of mixture used in the growth process was 0.1M. Since our previous study has demonstrated that DSSC using ZnO nanorods electrode prepared with 0.1 M mixture, same concentration of mixture was used in this work to study the effect of ZnO nultilayer electrode on the operating characteristics of DSSC.

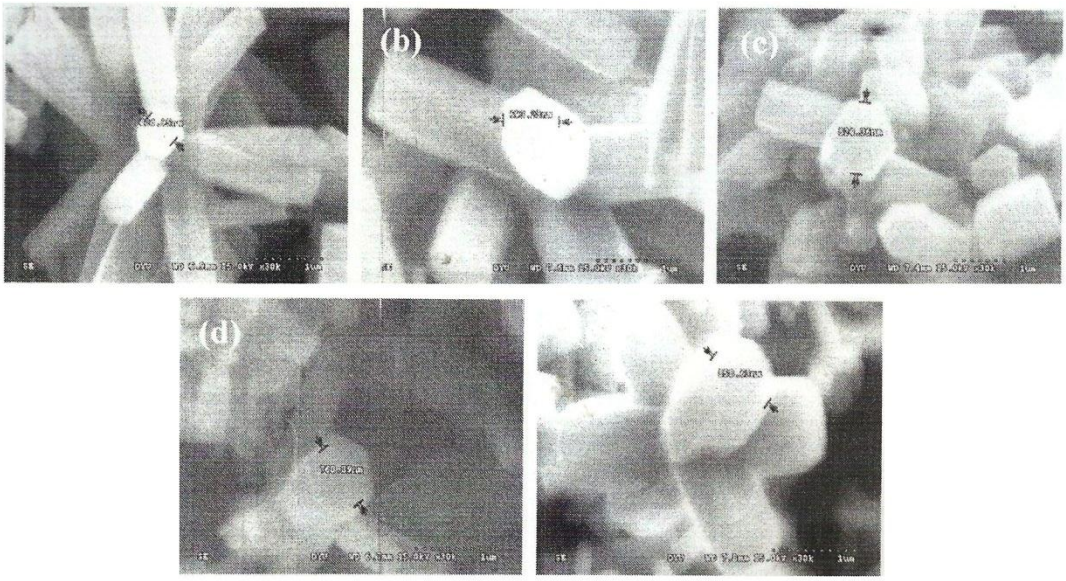

Figure (3-7). The enlarged SEM images of ZnO nanorods of the: (a) 1^{st} , (b) 2^{nd} , (e) 3^{rd} (d) 4^{th} , and (e) 5^{th} generations. The magnification factor is 3×10^4.

Table (3.2). Chemical composition for the ZnO nanorods of different generations.

Chemical composition	Atomic percentage (%)				
	1^{st}	2^{nd}	3^{rd}	4^{th}	5^{th}
O	77.82	60.18	53.49	52.85	50.60
Si	2.80	0	0	0	0
Zn	19.37	39.82	46.51	47.15	49.40
Zn:O	1:4.02	1:1.51	1:1.15	1:1.12	1:1.02

Figure (3.7) shows the top-view SEM images of ZnO nanorods of

different generations, while the enlarged images arc shown in the Figure 2. The magnification factor is 1×10^3 for Figure (3.7), and is 3×10^3 for Figure (3.8). The growth parameters are listed as follows: the growth temperature was 85°C, growth time was 1 hr, the molar concentrations of

$Zn(NO_3)_2.6H_2O$ and $C_6H_{12}N_4$ were 0.1M (the molar ratio was 1:1), and the growth process was repeated 1 to 5 times.

From Figure (3-7)(a), (b), (c), (d), and (e), it is clearly seen that no obvious change in the surface morphology of ZnO nanorods of different generations can be observed. Figure (3-7)(a) shows the ZnO nanorods of the 1st generation which is obtained with a mixture solution of 0. 1M. the average diameter of ZnO nanorods is ~ 420 nm. The average diameter of nanorods increases logarithmically from ~ 693 nm for the ZnO of the 1^{st} generation to 858 nm for the ZnO of the 5th generation. As shown in Figures (3-7) (d) and (e), the shape of nanorods tends to become short and wide. Since fresh mixture solution was added before every growth process in order to maintain a constant ion concentration of 0.1M in the solution, the ZnO nanorods that have been adhered to the substrate already will have the opportunity to replenish newly added anions. Since the growth rate on the six side walls is higher than that on the tip surface, it is reasonable for the shape of ZnO nanorods to become short and wide after multiple growth processes.

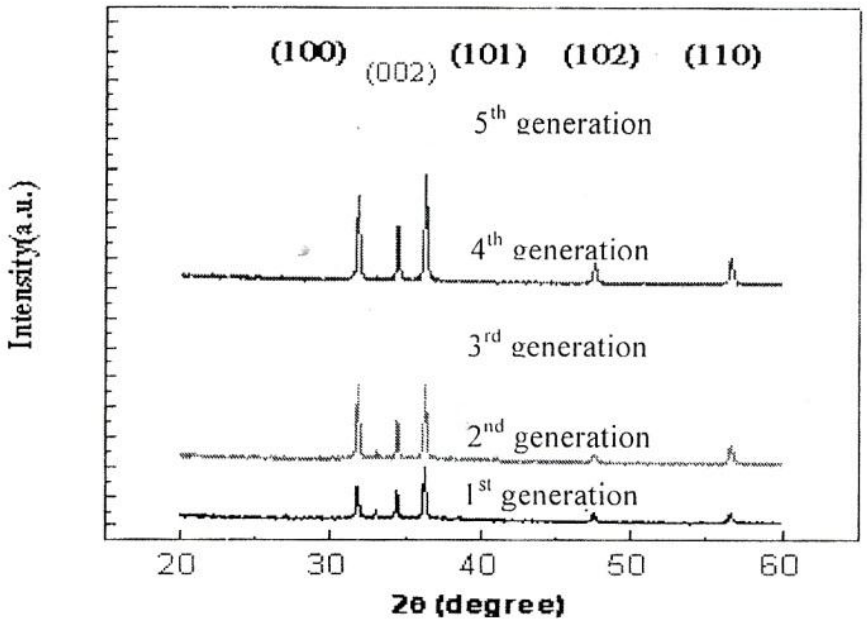

Figure (3-8). XRD spectra for the ZnO nanorods of different generations.

Table (3.3). Intensities of characteristic peaks in XRD spectra for the ZnO nanorods of different generations.

Generation of ZnO	Ia	Ic	Ib	Ia/Ic	Ib/Ic
1st	602	511	893	1.18	1.74
2nd	829	653	1169	1.27	1.79
3rd	959	710	1292	1.35	1.82
4th	1502	1058	2000	1.42	1.89
5th	1669	1135	2290	1.47	2.02

In this study, EDS used to measure the chemical composition of ZnO nanorods of different generations and is listed in Table I. As observed in the EDS analysis, the atomic content of silicon in the Zn() nanorods of the 1st generation is 2.8%. Since no silicon-containing reagent was used in the growth process. The detected silicon content is caused by silicon atoms on the substrate.

Obviously, the ZnO nanorods were not dense enough to completely. Cover the entire substrate. As the ZnO nanorods evolve into the 2nd generation. The atomic percentage of silicon drops to 0% indicating that the distribution of ZnO nanorods is uniform and dense. The silicon substrate is completely covered by ZnO nanorods. This is beneficial to the uniform adsorption of dye molecules. The chemical composition for ZnO nanorods of different generations can be clearly seen in table 1. It seems that the atomic ratio of zinc to oxygen decreases as the ZnO nanorods evolve. The atomic ratio of zinc to oxygen on the surfaces of nano rods is 1:4.02 for the ZnO nanorods of the 1st generation. Whereas this atomic ratio decreased to 1:1.02 for the ZnO nanorods of the 5th generation which is close to the theoretical value of 1 as is expected for ZnO.

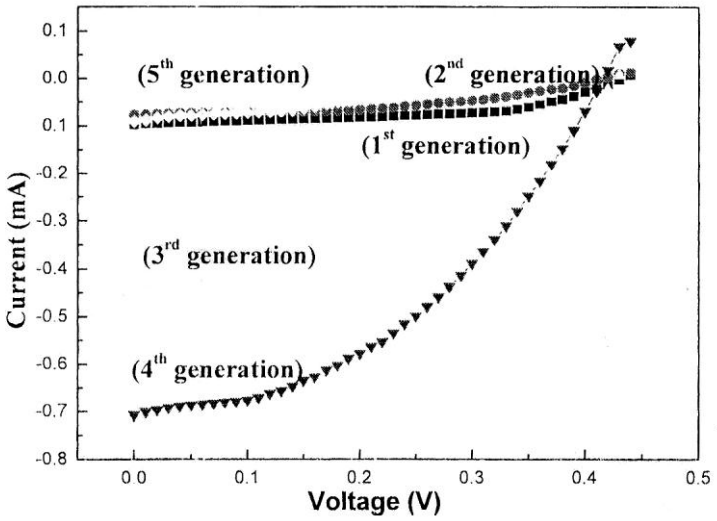

Fig (3-9)I-V characteristics for the DSSC using ZnO nanorods of different generations as the working electrode.

Figure (3-4) shows the XRD spectra for the ZnO nanorods of different generation. In figure (3-4), all spectra exhibit five peaks located at diffraction angles of 2seta=31.77^0. 34.42^0 and 36.25^0 are most pronounced. These three peaks correspond to (100),(002), and (101) directions of crystallization of wurtzite ZnO nanorods, i.e the growth along the directions of a, b, and c

axis of nanorod hexagonal structure, respectively. These intensities of characteristic peaks in XRD spectra for the ZnO nanorods of the different generation are summarized in Table 2. In the different spectra, the intensity ratio in the direction of axis and c axis (I_a/I_c) and the intensity ratio in the direction of axis and c axis (I_b/I_c) are useful. As ZnO nanorods evolve from the 1^{st} generation to the 5^{th} generation, the values of I_a/I_c and I_b/I_c increase. The value of I_a/I_c increase from 1.18 to 1.47. and I_b/I_c increases from 1.74 to 2.02. The aspect ratio of nanorod also increases with the evolution of ZnO nanorods.

This is because the increases in the growth rate on the (100) and (101) surfaces of ZnO nanorods are higher than that on the (002) surface. Hence, nanorods become short and wide. This assertion is verified by the SEM image in Figure 1(e.

Figure(3-5) shows the I-V characteristics of the $DSSC_s$ fabricated with ZnO nanorods of different generations. The corresponding open-circuit voltage (V_{oc}), short-circuit current (I_{sc}), and fill-factor (FF) are tabulated in Table 3. For the $DSSC_s$ prepared with ZnO nanorods of the 4^{th} generation exhibits much improved short-circuit current and fill factor., and hence a much higher conversion efficiency. However, it is found that the $DSSC_s$ prepared with ZnO nanorods of the 5^{th} generation has a lower short-circuit current, open-circuit voltage, fill factor, and hence a lower conversion efficiency. Possible explanations are given s follows. For the ZnO nanorods of the 1^{st} generations, the distribution of nanorods on the ITO glass substrates is not uniform. Lots of voids and vacancies are found in the ZnO film so that dyes can not uniformly adsorbed in the film. Therefore, the DSSC prepared with the 1^{st} generation ZnO nanorods exhibit poor *I-V* characteristics. The distribution of ZnO nanorods of the 2^{nd} generation is still non-uniform indicating that there are some voids and vacancies in the ZnO film. This can affect the adsorption of dye molecules so that only slight improvement in the *I-V* characteristics of DSSC can be achieved. For the $DSSC_s$

using ZnO nanorods of the 3rd and 4th generation. Substantial improvement in their *I-V* characteristics is evident. Compared with the DSSC prepared with ZnO nanorods of the 1st generation, short-circuit current increases by a factor of 7 for the DSSC using ZnO nanorods of the 4th generation, and a large increase in the conversion efficiency of DSSC is achieved. From the atomic ratio of zinc to oxygen in EDS analysis, the structure of the ZnO nanorods of the 3rd and 4th generations is considerably better than that of the ZnO nanorods of the 1st and 2nd generation. Much fewer bonding vacancies are present in the nanorods. Therefore, electron is easier to travel in these films and the conversion efficiency of DSSC is increased.

The reason for the degeneration in the I-V characteristics as found in the DSSC prepared with ZnO nanorods of the 5th generation is presumably caused by the larger thickness of ZnO film. The distance which electrons have to travel through the ZnO film is increased, thus electron-hole recombination is more likely to take place and photocurrent is decreased according. Furthermore, the average diameters of ZnO nanorods become larger for the ZnO nanorods of the 5th generation so that the aspect ratio of nanorods increases and nanorods become short and wide. The voids and vacancies lying between nanorods become larger and intimated contact between nanorods is unlikely now. This results in an increase in the internal resistance of working electrode. FF factor and conversion efficiency are decreased drastically and operating characteristics of DSSC are severely degraded.

characteristic peaks. Of these five peaks, the diffraction

Figure 3 shows the XRD spectra for the ZnO nanorods of different generation. In figure 3, all spectra exhibit five peaks located at diffraction angles of 2seta=31.77^0. 34.42^0 and 36.25^0 are most pronounced. These three peaks correspond to (100),(002), and (101) directions of crystallization of wurtzite ZnO nanorods, i.e the growth along the directions of a, b, and c

axis of nanorod hexagonal structure, respectively. These intensities of characteristic peaks in XRD spectra for the ZnO nanorods of the different generation are summarized in Table 2. In the different spectra, the intensity ratio in the direction of axis and c axis (I_a/I_c) and the intensity ratio in the direction of axis and c axis (I_b/I_c) are useful. As ZnO nanorods evolve from the 1^{st} generation to the 5^{th} generation, the values of I_a/I_c and I_b/I_c increase. The value of I_a/I_c increase from 1.18 to 1.47. and I_b/I_c increases from 1.74 to 2.02. The aspect ratio of nanorod also increases with the evolution of ZnO nanorods.

This is because the increases in the growth rate on the (100) and (101) surfaces of ZnO nanorods are higher than that on the (002) surface. Hence, nanorods become short and wide. This assertion is verified by the SEM image in Figure 1(e.

Figure 4 shows the I-V characteristics of the $DSSC_s$ fabricated with ZnO nanorods of different generations. The corresponding open-circuit voltage (V_{oc}), short-circuit current (I_{sc}), and fill-factor (FF) are tabulated in Table 3. For the $DSSC_s$ prepared with ZnO nanorods of the 4^{th} generation exhibits much improved short-circuit current and fill factor., and hence a much higher conversion efficiency. However, it is found that the $DSSC_s$ prepared with ZnO nanorods of the 5^{th} generation has a lower short-circuit current, open-circuit voltage, fill factor, and hence a lower conversion efficiency. Possible explanations are given s follows. For the ZnO nanorods of the 1^{st} generations, the distribution of nanorods on the ITO glass substrates is not uniform. Lots of voids and vacancies are found in the ZnO film so that dyes can not uniformly adsorbed in the film. Therefore, the DSSC prepared with the 1^{st} generation ZnO nanorods exhibit poor *I-V* characteristics. The distribution of ZnO nanorods of the 2^{nd} generation is still non-uniform indicating that there are some voids and vacancies in the ZnO film. This can affect the adsorption of dye molecules so that only slight improvement in the *I-V* characteristics of DSSC can be achieved. For the $DSSC_s$

using ZnO nanorods of the 3rd and 4th generation. Substantial improvement in their *I-V* characteristics is evident. Compared with the DSSC prepared with ZnO nanorods of the 1st generation, short-circuit current increases by a factor of 7 for the DSSC using ZnO nanorods of the 4th generation, and a large increase in the conversion efficiency of DSSC is achieved. From the atomic ratio of zinc to oxygen in EDS analysis, the structure of the ZnO nanorods of the 3rd and 4th generations is considerably better than that of the ZnO nanorods of the 1st and 2nd generation. Much fewer bonding vacancies are present in the nanorods. Therefore, electron is easier to travel in these films and the conversion efficiency of DSSC is increased.

The reason for the degeneration in the I-V characteristics as found in the DSSC prepared with ZnO nanorods of the 5th generation is presumably caused by the larger thickness of ZnO film. The distance which electrons have to travel through the ZnO film is increased, thus electron-hole recombination is more likely to take place and photocurrent is decreased according. Furthermore, the average diameters of ZnO nanorods become larger for the ZnO nanorods of the 5th generation so that the aspect ratio of nanorods increases and nanorods become short and wide. The voids and vacancies lying between nanorods become larger and intimated contact between nanorods is unlikely now. This results in an increase in the internal resistance of working electrode. FF factor and conversion efficiency are decreased drastically and operating characteristics of DSSC are severely degraded.

Table (3.4). Open-circuit voltage (Voc), short-circuit current (Isc), and fill factor (FF) for the DSSCs using ZnO nanorods of different generations as the working electrode.

Generation of ZnO	V_{oc}(V)	Isc(A)	FF(%)
1^{st}	0.44	9.812×10^{-5}	53.101
2^{nd}	0.43	1.694×10^{-4}	44.287
3^{rd}	0.43	4.477×10^{-4}	44.050
4^{th}	0.42	7.074×10^{-4}	41.979
5^{th}	0.37	2.348×10^{-4}	40.745

3.6.4 Conclusions

In this study, ZnO nanorods of different generations were used as the working electrodes for DSSCs. Experimental results reveal that the average diameter of ZnO nanorods increases with the evolution of ZnO nanorods.

As the ZnO nanorods evolve, the shape of ZnO nanorods varies from long, slender hexagonal column to short, wide rods after multiple growth processes. As the ZnO nanorods evolve into the 4uh1 generation, substantial improvement in the open-circuit voltage, short-circuit current, and conversion efficiency of DSSC are achieved. As the ZnO nanorods evolve into the 515 generation, the average diameter of nanorods increases to lower the specific surface area.

Less dye molecules are adsorbed which makes the photocurrent decrease. Another possible reason is the increase of internal resistance in the ZnO nanorods working electrode which can also lower fill factor and conversion efficiency[33].

3.7 Summery and critique

Many attempts were made to develop solar cells [34,35,36,37]. In some of them polymers were used [38,39,40,41], in other titanium oxides and dyes were used [42,43,44,45]. Unfortunately these cells are chemically unstable due to the fact that organic materials are affected by environment strongly. There is thus need for stable cells of metallic origin.

Chapter 4

Result and discussion

4. Introduction

The purpose of this work is to clue the current transport mechanism of n-ZnO/p- CuO heterojunctions. In this study is to fabricate two types of solar cells. The first type is FTO/CuO/ZnO/Al and the second type is FTO/ZnO/CuO/Al. Six samples were prepared from each types. The efficiency for each type was obtained. The FTO and CuO acts as p-type semiconductor, while ZnO act an n- type semiconductor. Thus the first type acts pnp component, while the second type acts ppn component.

Photovoltaic (PV) technologies, which convert solar energy directly in electricity, are playing an ever increasing role in electricity production worldwide. In this study, a n- ZnO/p- CuO and CuO/ZnO heterojunction was fabricated by electro deposition technique. Then the optical, structural and electrical properties of the samples were studied by the UV-VIS spectroscopy.

4.1 Material and method

4.1.1 Description of the Materials

4.1.2 Zinc Oxide (ZnO)

Zinc oxide is considered as an excellent material in this work because of it is a wide band gap ($\sim 3-3.5ev$), high free carrier concentrations for electron conduction (10^{18} cm^{-3}), and very similar electron affinity (4.35eV) [23]. ZnO has been applied in various electrical and optical device, such as solar cells, light emitting device, gas sensors, and photo detectors. However, it is difficult to fabricate high quality p-type ZnO semiconducting material because of the oxygen vacancies and zinc interstitials an un-doped ZnO, which enable ZnO to show n-type semiconductor properties [23]

These properties suggest minimal voltage loose during charge transport across the interface. The oxide has been shown to form a chemically stable p-n hetero junction [24, 25]. Such that the photo generated electrons (minority carriers) from the absorber can be collected effectively and transported to their respective contacts with minimal current losses.

Also the low toxicity and relatively easy processing of ZnO makes it an attractive with other materials. As n-type metal oxide semiconductors [26, 27], Zinc oxide (ZnO) has attracted intensive research attention owing to its diverse interesting properties such as electro-optical, piezo electronic and magnetic properties. Which a direct band gap and relatively large exciting binding energy of (60 meV) [28].

4.1.3 Cupric Oxide (CuO)

Cupric oxide (CuO) is anther metal oxide material that has been substantially explored for furious fields of applications. As a p-type semiconductor having a narrow band gab of (1.35eV), CuO has great potential as afield emitter, catalyst and as a gas sensing medium. The physiochemical properties of CuO such as the photo conductivity and the photo chemistry can be tailored for fabricating optical switches and solar cells. [29].

As a solar material, cuprous oxide Cu_2O has the advantages of low cost, great availability, non-toxic nature for use in thin film solar cells, a theoretical solar efficiency of about 9-11% an abundance of copper and the simple and inexpensive process for semiconductor layer formation. In addition to everything else. Cuprous oxide has band gab of 2.0eV which is within the acceptable range for solar energy conversion; because all semiconductors with band gab between 1eV and 2eV are favorable materials for photo voltage cells [30, 31].

4.1.4 FTO substrate

Compounds used for functionalization of the FTO electrodes are presented in the Fig. ***. The following silanes were used N-3-(Trimethoxysilyl) propyl-N,N,N-trimethylammonium chloride (1 denoted as TMATMS) from ABCR GmbH and N-3-(Trimethoxysilyl)propyl-N-octadecyl-N,N-dimethylammonium chloride (2 denoted as ODMATMS) from Aldrich. As the ion complexone, 4,4′,4″,4‴-(Porphine-5,10,15,20-tetrayl)tetrakis(benzoic acid) (3 denoted as Porphine) and 3-(2-pyridyl)-5,6-bis(4-phenylsulfonic acid)-1,2,4-triazine, monosodium salt (4 known as Ferrozine) were used, both purchased from Aldrich.

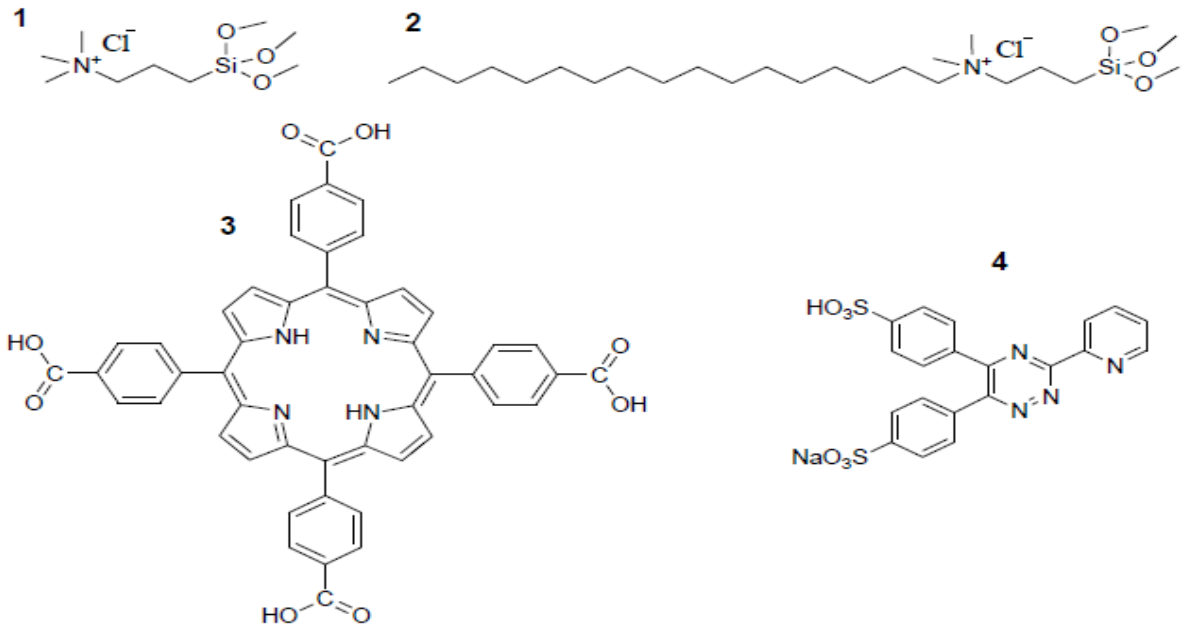

Figure 4-1. Compounds used for the functionalization of the FTO coated electrodes. 1 – TMATMS, 2- ODMATMS, 3-Porphine, 4-Ferrozine.

4.1.5 Spin coater

Usually a thin film is made by the spin coating method. It is versatile and simple .The number of round depended of the voltage, the number of round proportional increases with the voltage, then the thickness decreases with an increase in the number of round.

Fig (4-2): Spin coating device

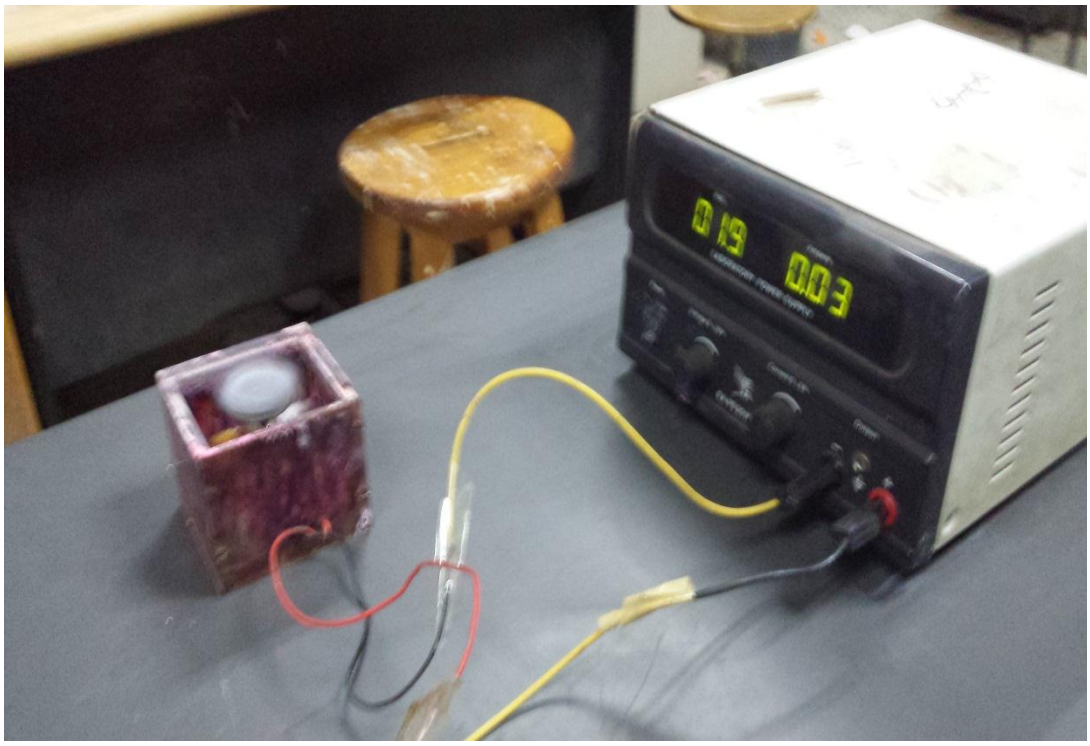

Fig (4-3): Spin Coating for the sample

4.1.6 UV-VIS.1240 Spectrophotometer

This device was used to measure the absorption and to transmission of the solutions and solvents before use in cavity. It is covering a wavelength from 190-1100 nm with auto lamp switch from visible to ultra violet range. UV-VIS Spectrophotometer from SHIMADZU contains a cell of thickness 0.1 mm as a sample holder.

4.2 preparation of the thin film

Avery simple apparatus was used for electro deposition its consisted of CuO layers were prepared on pre- cleaned fluorine – doped tin oxide (FTO) glass plate by electro deposition using platinum counter electrode. Two electrodes (cathode and anode) and a standard electrical circuit for electrolysis.

The deposition solution contained copper sulfate (($CuSO_4$) 0.4mol/l, wako 97.5%) and lactic acid ($C_3H_6O_3$)(3 mol/l wako)were dissolved in to distilled water. PH of the electrolyte

solution was adjusted to 12.5 by adding NaOH. The temperature of electrolyte solution was kept at 650^0C during electro deposing, Preparations of CuO layer were carried out at voltage of +0.70V and quantity electric charge of 2.2Ccm^{-2}. After the deposition, the sample was rinsed with water and transferred in to the ZnO electro deposition bath.

ZnO layers were electrodeposited from 0.025M aqueous solution of Zn (NO_3) of the FTO/CuO substrate. Finally, the substrate were rinsed with water, dried we use the spin coating and quickly transferred in to a thermal evaporator for the vacuum deposition of the aluminum (Al) back contact. The structure of hetero junction solar cells were denoted as: FTO/CuO/ZnO/Al (six samples from 1 - 6) and FTO/ZnO/CuO/Al also (six samples from 7 – 12) with schematic illustration as shown in figure (3-4) set up.

4.3 Setup

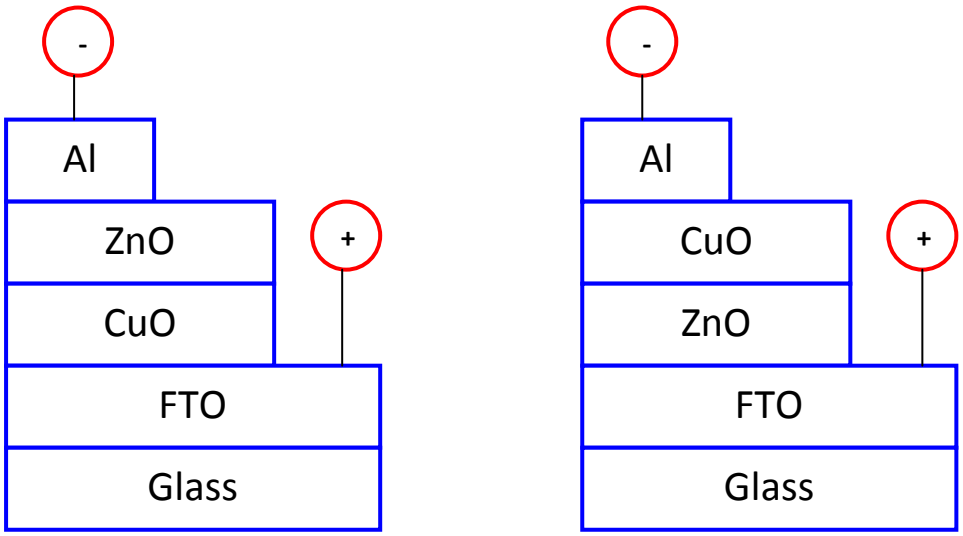

Figure (4-4): structure of (a) FTO/CuO/ZnO/Al and (b) FTO/ZnO/CuO/Al solar cells

Fig (4-5): up (1-6) samples ZnO/CuO & lower (7-12) samples CuO / ZnO

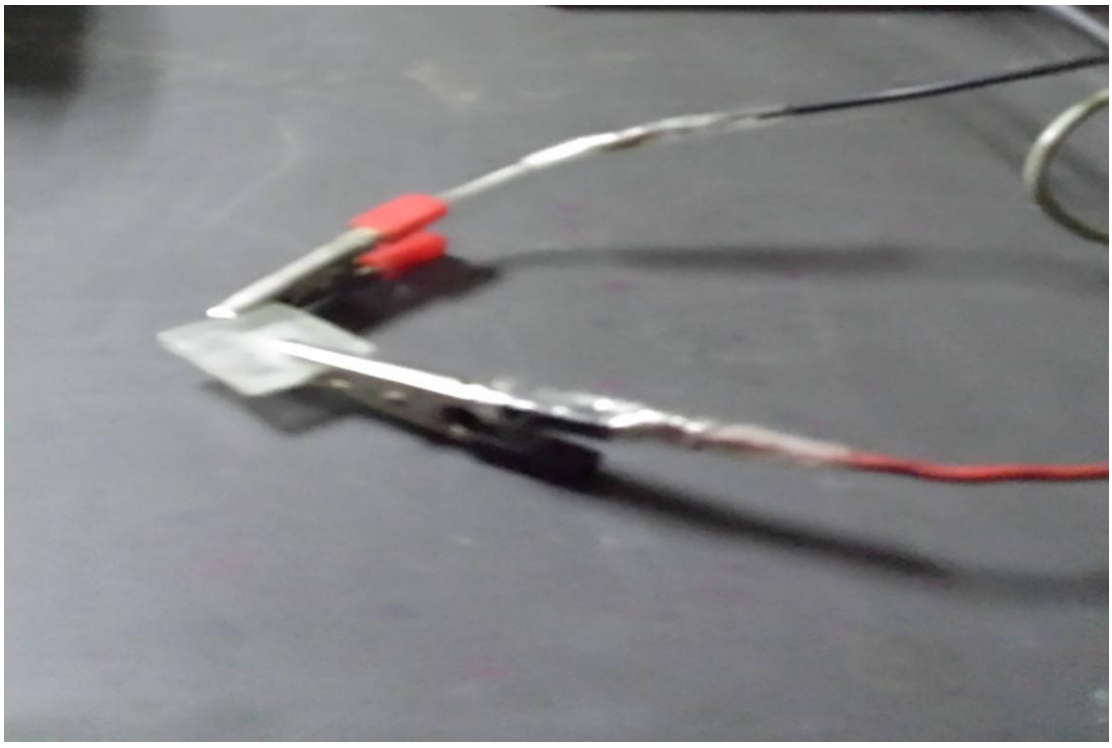

Fig (4-6): the Sample

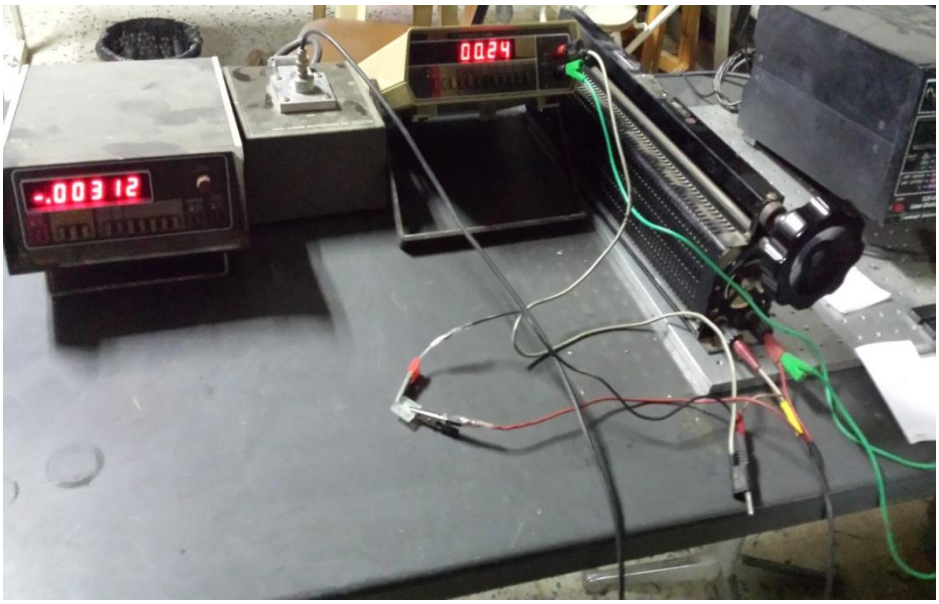

Fig (4-7): (I-V) Reading for the Sample

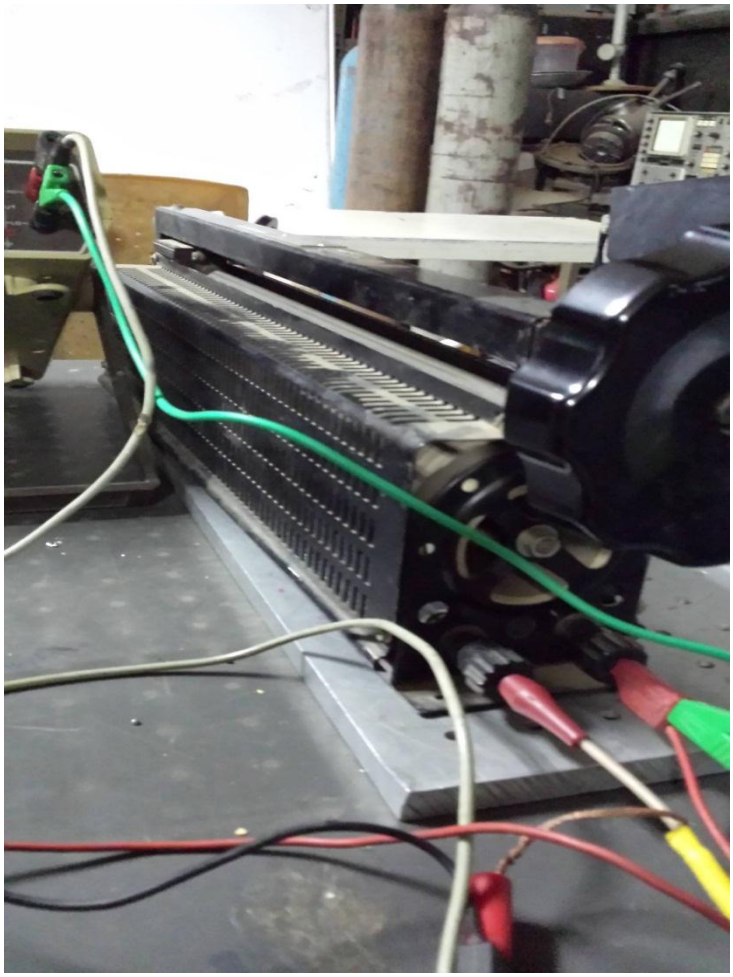

Fig (4-8): Potentiometer

4.4 Result and Discussion

The objective of this work is to develop a low cost, easy to manufacture, cuprous oxide (CuO) – based solar cells with zinc oxide (ZnO) to be fabricated on fluorine – doped tin oxide (FTO) by an electrode position. The performances of solar cells with FTO/CuO/ZnO/Al (six samples from 1-6) structures were investigated.

Measurements of the CuO/ZnO and ZnO/CuO hetero junction light current-voltage characteristics were done. The optical absorption of thin film was also measured, beside determination of the optical band gab energy (E_g)

The FTO/ZnO/CuO/Al sample (1), (2), (3),(4),(5)and (6) structure showed characteristic curves with short –circuit current and open circuit voltage. Table (1) shows measured parameters of ZnO/CuO –based solar cells.

The figures below, shows V-Icharacteristics for ZnO/CuO sample (1), (2), (3), (4),(5)and (6) of ZnO/CuO solar cells.

The FTO/CuO/ZnO/Al, stricture (7), (8), (9), (10), (11) and (12) showed characteristic current with short – circuit current density (J_{sc}) and open – circuit voltage (V_{oc}), fill factor (FF) and provided a power conversion efficiency (η) , Table (2) shows measured parameters of CuO/ZnO – based solar cells.

Table (4.1): FTO/ZnO/CuO/Al solar cells performance

Structure	(V_{oc})V	J_{sc} (mA cm^{-2})	FF	η%
(1)	0.221v	$10^{-3}\times2.858$	0.99	$10^{-4}\times6.24$
(2)	0.220v	$10^{-3}\times2.9083$	0.98	$10^{-4}\times6.32$
(3)	0.221v	$10^{-3}\times2.9316$	0.99	$10^{-4}\times6.45$
(4)	0.223v	$10^{-3}\times4.462$	0.98	$10^{-4}\times9.790$
(5)	0.222v	$10^{-3}\times3.003$	0.98	$10^{-4}\times6.55$
(6)	0.214v	$10^{-3}\times2.688$	0.97	$10^{-4}\times5.59$

In view of tables (1) FTO/ ZnO/CuO/ Al solar cell the average efficiency is about ~ 0.65×10^{-3}.Whilethe average efficiency for FTO/CuO/ZnO/Al is about ~ 2×10^{-3} the efficiency of FTO/ZnO/CuO/Al is lower than FTO/CuO/ZnO/Al type.

Table (4.2): FTO/CuO/ZnO/Al Solar Cells performance

Structure	(V_{oc})V	J_{sc} (mA $10^{-3}\times cm^{-2}$)	FF	η%
(7)	1.23	2.74	0.787	$10^{-3}\times2.62$
(8)	1.14	2.75	0.763	$10^{-3}\times2.39$
(9)	1.13	3.30	0.821	$10^{-3}\times3.06$
(10)	0.875	2.767	0.904	$10^{-3}\times2.188$
(11)	0.220	2.86	1.18	$10^{-4}\times7.303$
(12)	0.898	2.81667	0.85	$10^{-3}\times2.14$

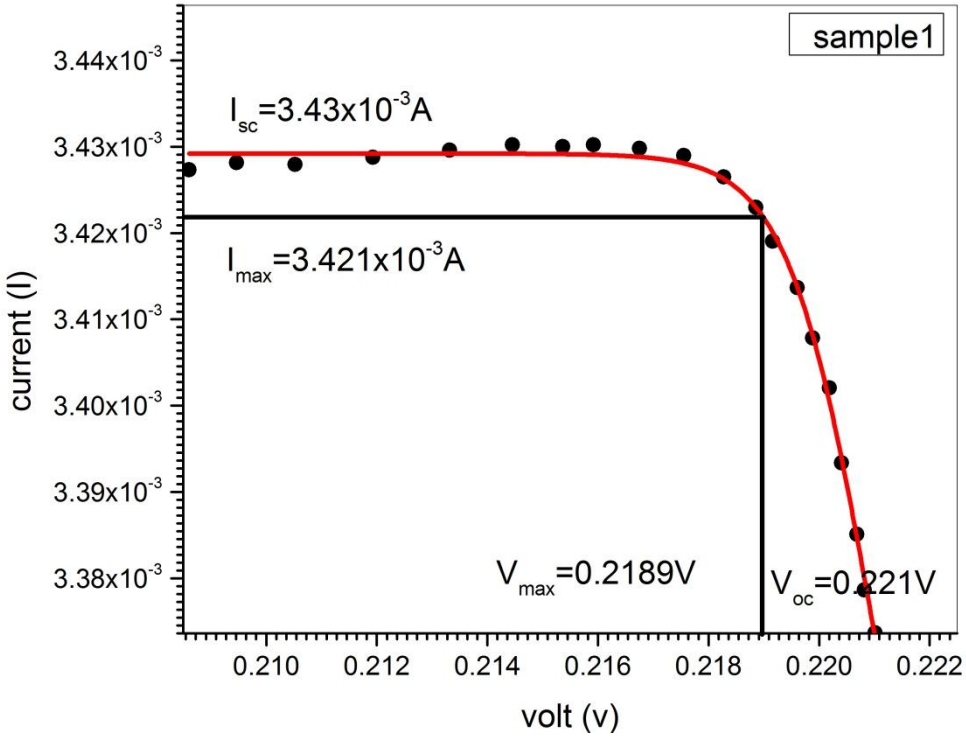

I-V. Characteristics for sample 1

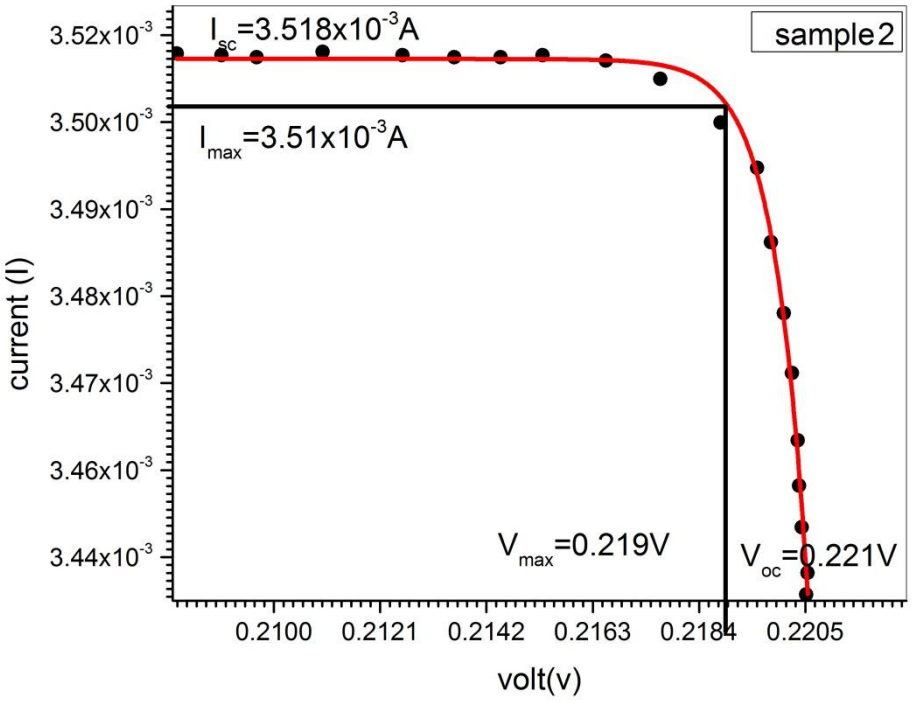

I-V. Characteristics for sample 2

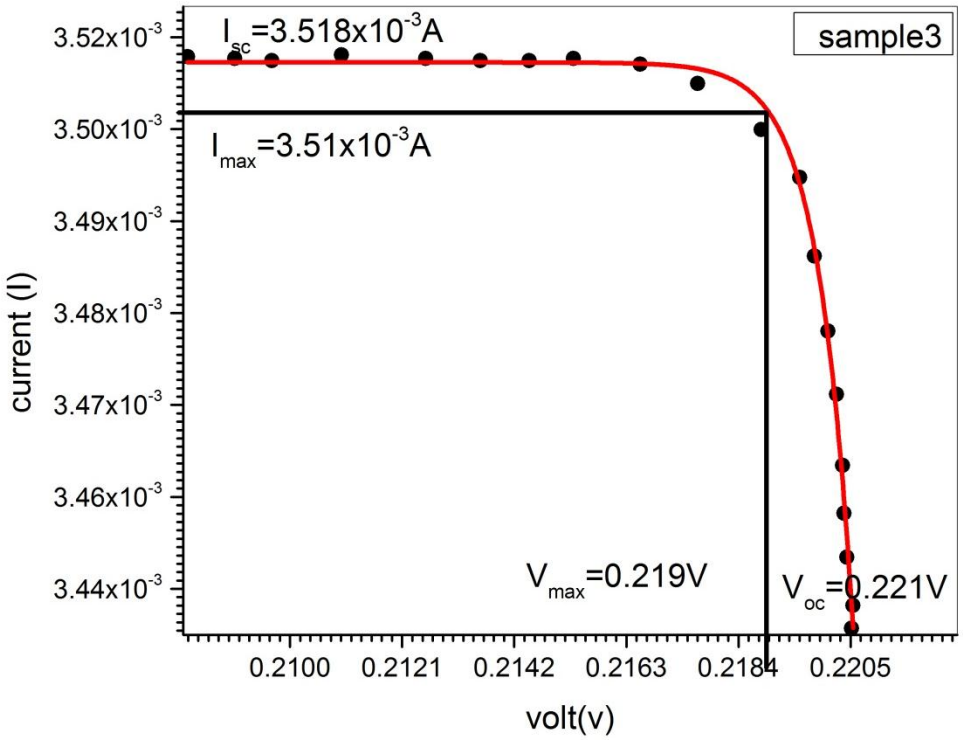

I-V.Characteristics for sample 3

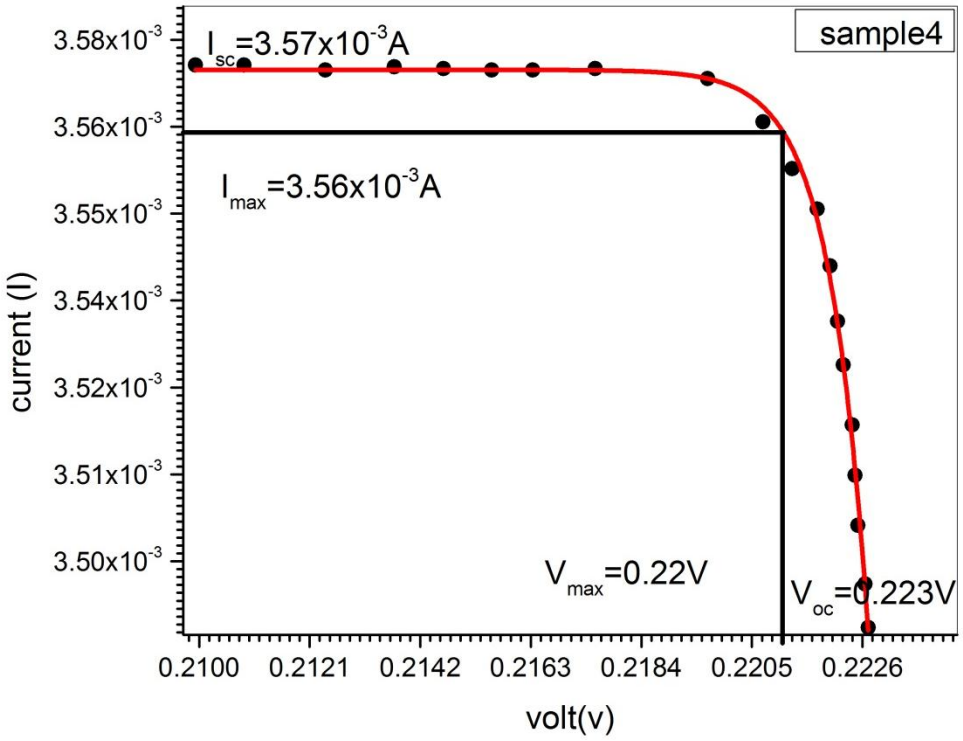

I-V.Characteristics for sample 4

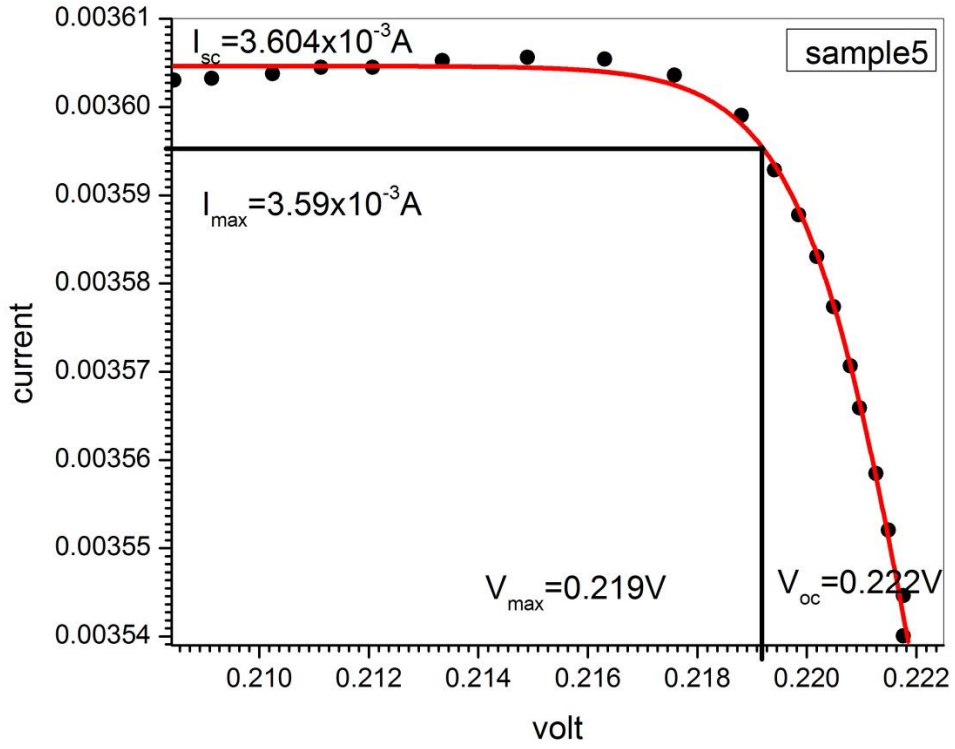

I-V.Characteristics for sample 5

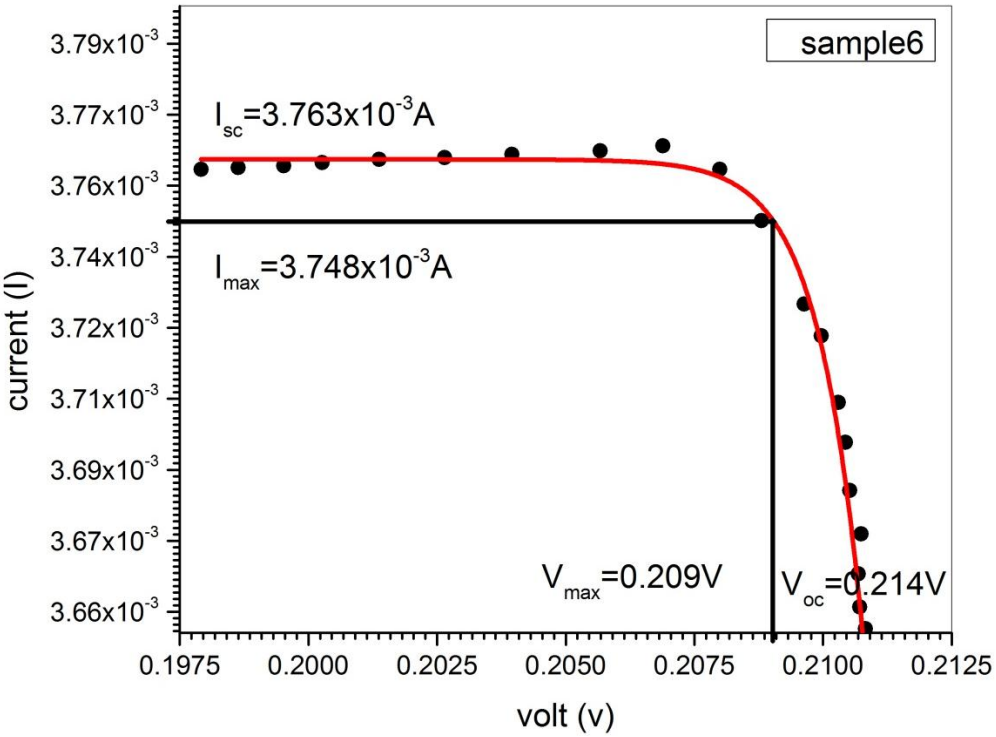

I-V.Characteristics for sample 6

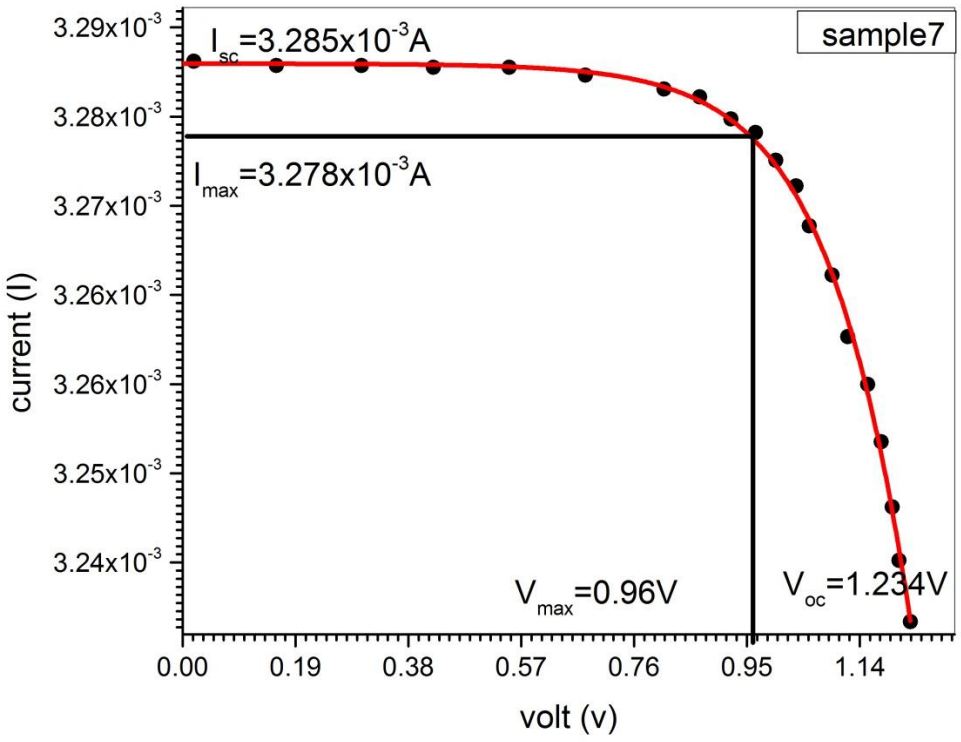

I-V.Characteristics for sample 7

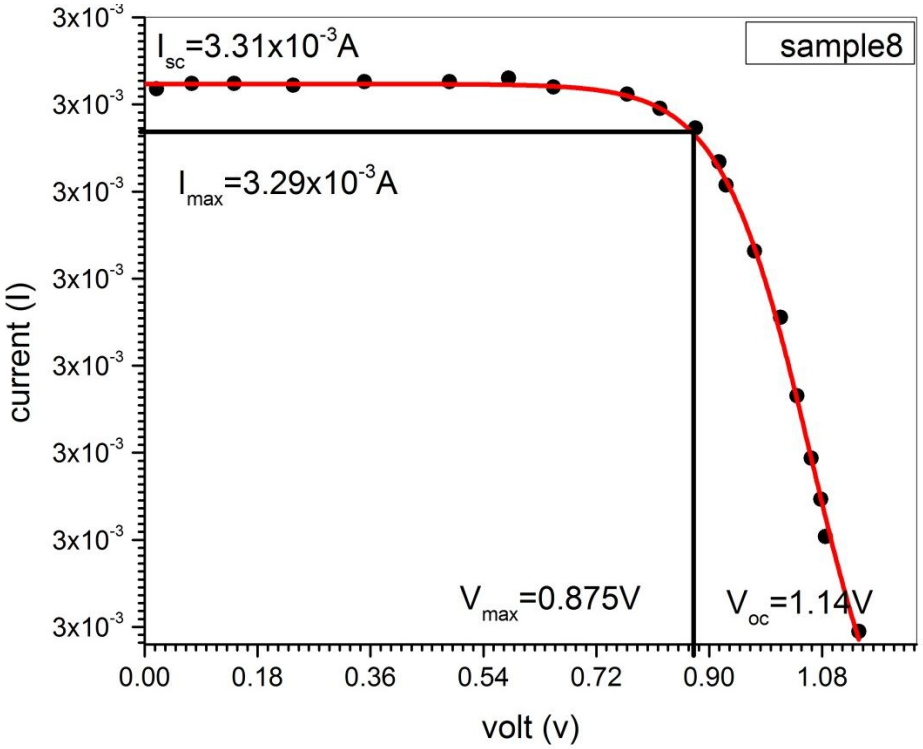

I-V.Characteristics for sample 8

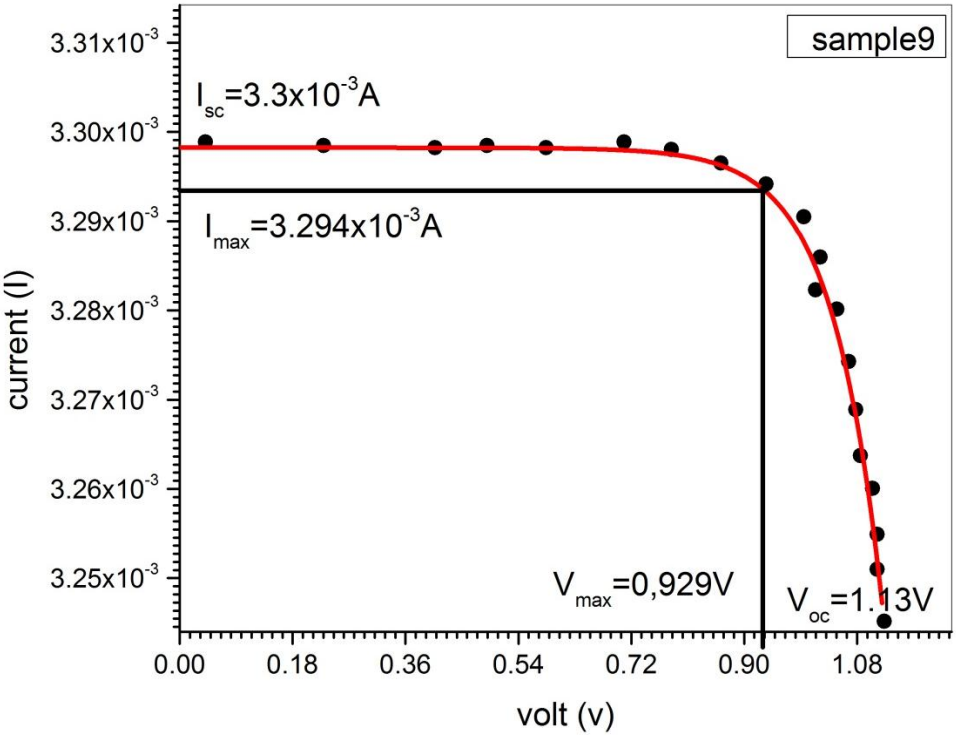

I-V.Characteristics for sample 9

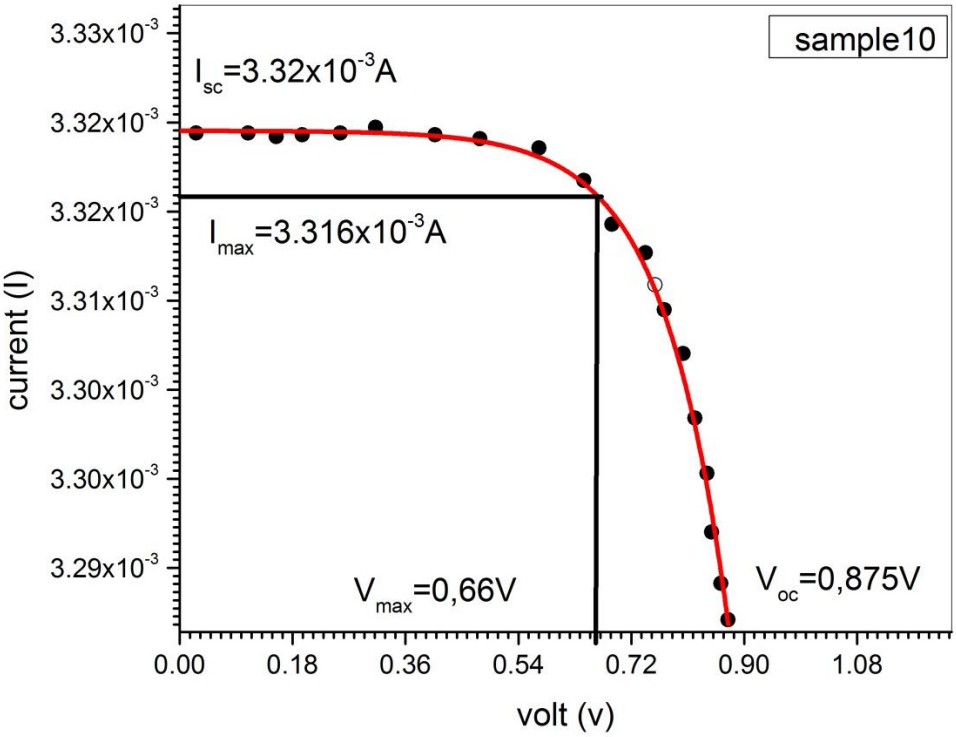

I-V.Characteristics for sample 10

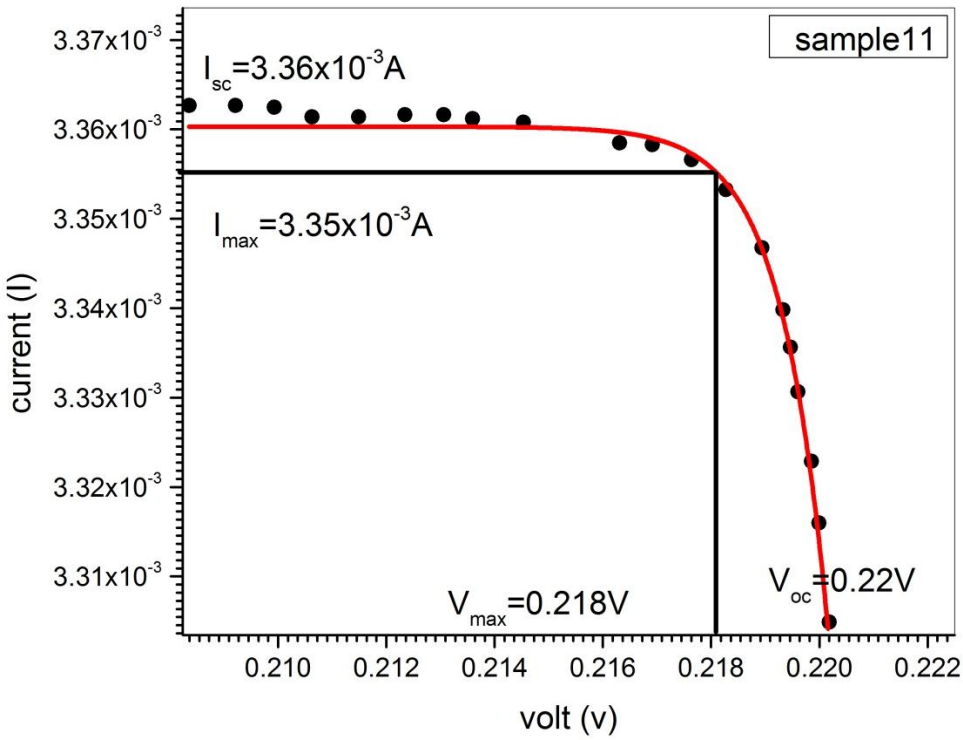

I-V.Characteristics for sample 11

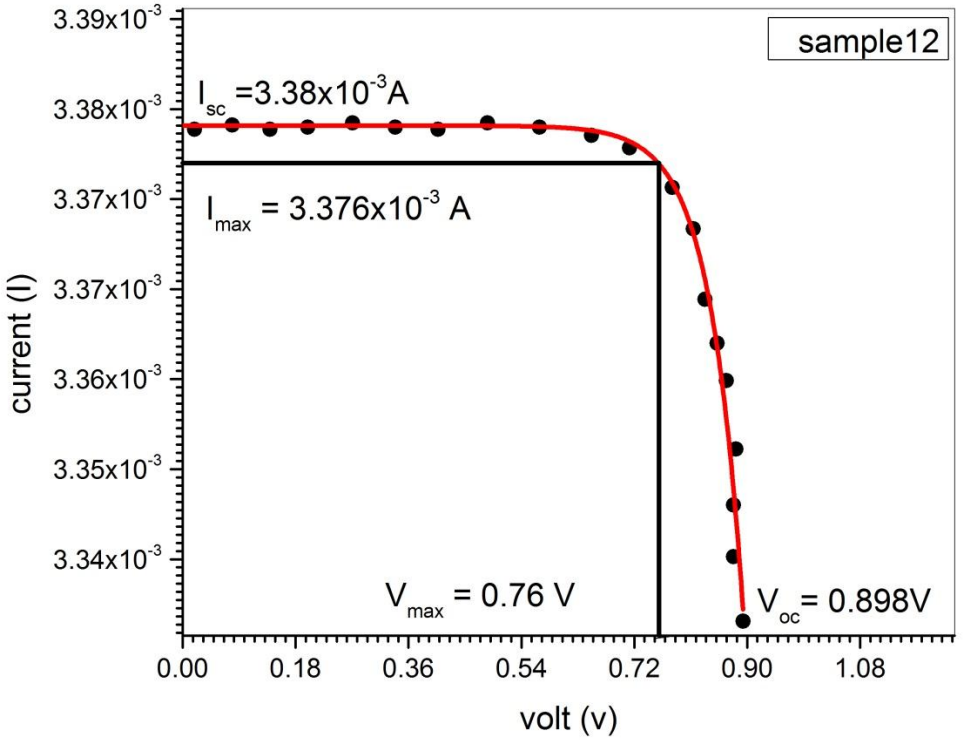

I-V.Characteristics for sample 12

In view of table one (1) for FTO/ZnO/CuO/Al solar cells the average efficiency is about $\sim 0.65 \times 10^{-3}$. While the average efficiency for FTO/CuO/ZnO/Al is about $\eta \sim 2 \times 10^{-3}$ of FTO/ZnO/CuO/Al is lower than FTO/CuO/ZnO/Al type. This may be related to the fact that FTO act as a p- type semiconductor since F acts as an accepter, which is well known the literature. ZnO act an n- type while CuO is a p-type semiconductor.

Thus the first cells act as pnp Semiconductor therefore the free electrons amount in ZnO diffusing to the negative electrode were lowered appreciably by CuO holes, since these electrons passes through their ways to the negative electrode. However, the situation is different for the second cell which acts as a ppn semiconductor. For such cell the ZnO free electron transfer directly to the negative electrode, while CuO and FTO holes diffuse to the positive electrode thus increases electric potential difference appreciably.

Figure (13) shows measured optical Absorption of thin films. The CuO thin films show high optical absorption in the range of 400 nm to – 700 nm. This corresponds to an energy band gab (for 800 nm), $E_g \sim 1.3$ -2eV which is near the known value 1.2 eV.

For ZnO the absorption range is (300 – 550 nm) with energy gap in the range $E_g \sim$ (2.2 – 3.3) eV.

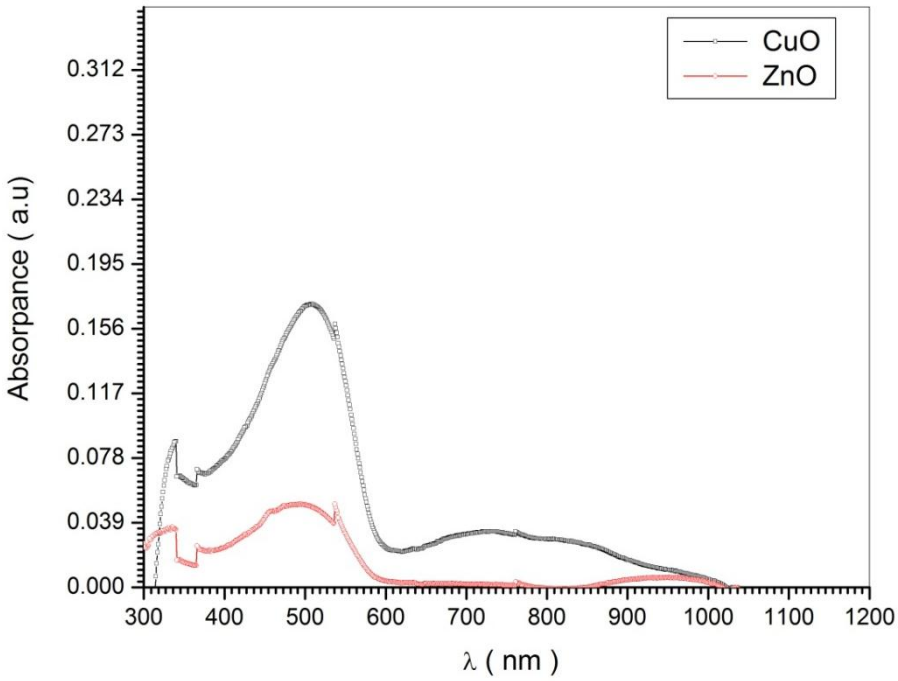

Figure (4.21) UV – Visible absorption spectra of thin films prepared by electrode position.

Transmittance spectrum of 0.3 μ m thick CuO film, deposited on FTO is presented in fig (2-15) and ZnO film in fig (3- 16).

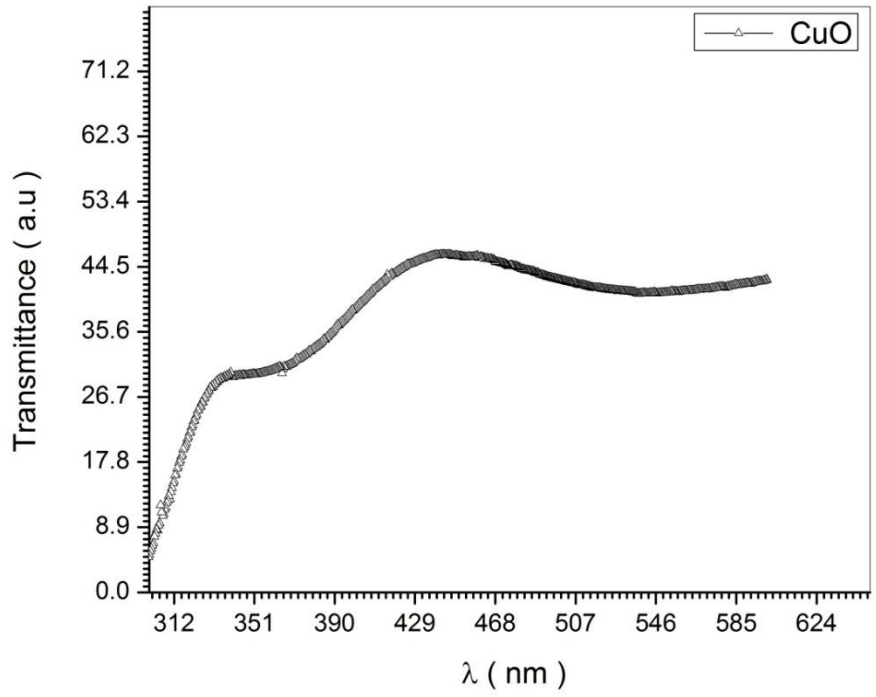

Figure (4.22) optical transmission spectrum of 0.3μm thick CuO film

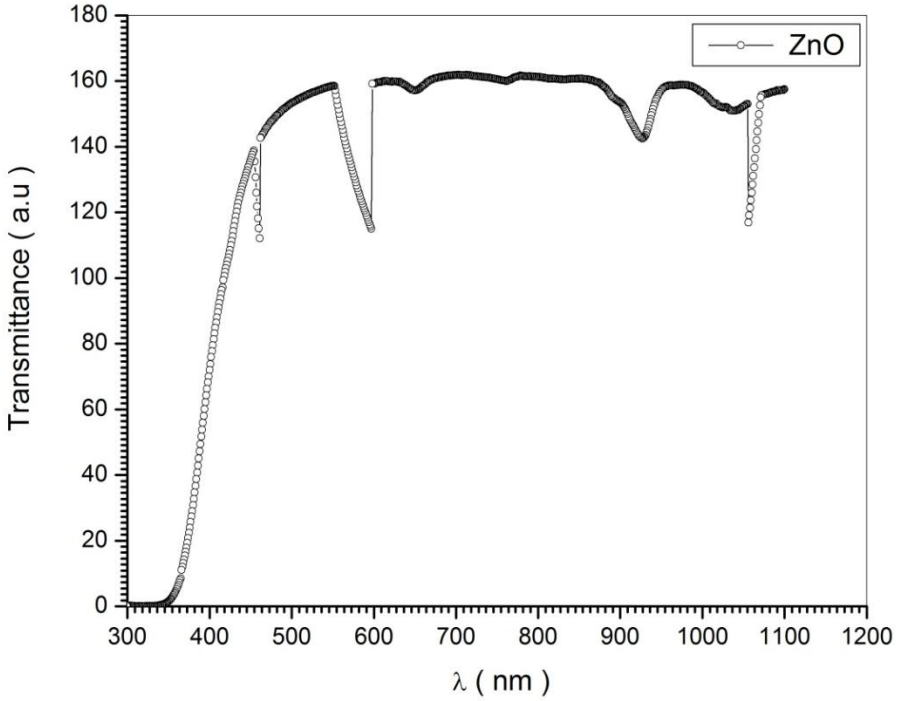

Figure (4.23) optical transmission spectrum of 0.3μm thick ZnO film

The transmittance for CuO in figure (4.21) shows that the transmittance at about 300 nm drops abruptly corresponding to energy gap $E_g \sim$ 3.7eV which is apparently in conflict with the real value E_g (acceptor) ~1.2eV.

This discrepancy can be removed if one bears in mind that E_g (acceptor) ~1.2eV is the energy gap between top valance band and acceptor level. Since acceptor atoms are very few compared to the host CuO atoms. Then one expect radiation absorbed for electron transfer to the acceptor level can be neglected compared to a large amount of radiation absorbed to transfer electron from conduction to valence band of CuO which is as wide as $E_g \sim$ 3.7eV. However the situation is different for ZnO which is an n-type semiconductor, where the donor level is near conduction band. Thus

$$E_g \text{ (donor)} \sim E_g \text{ (cond. valence)}$$

Therefore transmittance spectrum in figure (3) shows an energy gap for ($\lambda \sim 300nm$) of value, E_g (cond, valence) ~ 3.6 eV which is near the known value E_g (donor) ~ 3.3eV .The fact that:

$$E_g \text{ (cond, valence)} > E_g \text{ (donor)}$$

Again confirms the fact the ZnO host atoms which have very high concentration absorb radiation more efficient than donors which have low concentration, from the spectrum of the optical band gap for CuO can be found. The optical absorption coefficient (α) of this film it can be determined from the spectral transmittance.

The determination of the optical band gap energy (E_g), for CuO is based on the relation of:

$$\alpha h\nu = A\,(h\upsilon - Eg)^{n/2} \qquad (4.1)$$

Where n is a number that depends on the nature of the transition. In this case is value was found to be 1 (which corresponds to direct band to band transition) because that value of n yields the best linear graph of $(\alpha h\nu)^2$ versus hν. In view of figure (4) the band gap for CuO is which agrees with the range (1.5 – 2.0) eV.

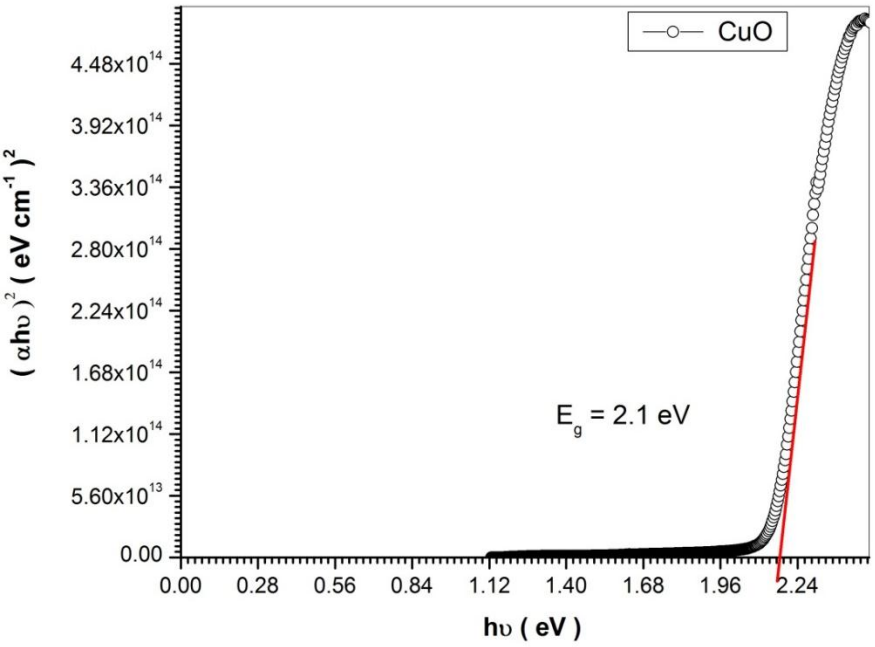

Figure (4.24) photon energy and absorption Coefficient

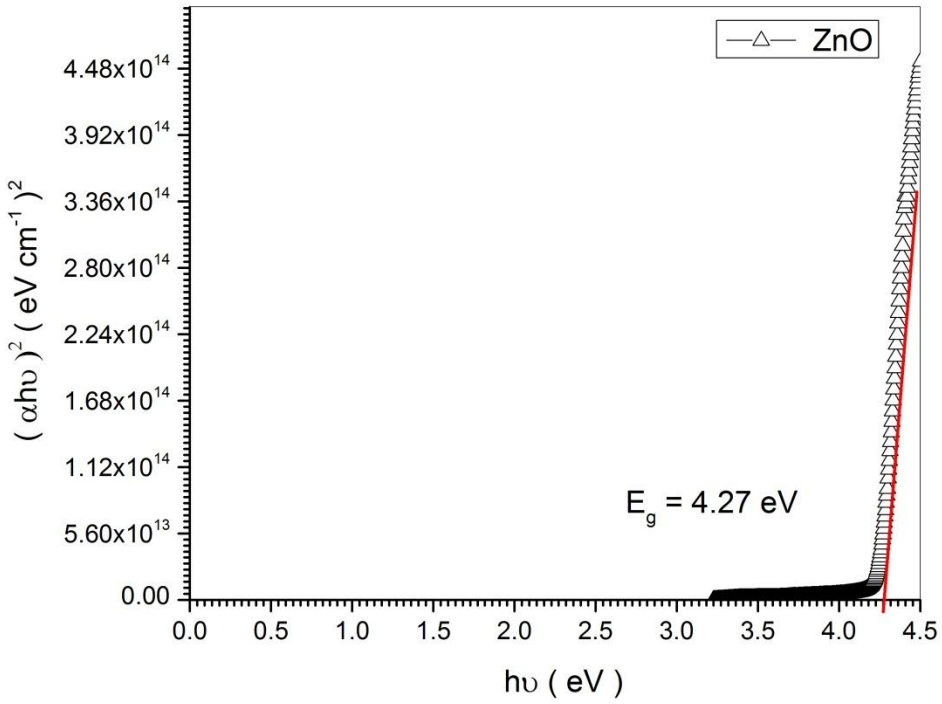

Fig (4.25) (b) Tauc plot for the ZnO thin film

The plate shapes of the spectrum for ZnO and CuO in figs (4.21) and (4.22) towards longer wave length conforms to fact that low energy photons escape without being absorbed as for as they have no sufficient energies to transfer electrons from valence to conduction band. It also observed that for FTO/ZnO/CuO/Al solar cells the area decrease increases the efficiency and V_{oc}. This may be related to the fact that V_{oc} is related to the concentration of carriers by treating the terminal of the cell as capacitors of electric field E and potential difference V given by:

$$Voc = EL = \frac{\sigma l}{\varepsilon} = \frac{nl}{A\varepsilon} \qquad (4.2)$$

Where L is the length of the cell, A being the cross sectional area. Thus the area decrease increases V_{oc}, which in turn increases the efficiency η.

Table (4.3) Relation between A, V_{oc} and η

A	**V_{oc}**	**η**
1.4	0.214	$10^{-3}\times0.5595$
1.2	0.222	$10^{-3}\times0.6551$
0.8	0.223	$10^{-3}\times0.9790$

4.5 Conclusion

The solar cell which is formed from FTO/CuO/ZnO/Al respectively is more efficient and has good performance compared to FTO/ZnO/CuO/Al solar cells. The efficiency can be increased considerably by adding donors to ZnO and acceptors to CuO.

The optical properties of ZnO and CuO indicate that the optical transmittance spectrum determines the energy band that separates conduction band from the valence band. The small difference between optical band gap for ZnO and the real value confirms the fact that it is an n – type semiconductor. While the large difference for CuO indicates that it is a p – type semiconductor. The absorption spectrum is related to the donor or accepter levels.

References

[1] Ahmed Khogali, Solar energy, Sudan coin press, Khartoum (2007).

[2] Maissel, L.I, and Change, R., Hand book of thin film technology, MC-Graw-Hill, new york (1970).

[3] N.S. Sariciftci, primary photo excitations in conjngated polymers, world scientific, Singapore.

[4] Pope, M., swenberg, C.E., Electronic processes in organic crystals and polymers, oxford university press, new york (1999).

[5] PhD by dipl. Ing. Klaus Detvitsch"organic solar cell Architectures" Cambridge and craz, July 2000.

[6] Kazuya Fujimoto, Takeo Oku, Tsuyoshi Akiyama and AT sushi Suzuki " fabrication and characterization, of copper oxide – zinc oxide solar calls prepared by electrode position", Department of materials science, The university of shiga prefecture, Hikone, Shiga 522 – 8533, Japan 2012.

[7] Hiroki Kidowaki, Takeo Oku and Tsyoshi Akiyama "Fabrication and evaluation of CuO/ZnO Heterostructures for photoelectric conversion 2500 hassaka, hikone, shiga 522-8533 Japan – October 2012.

[8] E.O. Omayio, P.M. Karimi, W.K. Njoroge, F. K. Mugwanga, "current – Voltage characteristics of P-CuO/n-ZnO: sn solar cell" Department of physics and Kenyatta university, Kenya December 2012.

[9] H.Kidowaki, T. Oku, T.Akiyama "Fabrication and characterization of CuO/ ZnO solar cells" Department of Materials Science, The university of shiga prefecture, 2500 Hassaka, hikone Shiga 522 – 8533, Japan 2011.

[10] B. Das, S.P. McGinnis, P. Sines "High Efficiency solar cells based on semiconductor nanostructures" West viranina

University. Morgan Town, WV 26506 – 6109, USA September 1999.

[11] A. Kay, M. Gratzel, J. Phys. Chem. 97 (1993), 6272.

[12] Yee – Fun Lim, Joshua Jochaj. choi, and Tobias Hanrath "Facile Synthesis of colloidal CuO nanocrystals for light – harvesting Applications" Gornall University, (Thaca, N.y 148533 – 1501, USA 14 July 2011.

[13] C.I. Brabec and J.R. Durrant "Solution – Processed Organic Solar cells" MRS Bulletin, Vol, 33, no, 7 PP. 670 – 675, 2008.

[14] Li, G., Shrotriya, V., and yao, Y. " Investigations of annealing effects and film thickness dependence of polymer solar cells based on poly (3- hexylthiophent Appl, Phys, V, 98. No. 4, PP- 043704, 2005.

[15] A.K. Pandey, J.M. Nunzi, B- Partier, and A. Molition, "size effect on organic optoelectronics devices", Example of photovoltaic cell efficiency Elsevier, V. 372, PP.1333 – 1326, 2007.

[16] U mang V Desai, Chengkun Xu, Jiamin Wu and Di Gao "solid – state dye – sensitized solar cells based on ordered ZnO nanowire arrays" university of Pittsburgh, PA 15261, USA, 16 march 2012.

[17] M Gloeckler, Al Fahrenbruch, JR sites "Numerical modeling of CIGS and CdTe Solar cells: setting the Baseline" 3rd conf. Pvener - conv., 491 – 494, 2003.

[18] SI Fonash. Solar Cell Device Physics. 2nd edition, Elsevier USA, 2010.

[19] Donald A. Neamen "Semiconductor Physics and Devices", University of New Mexico, 3rd edition, 2008.

[20] CA wolden, Jkurtin, JB Baxter, I Replins, SE Shaheen, JT Torvik, AARocket, VM Fthenakis, ES Aydil "Photovoltaic Manufacturing: Present Status, Future Prospects and

research needs" J: Vac. Sci. Technol. A29(3); 03080 i(1.16), 2011.

[21] John and Willi Leone family Department of energy and mineral engineering "Numerical modeling of Tin – Based Absorber devices for cost – effective solar photovoltaic" may 2012.

[22] A. Mittiga, E. Solar , F.Sarto, M. Jucci and R- Vasnthi, Heterojunction solar cell with 2% efficiency based on a CuO substrate, App. Phys. 2006.

[23] M. Izaki, T. Shinagawa, K. Mizuno, Y. Ida, M. Inava and A. Tasaka, Photo chemically hetero junction diode device, J. Phys. D: App. Phys 2007.

[24] B. G hoch, M. Dos, P Banerjee., S DAS " Fabrication of the SnS/ ZnO Hetero Junction for PV Application using electrodeposited ZnO films " Semiconductor. Sci. Techno 2013.

[25] Kamat, P.V, et al (2014) "semiconductor nano particles, in hand book of nano structured materials and nanotechnology, Academic press: New York.

[26] Warfel. P (2009) physics of solar cells – form principles of new concepts, wiley VCH.

[27] R. V inodkumar, K.J.L. etthy, D. Beena A.D. Detty, I. Nava, U. V. nayor, V.P mahadevan, V. Ganesan, V.R.R eddy, Effect of ITO buffer layers on the structural, optical and electrical properties of ZnO multilayer thin films prepared by pulsed laser deposition technique, Sol, energy. Mater. Sol. Cells 2011.

[28] H. Kidowaki, T. Oku, T. Akiyama, "Fabrication and characterization of CuO / ZnO solar cells, Journal of physics: Conference Series, 2012.

[29] V. D. Mihailetchi (2010) Device physics of organic bulk heterojunction solar cells, PHD thesis, University of groningch.

[30] Wirfel (2014), physics of solar cells – 1st ed, weinheim, wiley .VcH.
[31] Peiwei Lv, Weifeng Zheng, Limei Lin, Fuchuan peng, Zhigao Huang, Fachunlai " I-V characteristics of ZnO/ CuO thin film n-i-p heterojunction", School of physics and opto – electronic tech, fuijan Normal university PR China B January 2011.
[32] VA Gevorkyan, A E Reymers, M Neresyan, " Characterization of Cu_2O thin films prepared by evaporation of CuO powder" 2012.
[33] Shih-fong Lee, Yung-Ping Chang, Li-Ying Lee, Jung-Fu Hsu " Characterization of Dye – Sensitized Solar Cells with ZnO Nanorod Multilayer Electrode" 2007 National Kaohsiung University of Applied Sciences, ISSN 1813-3851.
[34] Marius Grundman, "The physics of Semiconductors, An introduction Including Devices and Nano physics, January 2006.
[35] S.M . Sze, Hsincha , Taiwan, Kwakk, Ng san Jose, Clifornia, "Physics of Semiconductor Device Third Edition, July 2006.
[36] Martin A. Freen, Keith emery, yoshihiro hishikawa and Wilhelm warta, Solar cell efficiency tables (version 37), John 2010.
[37] Antonio Facchelttti. (2010), π -Conjugated polymers for organic Electronics and Photovoltaic Cell Applications. Journal of Chemistry and the materials Research Center United States, Northwestern University 214: 202-211.
[38] Bassam Z. Shakhashiri A Handbook for Teachers of Chemistry 'polymers' Journal Chemical or the week, volume 1 (1983), Page 241.
[39] Barry C. Thompson and Jean M. J.Fr_chet*" Polymer-Fullerene Composite Solar Cells" 2008 Wiley-VCH Cerlag

GmbH & Co. KGaA, Weinheim Angew. Chem. Int. Ed. 2008.

[40] Chang, R.; Hsu, J.H.; Fann, W. S.; Liang, C.H.; Hayashi, M.; Yu, J.; Lin, S.H.; Chang, E. C.; Chuang, (2000) Investigations of Ultrafest Dynamics in Light-emitting polymers. Journal of chinese Chemical Society (1-2): 142-152.

[41] C.J. Brabec, G. Zerza, G. Cerullo, S. De Silvestri, S. Luzzati, J. C. Hummelen (2001). Tracing photoinduced electron transfer process in conjugated polymer/ fullerence bulk heterojunctions in real time. Journal of chemical physics letters 340: 232-236.

[42] N. S. Sariceftic (Ed.), (1998), Primaty photo excitations in conjugated polymers: Moleculat excition versus Semiconductor Band Model. World Scientific Publishers, Singapore.

[43] Peter Gevorkian. (2007). Sustainable energy systems engineering: the complete green building dsign resource. McGraw-Hill Professional. PP. 498. http://books.google.com/books?id=i8rc.

[44] Santra, Pralay K.; Kamat, Prashant V. (2012). "Mn-Doped Quantum Dot Sensitized Solar Cells: A Strategy to Boost Efficiency over 5%". Journal of the American Chemical Society 134 (5): 2508-11. doi:10.1021/ja211224s. PMID 22280479.

[45] Graham, S. C,; Bradley, D. D. C.; Friend R. H.; Spangler, (1991). Raman and photoluminescence spectra of PPV oligomers. Journal article in the OhioLINK Electronic 41: 1277-1280.

[46] http://en.wikipedia.org/wiki/semiconductor

[47] Wikipedia the free En cyclopedia Electronic bad structure.

[48] B. van zeghbroeck. , "preinciples of semiconductor device", 2011

[49] http://en.wikipedia.org/wiki/doping-(simicandoctor)
[50] http://www.halbleiter.org/en/fundamentals/doping(funamentalsdoping:n-andP-semconductor.
[51] R. R. king, D. Bhusari, D.Larrabee, X.Q.Liu, E.Rehder, K.Edmondson, H.Cotal, R.K. Jones, J.H. Ermer, C.M. Fetzer, D.C. Law and N. H. Karam, "Solar cell generations over 40% efficiency" Germany 2011.

Appendix